ZnTeO and Oxygen Doped II-VI Ternary Alloys for Intermediate Band Solar Cells

by

Chihyu Chen

A dissertation submitted in partial fulfillment

of the requirements for the degree of

Doctor of Philosophy

(Applied Physics)

in The University of Michigan

2015

Doctoral Committee:

Professor Jamie D. Phillips

Professor Roy Clarke

Professor Rachel S. Goldman

Assistant Professor Emmanouil Kioupakis

Associate Professor Pei-Cheng Ku

2015

Dedication

For my parents.

Acknowledgements

First and foremost, I would like to thank my thesis advisor Prof. Jamie D. Phillips for offering me a position in his lab when all other doors seemed closed and I was looking at the real possibility of having to leave graduate school. I stumbled into the business of MBE, and it turned out to be an incredibly empowering and rewarding experience. I sincerely thank Prof. Phillips for trusting me with his MBE, and for patiently guiding me over the years while taking seriously and encouraging me to pursue my own ideas as I learned to solve technical and scientific problems, and become a more scientific person. This has been a deeply rewarding journey.

I would like to thank my committee members for the many useful suggestions and collaborations over the years. Several key experiments presented in this thesis were a direct result of these suggestions and collaborations.

I would like to thank my many MBE colleagues across the campus, for sharing their experience, and MBE parts, during MBE emergencies and during many informal discussions in hallways, and in each other's labs and offices. I enjoyed the camaraderie immensely, and I also thank them for offering many times the compassion that can only be given by people who truly understand the horrors of what an MBE can do to its growers. In particular, I would like to thank Thomas, Sishir, Animesh, Shafat, and Kyusang.

Several of the major MBE repairs would not have been possible without the help of LNF staff. I in particular think Dennis Schweiger and David Sebastian for the many times they offered hands-on help and advice for MBE repairs and upgrades.

I was very lucky to be part of CSTEC during my time here. As a result I was exposed to ideas and perspectives from collaborators in several different groups and departments. I especially thank Vladimir Stoica and Sung Joo Kim for the many fruitful discussions and collaboration.

I would also like to thank my past and present group members, in particular Weiming, Bor-Chau, Adrian, Jinyoung, Justin, Alan, and Conor, for the many useful discussions and friendship. I especially thank Weiming for training me to use the MBE, Justin and Alan for challenging my ideas- it was an important part of me becoming more scientific in my thinking.

Finally, I would like to thank the many friends that shared with me and witnessed much of this journey. In particular, Leslie, Elizabeth, Steve, Alan, Robert, Sishir, Thomas, Animesh, Allan, Shafat, and Justin.

Table of Contents

List of Figures

List of Tables

Abstract

ZnTeO is a promising material for next generation photovoltaics and X-ray scintillators.

ZnTeO is a highly mismatched alloy (HMA) where O is much more electronegative than the host Te. O and HMA effects between O and the CB of ZnTe have been predicted to form a sub-bandgap band[1]. When the oxygen concentration is high, the oxygen related states have been said to merge into a band, and called an intermediate band (IB), and may potentially be an Intermediate Band Solar Cell (IBSC) absorber.

In the case of X-ray scintillators, ZnTeO as an X-ray phosphor material has the some of the fastest decay time of ~1 μs, largest gain efficiency of, and lowest afterglow with respect to common material systems, which are important for fast time resolution, brightness, and signal to noise, respectively, for the final X-ray detection system.

The thesis presents detailed work on ZnTeO material. Structural, chemical, optical, and lifetime data shows that oxygen induces an intermediate band (IB) approximately 0.4 eV below the conduction band (CB) edge, when the oxygen concentration is approximately 10^{20} cm^{-3}. It is shown that the electronic structure of the oxygen induced energy levels are influenced by oxygen location in the crystal lattice, which can be influenced by oxygen plasma back ground pressure used during material synthesis. Photoluminescence, X-ray diffraction and Nuclear Reaction Analysis channeling data

reveals that the oxygen likely resides in both Te substitutional positions and interstitial positions.

A novel two pump time resolved photoluminescence was used to observe the time resolved electron transfer from the VB to IB, and then from IB to CB with two sub-bandgap pulses. A novel way to prepare GaSb(100) substrate for ZnTe epitaxy was developed to enable near lattice matched growth of ZnTeO on GaSb(100). The reduction of the FWHM of the XRD peak from approximately 300 arc-seconds for ZnTe/GaAs(100) to 40 arc-seconds for ZnTe/GaSb(100) was achieved. Ternary II-VI alloys of ZnSeTe, CdMgTe, and CdZnTe with bandgaps of approximately 2 eV, near the ideal bandgap for IBSCs were synthesized. Oxygen was then introduced during synthesis to form sub-bandgap electronic states for use as IB.

Chapter 1
Introduction

1.1 The Need to Mitigate Climate Change

Coal and other fossil fuel based energy sources reliably supported the large economic growth of the global economy following the Industrial Revolution. However, there is scientific consensus that continued burning of fossil fuels at current levels will lead to climate change that can disrupt future economic development. The Intergovernmental Panel on Climate Change projects for the end of the 21st century and beyond with high confidence that the global mean temperature will likely exceed 2^{o} C above 1850-1900, that in most places there will be more hot and fewer cold temperature extremes, and that it is very likely that the Arctic Sea ice will continue shrinking, and that northern hemisphere snow cover will decrease[2]. For example, increased high temperatures may causes challenges for agricultural production, and rising sea levels may pose threats to coastal human settlements. Since greenhouse gas emissions from fossil fuel combustion significantly contributes to climate change, it has been recommended that human societies shift towards renewable energies to power its future economic development. There is international consensus that the goal of avoiding a greater than 2^{o} C increase in the global mean temperature should be a baseline goal, and to achieve it,

renewable energy should be cost competitive with fossil fuel energy sources by the middle of the 21st century[3].

1.2 Solar Energy as a Renewable Energy Solution

Renewable energies potential far exceeds the global energy demand, as shown in Table 1-1 [3]. The theoretical potential is defined as the amount of energy from the source, technical potential is roughly defined as the realistic amount of energy recoverable, and the sustainable potential takes into account various ecological and socioeconomic factors. For example, solar energy alone has a technical potential that is three orders of magnitude higher than the global energy consumption in 2011, and therefore solar energy will likely be an important source of a sustainable energy production in the future[3].

Table 1-1 Estimated amount of renewable energy from different renewable sources that can theoretically, technically, and sustainably be extracted, compared to world energy consumption[3].

	Theoretical Potential	Technical Potential	Sustainable Potential	Production 2008
	[EJ/year]	[EJ/year]	[EJ/year]	[EJ]
Biomass	2,400	800	100	50,3
Geothermal Energy	41,700,000	720	22	0,4
Hydropower	504,000	160	12	11,6
Solar Energy	3,900,000	280,000	10,000	0,5
Wind Energy	110,000	1,700	>1,000	0,8
Total: Renewable Energies	46,000,000	283,500	>11,000	64

In the United States for example, the SunShot Vision Study of the Department of Energy[4] projects that a 75 % reduction in solar electricity cost between 2010-2020 would make solar energy cost competitive to traditional energy sources such as coal, gas, and nuclear. This could lead to rapid and large scale deployment of solar energy

infrastructure, so that by 2020 (2050) the study projects solar electricity to supply 14 % (27 %)of the nation's power demand, leading to energy savings of $6 ($9) per household, and a reduction of emitted CO_2 by 8 % (28 %). To achieve the 75 % percent cost reduction in solar energy, the SunShot Vision Study projects that evolutionary changes on existing technology, primarily through the economies of scale as production is ramped up, is insufficient. Instead, revolutionary improvements in power conversion efficiency and systems cost reduction as a result of technological advances would be required[4]. In this work, we focus on efficiency improvements of photovoltaics (PV), which along with concentrated solar power (CSP) are the two strategies for harvesting energy solar energy.

PV is the direct conversion of Sun's photons into direct current electricity. CSP uses mirrors to focus the Sun's rays to heat up an energy storage medium, such as molten salt, which is then used to generate electricity through steam turbines when energy is needed. Since the cost of solar electricity is directly proportional to the ratio of equipment system cost to conversion efficiency, the solar power can be made cost competitive by reducing systems cost or increasing the conversion efficiency. These two parameters are inter-related. For example, in the case of PV, increased efficiency often is associated with increase in module cost, but as fewer modules are needed, there may be cost reductions in installation labor and non-module electronics, so that the increased conversion efficiency may increase or decrease the overall systems cost[4]. The thesis presents work that attempts to increase the PV efficiency while maintaining lost solar cell cost with the Intermediate Band Solar Cell (IBSC) approach.

1.3 Photovoltaics

In 2011, solar energy supplied less than 0.1 % of the US energy demand. Most of that solar energy was supplied through PV, where crystalline Si (c-Si) had approximately 85 % market share, and thin film technologies such as amorphous Si (a-Si), CdTe, CIGS, make up the remainder of the market. Crystalline Si has the dominant market share because of the substantial knowledge base on the material properties and manufacturing technology associated with silicon, due to development from the microelectronics industry and a near ideal bandgap for the solar spectrum. To reach the cost reduction projections of the SunShot study, the installed solar modules should be at least 25 % efficient[4].

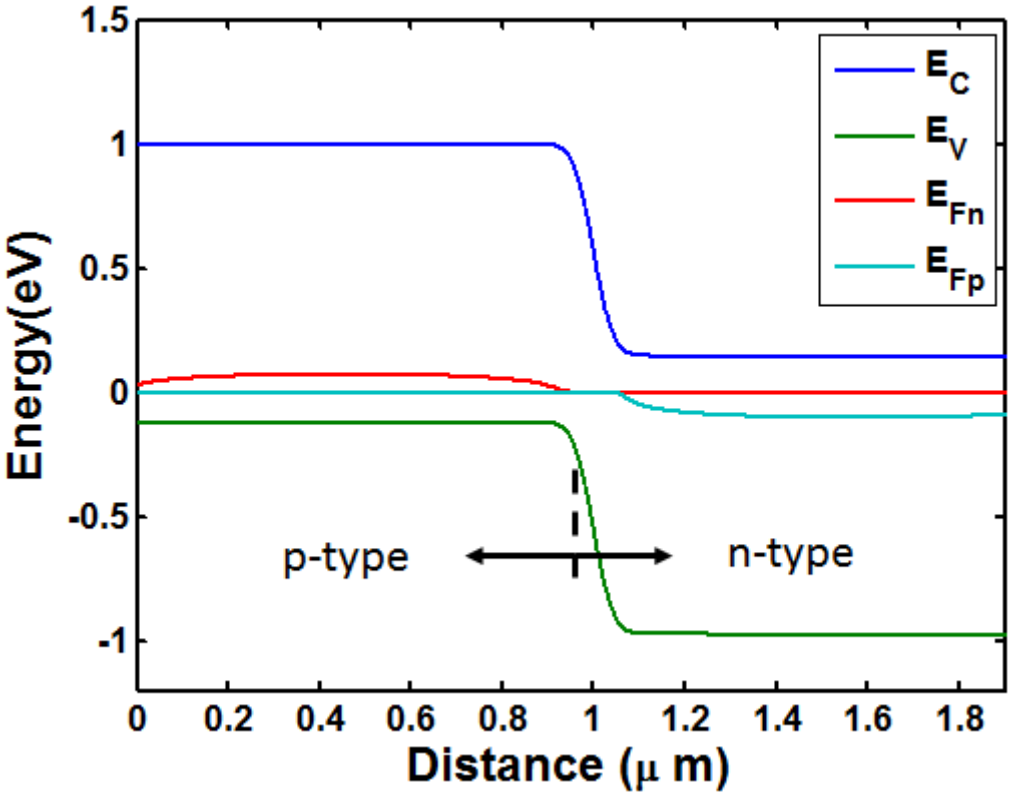

Figure 1.1 Band diagram of a single junction solar cell in the p-n device structure, showing the splitting of the conduction band and valence band quasi-Fermi levels as a result of optical excitation. Simulations done with AMPS-1D[5]

Traditionally, solar cells have a single junction device structure, where the incoming photon excites one electron pair that is separated by the built-in electric field of the semiconductor junction, as shown in Figure 1.1. Single junction cells cannot achieve the ideal Carnot conversion efficiency because these efficiencies are limited by the two fundamental loss mechanisms of thermalization and transparency losses, as shown in Figure 1.2. Thermalization loss occurs when above bandgap optical excitation generates charge carriers at energies larger than band edge energy, for which the excess energy is quickly lost to the crystal lattice as heat. Transparency loss occurs when the photons with energy less than the bandgap are not absorbed by the semiconductor. In selecting the bandgap energy of the semiconductor, there is a tradeoff between thermalization and transparency losses, as a larger bandgap would lead to reduced thermalziation losses but increased transmission losses. This tradeoff leads to an optimal bandgap of around 1.3 eV with an ideal conversion efficiency of approximately 29 % for unconcentrated terrestrial sunlight, as originally derived by Shockley-Queisser (SQ limit)[6]. As shown in Figure 1.3[4], research c-Si cells have approached the S-Q efficiency limit, although the typical module efficiency is 18 %. While triple junction concentrator cells (CPV-3J) in Figure 1.3 have module efficiencies of 31 %, the cost is too high for terrestrial applications. Significant technological innovation is required to achieve the goal of 25 % commercial module efficiency at a competitive cost, and the intermediate band solar cell (IBSC) is one idea that may meet this goal.

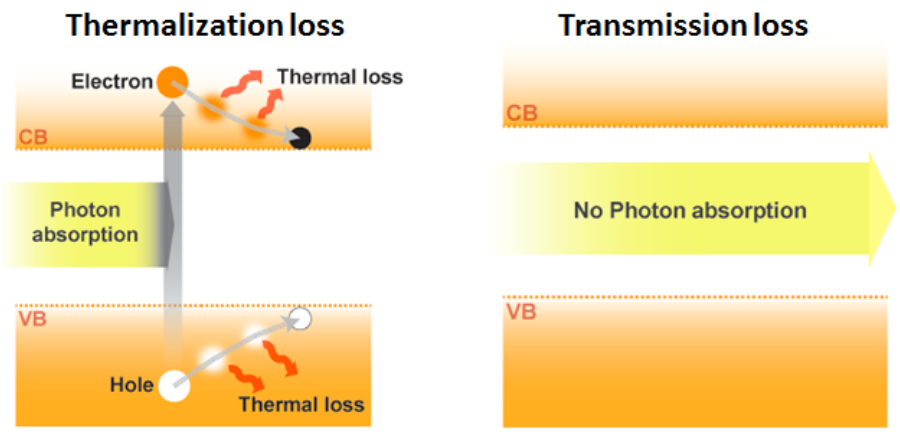

Figure 1.2 Depiction of thermalization and transmission losses in photovoltaic cells, which are the primary losses limiting the conversion efficiency of single-junction solar cells.

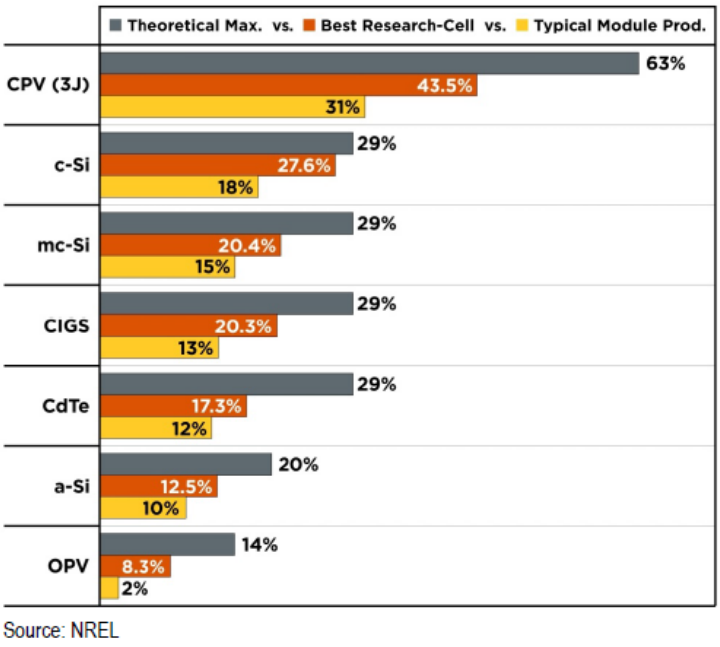

Figure 1.3 Solar cell efficiencies for primary PV production technologies[4].

1.4 Historical Developments and Economics of Solar Cells

There has historically been two major generations of solar cell technologies, as shown in Figure 1.4[7]. The first generation was single crystal materials, in particular Si.

As the technology matured, the manufacturing cost became increasing limited by the cost of the raw material, namely the single crystalline substrates. The direction of the technology therefore moved towards the development of a technology that used cheaper raw materials. The second generation technology is uses raw materials that absorb light strongly, so a that a poly-crystalline or amorphous thin film on a low-cost substrate may be used, which are cheaper to prepare than single crystalline substrates[7]. A reduction in efficiency is expected for the thin film technologies due to the lower quality materials, but also a price reduction due to the cheaper semiconductor raw materials, as shown in Figure 1.4.

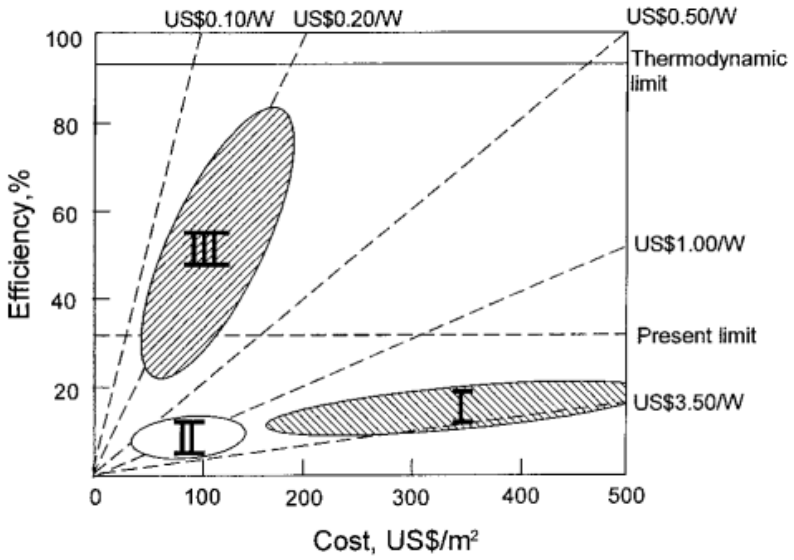

Figure 1.4 The three generations of solar cell technology development, namely single crystalline silicon, thin film, and above Shockley-Queisser efficiency limit[7].

Economically speaking, solar cell modules that include the first and second generation technologies have been decreasing in price from 1980-2001 largely due to economies of scale, where cost reduction was related to the increased production volume as opposed to improvement of technology, as shown in Figure 1.5 [4]. As of 2011, the

solar cell module cost is typically 1.5-2 $/W, and in the United States, the final cost of utility scale electricity in 2010 is approximately 3.8-4.4 $/W, as shown in Figure 1.6. As discussed in Chapter 1, there is broad consensus in the scientific community that recommends rapid reduction in the production of greenhouse gases to prevent the global mean temperature from rising above 2^{o} C from 1900 levels. As such, the U.S. Department of Energy's SunShot study recommends that solar cell module final cost should reach 1 $/W by 2020, making it cost competitive with other forms of electricity generation[4]. Following the historical solar cell module prices, the cost is expected to continue to decrease through gradual improvements and further economies of scale, as shown in Figure 1.7. However, Figure 1.7 also shows that this evolutionary approach to reducing the cost of first and second generation technologies is not fast enough to address climate change.

Therefore, attention is now focused on developing new technologies that will substantially increase the efficiency of the solar cell modules. This is termed the third generation technology. As shown in Figure 1.4, third generation technology aims to increase the efficiency beyond the Shockley-Queisser limit shown in Equation 1-5. The remaining sections in this chapter describe the three generations of solar cell technologies.

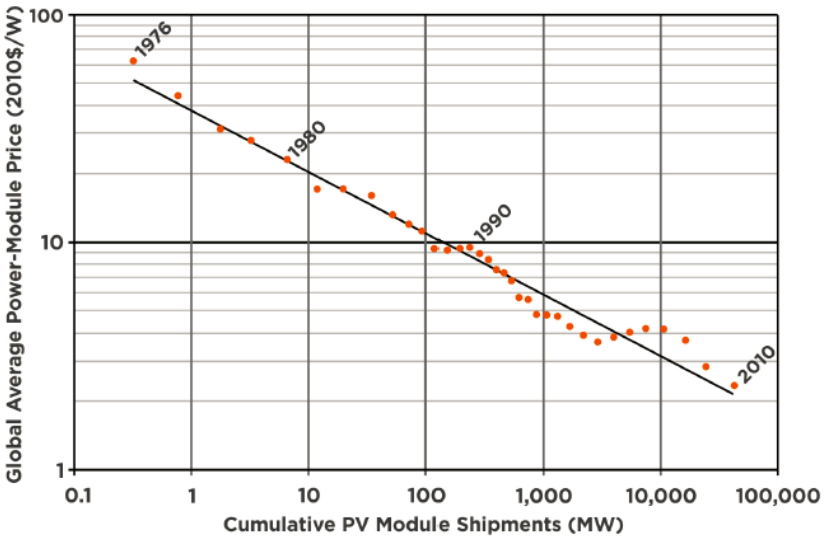

Sources: Mints (2011), Mints (2006), Strategies Unlimited (2003)

Figure 1.5 Solar energy historical price reduction primarily due to economies of scale[4].

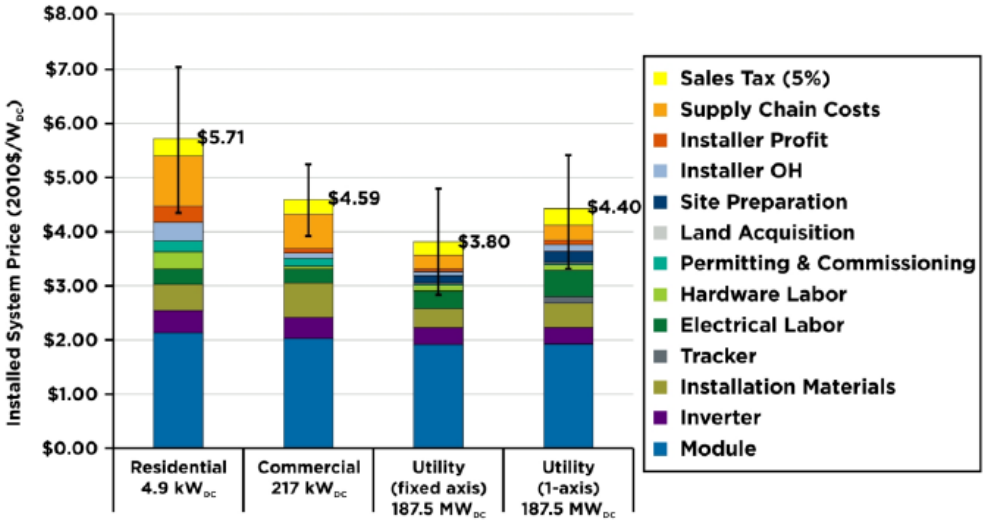

Source: Goodrich et al. (2012)

Figure 1.6 The cost break down of solar electricity[4].

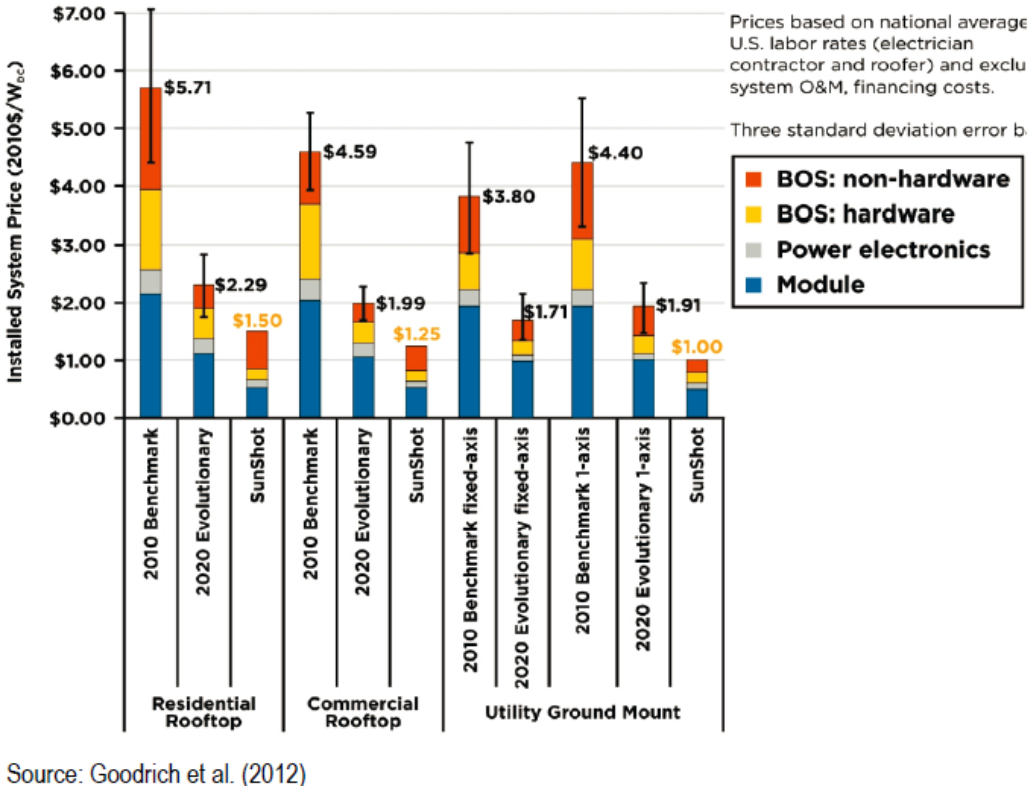

Source: Goodrich et al. (2012)

Figure 1.7 Comparison between the SunShot target needed to be achieved by 2020 to prevent global mean temperature from rising 2º C pre-industrialization levels and the price reduction due to evolutionary changes (economies of scale) [4].

1.5 Limits to efficiency

Efficiency limits are useful in understanding how much energy extraction is theoretically possible from an energy source. The calculated efficiency limits depend on the assumptions about the work extraction device. The discussion in this Chapter is mainly based on the text book "The Physics of Solar Cells" by Jenny Nelson[8].

The most efficient possible heat engine is one that employs the Carnot cycle, in which no entropy is created as the heat engine operates between the hot temperature body T_{Hot} and the cold temperature body T_{Cold}. For such a heat engine, the energy conversion efficiency is

$$\eta_{Carnot} = 1 - \frac{T_{cold}}{T_{hot}}$$ **Equation 1-1**

In the case of a solar cell, there are three relevant temperatures: temperature of the sun T_S, temperature of the solar cell T_C, and the temperature of the ambient environment to the solar cell T_A. In the ideal case that the solar cell is a Carnot engine, it would convert the heat transfer from the cell to the ambient Q_{C-A} to useful work W with the Carnot efficiency in Equation 1-1.

$$W = Q_{C-A}\left(1 - \frac{T_A}{T_C}\right)$$ **Equation 1-2**

In steady state, net energy entering the solar cell must leave the solar cell as heat transfer or work production. The net energy entering the solar cell, Q_{C-A}, is the radiation incident on the solar cell from the sun minus the radiation the solar cell emits due to its characteristic temperature T_C. Modeling both as black body sources,

$$Q_{C-A} = \sigma_S T_S^4 - \sigma_C T_C^4$$ **Equation 1-3**

where σ_S is the Stefan-Boltzmann constant. Defining efficiency as work produced with respect to radiation from the sun:

$$\eta = \frac{W}{\sigma_S T_S^4} = \left(1 - \left(\frac{T_C}{T_S}\right)^4\right)\left(1 - \frac{T_A}{T_C}\right)$$ **Equation 1-4**

Given the temperature of the sun of $T_S = 5760\ K$ and typical ambient temperature of 300 K on earth, Equation 1-4 gives rise to a maximum efficiency of 85 % for $T_C = 2470\ K$. We note that $T_C = 2470\ K$ for a solar cell in thermal contact with its environment is not

realistic, although a system with radiative heat transfer with the sun and it's ambient, but suppressed conductive and convective heat transfer with its ambient may presumably reach such high temperatures.

When considering strategies to generate electricity, entropy is often generated, and so the ideal efficiency would be lower than that of the Carnot heat engine given above. The single junction solar cell is first and most common photovoltaic device structure. The single junction cell is based on a semiconductor with a defined bandgap, as shown in Figure 1.8. A photon with energy larger than the bandgap promotes an electron into the conduction band. Some of the kinetic energy of the electron is then lost to the lattice as heat during the thermalization process, and the electron relaxes to the conduction band edge. The thermalization process is irreversible, generates entropy, and therefore the single junction cells have an ideal efficiency lower than the Carnot engine case in Equation 1-4.

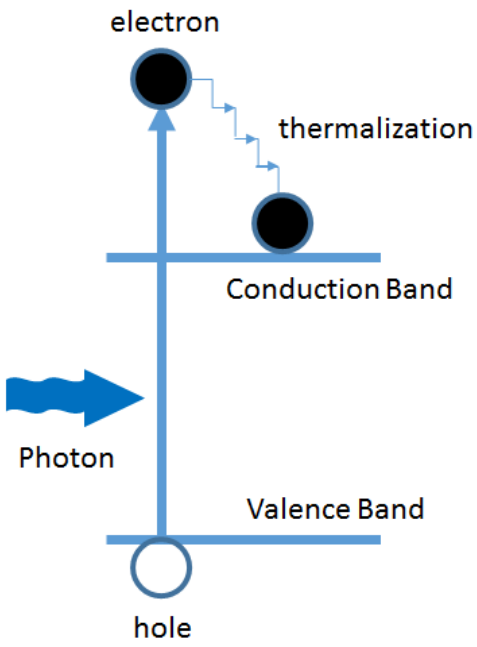

Figure 1.8 The two main loss mechanisms of the traditional single junction cell: thermalization and transparency.

Transparency is another loss mechanism. As shown in Figure 1.8, photons with energy insufficient to bridge the bandgap of the semiconductor would not be absorbed, leading to transparency loss. The thermalization and transparency losses together reduce the ideal efficiency to

$$\eta = \frac{E_G \int_{E_G}^{\infty} b_S(E)dE}{\int_{E_G}^{\infty} E b_S(E)dE} \qquad \textbf{Equation 1-5}$$

where E_G is the bandgap of the semiconductor, and b_S is the black body spectrum of the sun. Equation 1-5 assumes that all above bandgap photons incident on the solar cell is converted to electrical current, collected at a voltage equivalent to E_G/q, where q is the fundamental charge. As will be discussed in later sections, E_G/q is the largest voltage that can reasonably be collected from a single junction solar cell. Equation 1-5 is known as

the Shockley-Queisser limit[6], with an efficiency value 44 % a full concentration (where the sun covers in the entire sky) for a 6000 K blackbody sun and a semiconductor bandgap of 1.1 eV.

In a more updated calculation that accounts for the rectifying behavior of an ideal solar cell device J-V characteristic by modeling the recombination photon flux emitted from the solar cell with the generalized Planck's law[8], it has been calculated that an ideal solar cell would have a maximum efficiency of approximately 33 % with a bandgap of approximately 1.4 eV under AM1.5 illumination[8]. Figure 1.9 [9] shows calculated limiting efficiencies for a single junction solar cell for 1 blackbody Sun and full concentration illumination using such a model. In this calculation, the solar cell efficiency maximizes at around a bandgap of approximately 1.3 eV for 1 blackbody Sun concentration. Below this bandgap, thermalization losses dominate, and above this bandgap, transparency losses dominate.

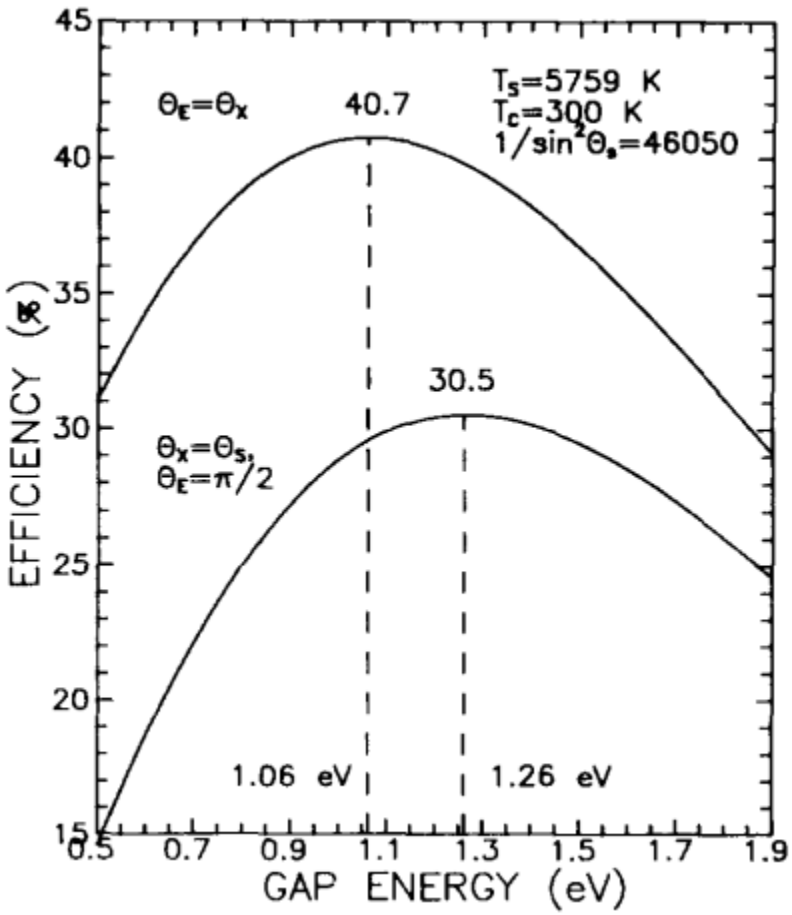

Figure 1.9 Calculated limiting efficiencies for a single junction solar cell for 1 blackbody Sun and full concentration illumination[9].

1.6 Origins of photovoltaic action

As outlined in the previous section, single junction solar cells are based on semiconductors, which are materials with a bandgap size of around 0.5-3 eV. When an the semiconductor absorbs light, electrons gain potential energy and is promoted from the valence band to the conduction band, as shown in Figure 1.10. The electron losses energy to the lattice in the femtosecond time scale through thermalization. This energy loss is much faster than the time it takes to collect the carriers in single junction devices. The bandgap prevents further thermalization, which requires closely spaced energy states

comparable to the phonon energy. At the band edge, the electron further loses potential energy through radiative recombination, which is a much slower process, with a time scale on the order of μs. This is sufficient time for the electron to be collected before further losing its potential energy. The higher the electron potential energy, the lager the output voltage to the external circuit.

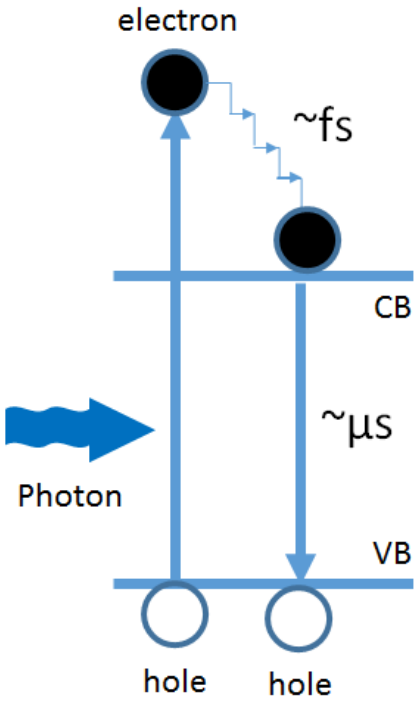

Figure 1.10 Time scale of thermalization is much shorter than radiative recombination, justifying modeling carriers at the band edges with quasi-Fermi levels.

To convert solar energy into electrical work, we need to the device to generate electrical current. Light incident on a uniform semiconductor does not generate substantial current. Electron and hole pairs would be generated, and both electrons and holes would diffuse towards regions with lower electron and hole concentrations, as show in Figure 1.11. While carrier diffusion leads to current, both electrons and holes diffuse in

the same direction, so if the diffusion constants are the same, there would be no net current; only small current can be expected that results from differences in electron and hole diffusion constants.

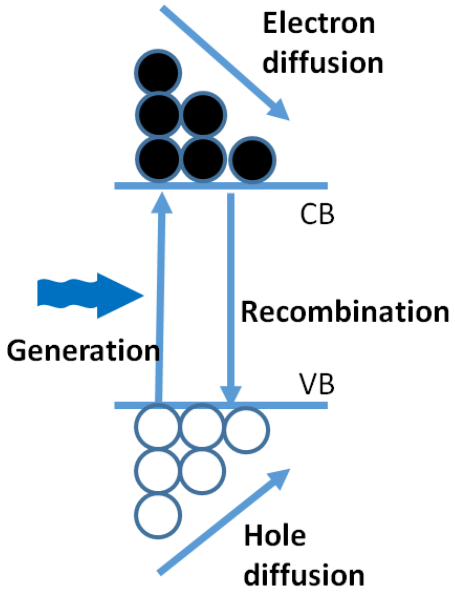

Figure 1.11 Diffusion in an uniform semiconductor. While the spatial asymmetry set up by the light field generates electron and hole currents, this does not lead to net current. Instead, regions that selectively collects electrons or holes are required to generate net current.

Before reaching a strategy to generate net current in the semiconductor, it is useful to consider the general mathematical expressions describing electron and hole current in a semiconductor, as follows:

$$J_n(\bar{r}) = -\frac{q\hbar}{m_C^*}\int_{CB} \bar{k} g_c(\bar{k}) f(\bar{k},\bar{r}) d^3\bar{k}$$ **Equation 1-6**

$$J_p(\bar{r}) = -\frac{q\hbar}{m_V^*}\int_{VB} \bar{k} g_V(\bar{k}) \{1 - f(\bar{k},\bar{r})\} d^3\bar{k}$$ **Equation 1-7**

for electrons and hole, respectively. Here, $\boldsymbol{k}$ is the momentum vector, g is the density of electronic states in the conduction of valence band, m is the effective mass in the conduction or valence band, and q is the fundamental charge. Since the momentum divided by mass is velocity, the expressions essentially sums the velocities of all the electrons or holes in the semiconductor, and that sum is directly proportional to the electrical current carried by electrons or holes. Since $\boldsymbol{k}$ is antisymmetric, g is symmetric (since the bottom of any stable potential well is approximately parabolic), f has to be antisymmetric if there is to be electrical current.

In equilibrium, the semiconductor by definition does not generate current, and so the electron distribution function in equilibrium f_o is an even function of space. f_o is the known as the Fermi-Dirac distribution:

$$f_o\left(E, E_F, T\right) = \frac{1}{e^{(E-E_F)/k_B T} + 1} \qquad \textbf{Equation 1-8}$$

When sunlight illumination is introduced, the semiconductor is no longer in equilibrium. Once the carriers have thermalized to the conduction and valence band edges, they may be relatively long lived, as shown in Figure 1.10. In semiconductor device physics, it is assumed that the carriers are long lived enough to reach a quasi-thermal equilibrium that that is roughly described by the functional form of f_o, but with a characteristic temperature and Fermi energy, as in $f_o(E, E_{Fn}, T_n)$ and $f_o(E, E_{Fp}, T_p)$ for electron and holes, respectively. The addition of a spatially asymmetric term is further assumed to allow for the possibility for electrical current. For example, the conduction band in quasi thermal equilibrium is modeled by:

Equation 1-9

$$f_C(\bar{k},\bar{r}) = f_o\left(E, E_{Fn}, T_n\right) + f_A(\bar{k},\bar{r})$$

Since we assume for the possibility of electrical current, we can apply the Boltzmann's transport equation to investigate what the conduction band distribution $f_c(\boldsymbol{k},\boldsymbol{r})$ may look like:

Equation 1-10

$$\frac{df_C}{dt} = \frac{d\bar{r}}{dt}\cdot\nabla_{\bar{r}} f_C + \frac{d\bar{k}}{dt}\cdot\nabla_{\bar{k}} f_C + \frac{\partial f_C}{\partial t}$$

We further assume that the distribution function exponentially evolves towards the quasi equilibrium distribution function with a characteristic time τ. This is called the relaxation time approximation:

Equation 1-11

$$\frac{\partial f_C}{\partial t} = -\frac{f_C - f_o}{\tau}$$

With this we find the antisymmetric part of the distribution function f_A

Equation 1-12

$$f_A = -f_o \frac{\tau\bar{v}}{k_B T}\nabla_{\bar{r}} E_{Fn}$$

Substituting this into Equation 1-6, and doing a similar analysis for the valence band, we obtain

Equation 1-13

$$J_n(\bar{r}) = \mu_n n \nabla_{\bar{r}} E_{Fn}$$

Equation 1-14

$$J_p(\bar{r}) = \mu_p p \nabla_{\bar{r}} E_{Fp}$$

If we further assume the Boltzmann approximation, where the distribution function is exponential in form, we can decouple the drift and diffusion components of the current:

Equation 1-15

$$J_n(\bar{r}) = qD_n \nabla n + q\mu_n Fn$$

Equation 1-16

$$J_p(\bar{r}) = -qD_p \nabla p + q\mu_p Fp$$

, where n and p are the electron and hole concentrations, μ is the mobility, D is the diffusion coefficient, and F is the electric field. Electron and hole current therefore require a spatial asymmetry in the quasi Fermi level, carrier concentration or electric field. Hence the reason that the case shown in Figure 1.11 would generate electron and hole current because the light field set up a gradient in the carrier concentration. As mentioned earlier, the case shown in Figure 1.11 would not lead to significant net current, because both electron and hole currents are collected in the same space. Therefore, to generate net electrical current from the device, the device also needs to selectively collect electron or hole current in most locations of the device.

Solar cells have finite spatial dimensions. Here we continue the discussion of light and semiconductor interaction in the previous section, but also taking into account space. When light is absorbed by the semiconductor, the photon's energy is converted into the potential energy of electrons and holes, as shown in Figure 1.8. Quantitatively, the number of electron hole pairs generated as a function of depth from the top surface (x) can be modeled by the Beer-Lambert law:

Equation 1-17

$$\frac{dI}{dx} = -\alpha I$$

, where I is the light intensity and α is the absorption coefficient of the material. The number of electron hole pairs generated at x per unit volume, $g(x)$, is thus

Equation 1-18

$$g(E,x) = \{1 - R(E)\}\alpha(E)b_S(E)e^{-\alpha(E)x}$$

, where $R(E)$ is the fraction of light reflected at the surface, $b_S(E)$ is the incident photon flux, and E is the energy of the photon.

Once the electron hole pairs are generated, the quickly thermalize to the conduction band edge, as shown in Figure 1.10. They then diffuse in space towards locations with lower electron and hole concentration until they eventually recombine. The amount of time on average for minority carriers to recombine is expressed as the minority carrier lifetime τ. It is often a good approximation that the carriers relax exponentially in time, in which case the total lifetime is the inverse sum of the radiative non-radiative recombination lifetimes:

Equation 1-19

$$\frac{1}{\tau} = \frac{1}{\tau_r} + \frac{1}{\tau_{nr}}$$

In general, it is desirable to have a long carrier lifetime, so that they have a higher chance of being collected before recombining. As shown in Equation 1-19, the process with the shorter time would dominate the overall lifetime. Radiative recombination is unavoidable, and in most materials, radiative lifetime does not dominate the overall lifetime. Non-radiative recombination processes have shorter lifetime compared to

radiative lifetime. Non-radiative recombination is typically associated with imperfections in the semiconductor crystal, such as dislocations or impurities. It is therefore important to find ways to increase the non-radiative recombination lifetime.

The amount of distance they diffuse before recombining on average can be modeled by the diffusion length

Equation 1-20

$$L_{diff} = \sqrt{\tau D}$$

, where D is the diffusion constant and τ is the carrier lifetime. This assumes an exponential decrease in electron and hole concentration with increasing distance from the point of carrier generation. One goal of device design is therefore to collect the light generated carriers within the diffusion length of the carriers.

A consequence of the selectivity in collecting holes or electrons only in a particular device region is that the device would exhibit rectifying behavior, as in current flows preferentially in one spatial direction. The circuit element that exhibits rectifying behavior is a diode, and a solar cell can therefore be conveniently modeled as a current source and a diode in parallel, as shown in the circuit diagram in Figure 1.12.

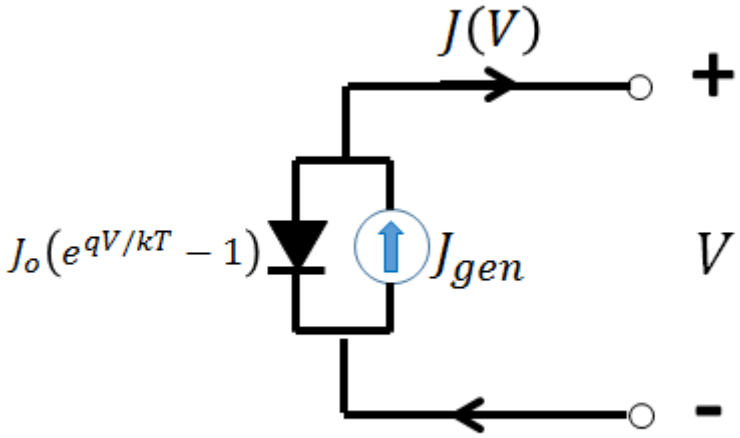

Figure 1.12 Simple circuit model of the single junction solar cell.

The diode is modeled by the ideal diode equation:

$$J(V) = J_o\left(e^{\frac{qV}{k_B T}} - 1\right) \qquad \textbf{Equation 1-21}$$

The rectifying behavior of the diode is demonstrated by the dark curve in Figure 1.13, plotted for the case of J_o is the leakage current at 10^{-14} mA/cm^2, *T=300 K*. No diode is completely rectifying, and Figure 1.14 plots the dark J-V curve in log scale to resolve the leakage current in reverse bias.

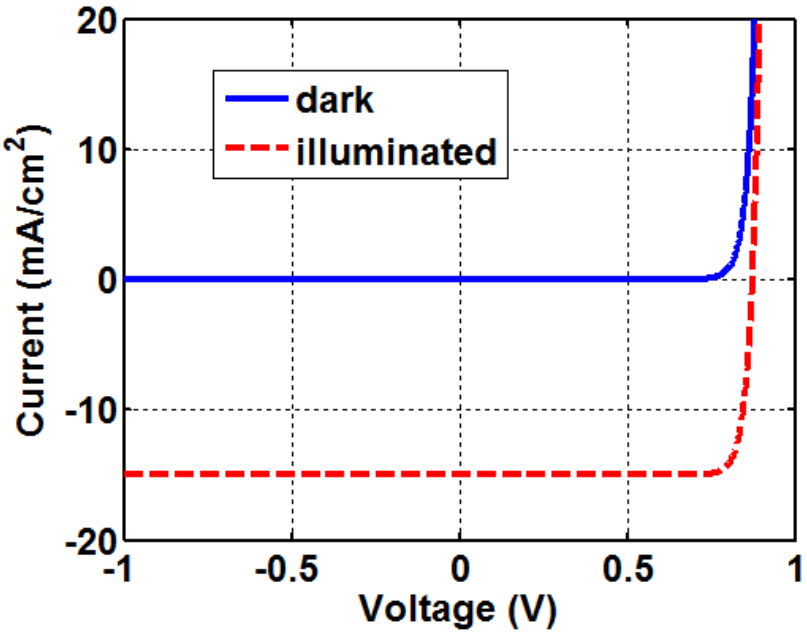

Figure 1.13 Model output of the simple circuit model of the solar cell shown in Figure 1.12.

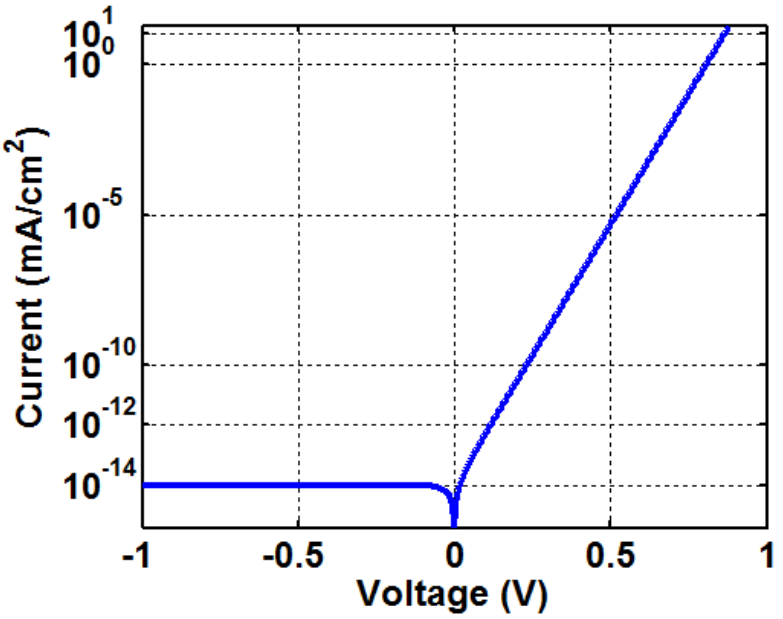

Figure 1.14 Leakage current is small but non-zero in reverse bias condition.

If we further assume the superposition condition, where illumination does not alter the characteristics of the diode structure, then the circuit diagram in Figure 1.12 is valid, and we can model light the effect of light illumination on a solar cell as:

$$J(V) = -J_{SC} + J_o\left(e^{\frac{qV}{k_B T}} - 1\right)$$ **Equation 1-22**

, where J_{SC} is the short circuit current representing the maximum light generated current. The case of $J_{SC} = 10\ mA/cm^2$ is plotted in the light curve in Figure 1.13. For solar cells, the region of interest on the J-V curve is the 4th quadrant (positive current, negative voltage), as that is the quadrant with net power output to the external load.

1.7 Junctions

As shown by Equation 1-13, Equation 1-14, generation of electron or hole current requires a spatial asymmetry in the electron and hole quasi Fermi level, and Figure 1.11 shows that to get net current output, the device needs to selectively collect either electron or hole current in most regions. One way to simultaneously achieve the above two requires for net current generation is to employ junctions. Junctions form when semiconductors of different work function, electron affinity, bandgap, or density of states are brought together. These factors are spatially asymmetric, and simultaneously separate the electrons and holes so that they can be selectively collected in different regions. The most common junction used in solar cells is the p-n junction, where semiconductors of different work function but identical otherwise are brought together to from a junction. This is discussed in the next section

The p-n junction is formed when a semiconductor is doped p-type on one side of the junction and n-type on the other, making it low resistivity for only either electrons or holes on each region. This allows for selective collection of electrons or holes. The junction also leads to a built-in electric field, which satisfies the spatial asymmetry

requirement for generating net electrical current. Figure 1.15 shows the band diagram of a p-n junction in equilibrium. As shown, and electrostatic field is setup in the region near the junction between the p-type and n-type material. Since most of the voltage drop occurs there, we can deduce that region is highly resistive, hence it is often assumed that the region is completely depleted of free charge carriers, and named the "depletion region".

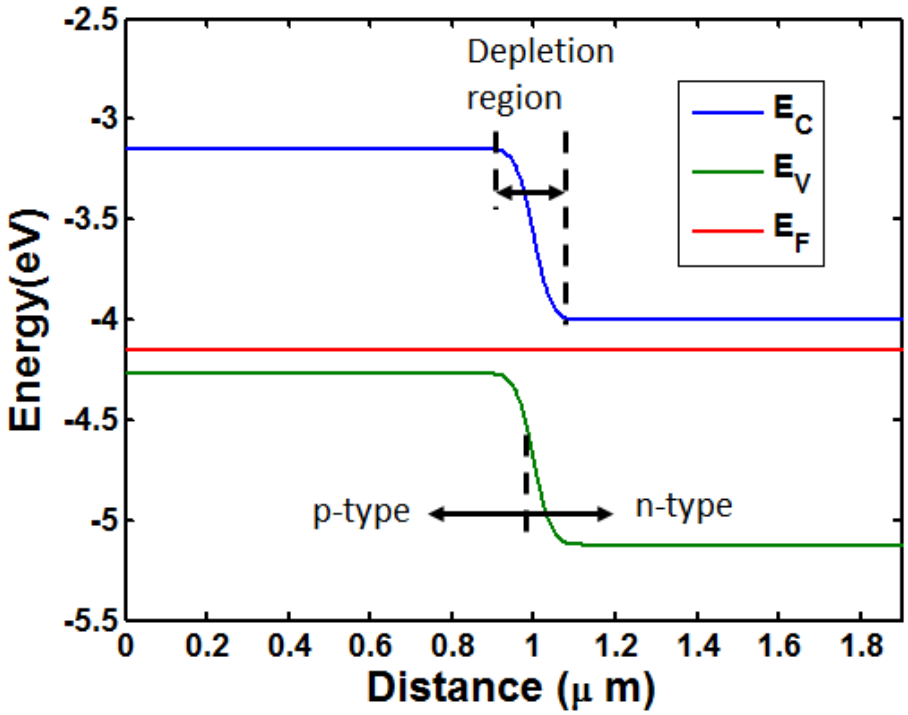

Figure 1.15 Band diagram of a p-n junction in the dark and thermal equilibrium. Simulation by AMPS-1D[5]

The electric field in the depletion also leads to charge separation of electron and holes, so that they can be selectively collected as minority carriers when biased by light illumination. Figure 1.16 shows the band diagram of a p-n junction under illumination, at an operation point where net current is being collected. The semiconductor is no longer at equilibrium, and after the carriers have thermalized to the band edges, these relatively long-lived populations are modeled by quasi-Fermi levels as shown in Equation 1-9. As

shown in Equation 1-20, the Fermi level splits into E_{Fn} and E_{Fp}, and the output voltage of the device is given by $V_{applied} = q\,(E_{Fn} - E_{Fp})$.

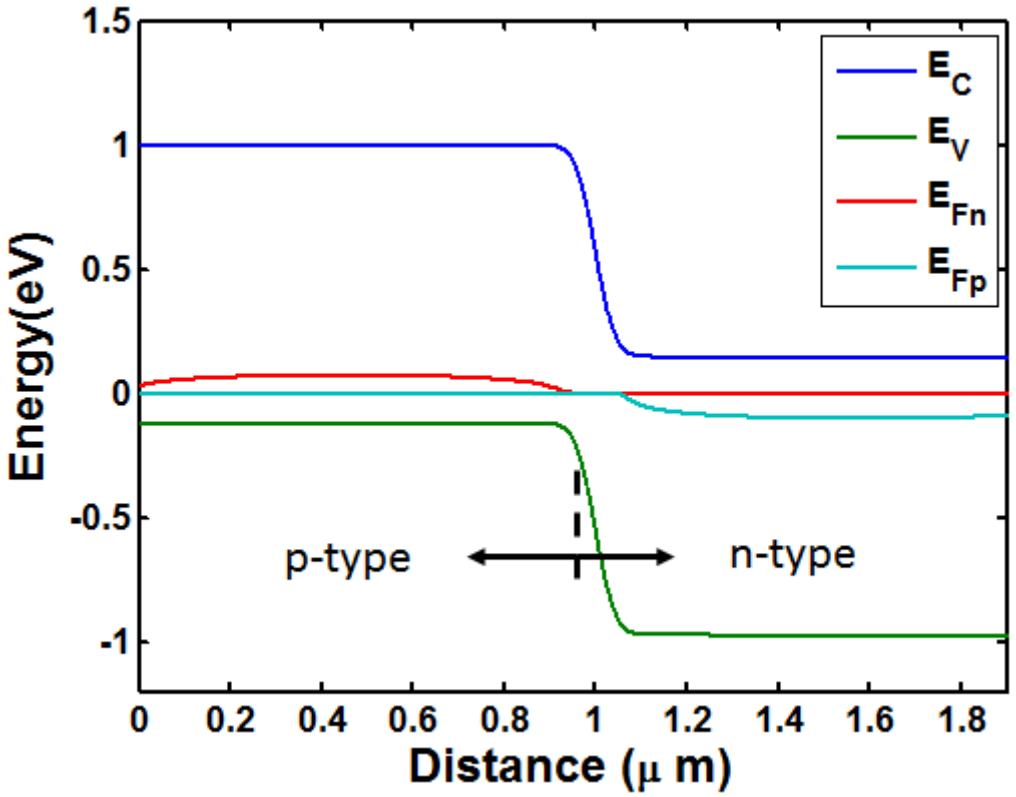

Figure 1.16 p-n junction under light illumination, at the short circuit condition. Simulation by AMPS-1D[5]

This is a minority current device where the minority carriers are collected by diffusion in the p and n regions, and by drift in the depletion region. The electric filed in the space charge region collects the minority carriers while blocking the majority carriers, so the large diffusive currents for minority carriers in the nearly neutral regions occur, and significant diffusive current for the majority carriers is prevented. This selective collection of minority carriers solves the problem outlined in Figure 1.11.

1.8 Single crystal solar cells (1st gen)

As mentioned in the previous chapter, historically there has been three generation of solar cell technology develop. The following sections briefly discuss each.

Single crystalline solar cells are devices based on the p-n junction device structure. The device needs to be thick enough to absorb all the incoming photon. Since in p-n junction devices the minority carriers needs to reach the junction to be collected, the diffusion length needs to be larger than the absorption length in single crystalline solar cells. This means that the material quality for the crystals has to be very high- this is true for the substrates such as Si and GaAs, which have been well developed by the microelectronics and optoelectronics industries. Since bandgaps of Si (1.1 eV) and GaAs (1.4 eV) is close to the optimal bandgap for solar radiation (1.4 eV)[8], these materials have been developed for solar cells. The following sections briefly describe these technologies.

Single crystalline cells typically have an n on p device structure, where the n-type material is on the top surface facing the illuminations source. The top layer is typically called the emitter, and the bottom layer is typically called the base. The absorption coefficient of Si is relatively low, on the order of 1000 cm^{-1} for most of the solar spectrum, so a lot of material, typically a few hundred microns, is needed to fully absorb the solar spectrum. Since the absorption coefficient is about an order of magnitude higher for short wavelengths, these high energy photons are absorbed completely near the top surface, therefore the junction depth should be shallow to collect them. The emitter is therefore typically thin, approximately 0.5 μm. The emitter is also typically highly doped to raise the open circuit voltage of the cell, since the open circuit voltage depends on the

work function difference between the emitter and base. The high doping also reduces the series resistance in the very thin emitter. Since the diffusion length decreases with doping, the base is typically lightly doped, on the order of 10^{16} cm^{-3}, and quite thick, approximately 300 μm, to fully absorb the solar spectrum, and have the carriers diffuse the length of the base to the junction. The n emitter and p base structure is typically chosen because electron diffusion length in p type material is longer than hole diffusion length in n type material, an important consideration as the base is very thick.

The absorption coefficient of GaAs is approximately 10 times larger than that of Si for most of the visible spectrum, and so the base in GaAs only needs to be a few microns thick to fully absorb the available solar spectrum. The base in Si cells instead 100 times longer than that in GaAs because Si also absorbs near IR light, and the absorption coefficient there is very weak, on the order of 10 cm^{-1} to 100 cm^{-1}. The diffusion length is longer than the absorption length for both n and p type materials, so both polarities of n on p or p on n structures are possible. The device structure features a thin and highly doped emitter of approximately 0.5 μm to collect the short wavelength carriers and reduce series resistance, and a thicker base of approximately 2-4 μm to fully absorb the solar spectrum. Being a compound semiconductor, GaAs III-V material system allows for the possibility of near lattice matched bandgap engineering. For example, a larger bandgap layer of AlGaAs can serve as a window layer to reflect the carriers away from the defective metal semiconductor surface interface. Like the case for Si, the raw material cost is a limiting factor for this technology. While the active solar cell is much thinner, it is grown on thick GaAs substrates, which is approximately 10 times more expensive than Si substrates.

1.9 Thin film solar cells (2nd gen)

Since the major drawback of the first generation technologies was the cost of the raw materials, the second generation, thin film, technologies aimed to use cheaper raw materials in less quantities. The materials are of amorphous or poly-crystalline quality, so they are cheaper to produce. These materials also have approximately 10 times higher absorption coefficients compared to Si, so that less material need is necessary. Also, the thin films can be deposited on cheap substrates such as glass for mechanical stability. The lower material quality leads to short diffusion lengths of approximately 0.1 μm, which is shorter than the absorption length of a few μm, so that the p-n junction device structure does not work, because it relies of diffusion to collect carriers. Instead, the p-i-n device structure is used to extend the electric field over the active carrier generation region, so that the carriers can be collected by drift. The following discusses the p-i-n device structure.

Figure 1.17 compares the p-n device structure with the p-i-n device structure. As shown, the p-i-n device structure extends the electric field across the "i" region, which is insulating. If the "i" region is completely insulating, the electric field would not expose net space charge to neutralize the field, and the built-in voltage would drop uniformly across the "i" region, as shown in Figure 1.17.

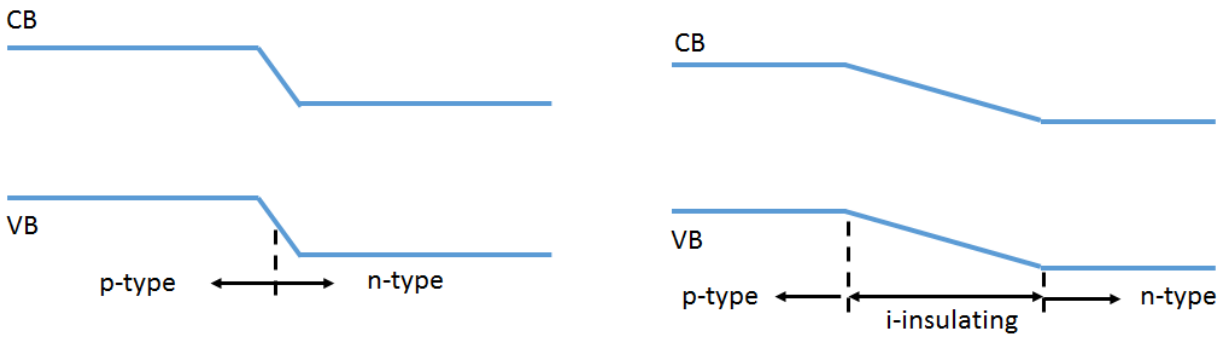

Figure 1.17 p-n junction compared with the p-i-n junction. The p-i-n junction extends the electric field over the i region.

Drift in metals is related the net velocities of carriers taking into account the collisions and the electric field experienced, and this is modeled by carrier mobility. In semiconductors, there's another factor, namely that carriers also recombine, and so we define an effective drift length that also takes into account recombination lifetime:

Equation 1-23

$$L_{drift} = \mu\tau E_i$$

where μτ is the average mobility lifetime product for minority electron and holes[10], and

Equation 1-24

$$E_i = \frac{V_{bi} - V_a}{x_i}$$

, where V_a is the applied bias, x_i is the length of the "i" region, and it is assumed that the field extends through the "i" region. With the aide of Equation 1-23, one way to think about carrier collection by drift in semiconductors is as follows: once the minority carrier is generated it would recombine after τ. The electric field can move the carrier by L_{drift} before it recombines. Therefore the minority carrier needs to be collected by entering a

region where it becomes a majority carrier. When $x_i > L_{drift}$ some of the carrier generated in the "i" region is lost, as if the region has increased series resistance.

Thus far we assumed that the electric field extends throughout the "i" region. Another design concern for the p-i-n structure is that the electric field may not extend throughout the "i" region fully, forming an undepleted region that would rely on diffusion for carrier collection, as shown in Figure 1.18. This can happen if the "i" region has some background doping concentration. An undepleted region longer than the diffusion length (~0.1 μm in many thin film materials) would significantly reduce carrier collection. This limits the design of most "i" regions to approximately 0.5 μm in thickness.

At high injection, such as concentrated sunlight conditions, the space charge would completely eliminate the electric field in the space charge region, as shown in Figure 1.19. Here, carrier collection relies on diffusion, and the charge separation occurs at the p-i and i-n interfaces. Some common second generation solar cell materials include amorphous Si, CdTe, $CuInSe_2$, and $CuInGaSe_2$.

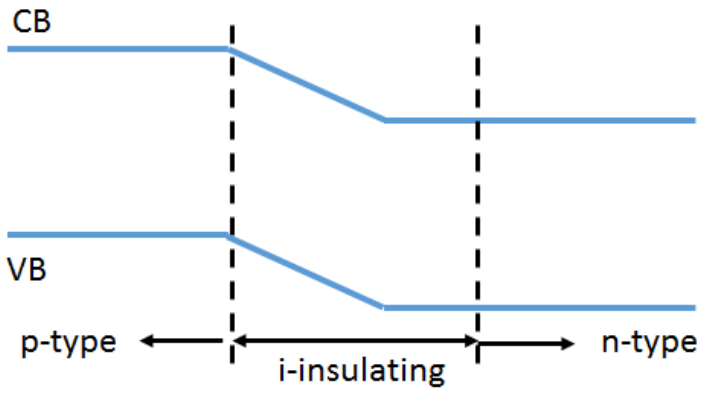

Figure 1.18 p-i-n junction with an undepleted i region.

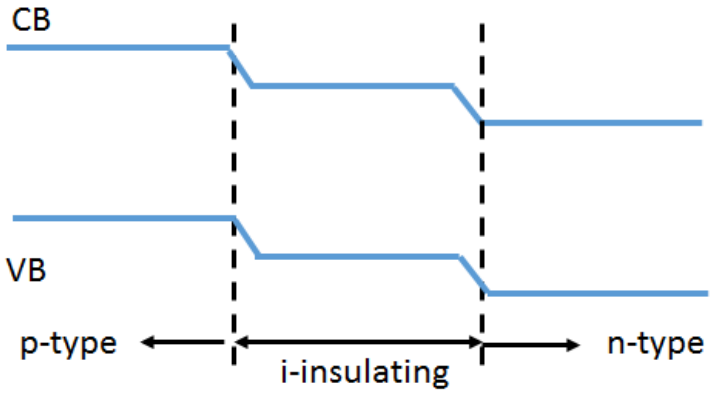

Figure 1.19 p-i-n junction where the electric field in the i region is zero, due to compensation by the charges of ionized dopants and/or carriers. Collection relies on diffusion, and occurs at the p-i and i-n interfaces.

1.10 Beyond the SQ limit (3rd generation)

As discussed earlier, dramatic increases in solar cell technology or manufacturing technology (as opposed to evolutionary improvement associated with economies of scale), is needed to make solar power cost effective compared to fossil fuels in time for prevent a 2^{o} C increase in global mean temperature. This section focuses on ideas that go beyond the Shockley-Queisser (SQ) efficiency limit shown in Equation 1-5. The following equations and discussion are based on [8].

The SQ limit shown in Equation 1-5 assumed two major loss mechanism, namely thermalization to the semiconductor band edge, and transparency for photons not energetic enough to bridge the bandgap. To go beyond the SQ limit we need to simultaneously reduce the thermalization and transparency losses. These are the so called third general solar cell ideas. As shown in Figure 1.4, third generation concepts aim to keep the cost low while being more efficient than the SQ limit that bounds the concepts from the first and second generation. To aid the calculation of the theoretical maximum efficiency of the following third generation ideas, it is useful to define the following functions:

$$N(E_{\min}, E_{\max}, T, \Delta\mu) = \frac{2\pi}{h^3 c^2} \int_{E_{\min}}^{E_{\max}} \frac{E^2}{e^{(E-\Delta\mu)/k_B T} - 1} dE \qquad \textbf{Equation 1-25}$$

$N(E_{min}, E_{max}\ T, \Delta\mu)$ is proportional to the generalized Planck's law (the integrand) that describes the blackbody spectrum when $\Delta\mu=0$, and describes the emission spectrum of a semiconductor out of equilibrium with its quasi-Fermi levels split by the amount $\Delta\mu$. The pre multiplying factor makes the units of $N(E_{min}, E_{max}\ T, \Delta\mu)$ inverse area, so this function describes photon flux.

$$L(E_{\min}, E_{\max}, T, \Delta\mu) = \frac{2\pi}{h^3 c^2} \int_{E_{\min}}^{E_{\max}} \frac{E^3}{e^{(E-\Delta\mu)/k_B T} - 1} dE \qquad \textbf{Equation 1-26}$$

$L(E_{min}, E_{max}\ T, \Delta\mu)$ describes the energy flux carried by the photons. We also introduce the f_s, the solid angle subtended by the sun as viewed from Earth. To simplify the analysis, we neglect the effects of atmospheric absorption, and model the radiation spectrum with the generalized Planck's law (the integrand in Equation 1-25). The maximum efficiency for the single junction cell described in the previous sections can be

calculated by the following. The solar cell accepts photon flux from the Sun and from the environment at the temperature of the Sun T_S and temperature of the ambient T_a, respectively, and emits radiation with characterized by its Fermi level splitting $\Delta\mu$ and T_a. Assuming that $\Delta\mu = V$, the operating voltage, the power output of the cell is:

$$P(V) = V \times qX\{ f_S N(E_G, \infty, T_S, 0) + (1 - Xf_S) N(E_G, \infty, T_a, 0) \quad \textbf{Equation 1-27}$$

$$- N(E_G, \infty, T_a, qV)\}$$

Here, X is the concentration of the sun. For one sun concentration, $X = 1$, the maximum power point is maximized for a bandgap E_G of 1.3 eV, with an efficiency of 31 %, as discussed previously. The following sections describe the major third generation ideas, namely multijunction, intermediate band, hot carrier, and impact ionization solar cells.

With a single junction, there is a tradeoff between the thermalization and transparency losses. Larger bandgap would decrease thermalization loss but increase transparency loss, and vice versa. One way to view the SQ limit is the optimum power point of this trade off. One way to get around this tradeoff is to use bandgaps of different sizes in series. The larger bandgap would collect the higher energy photons, thereby reducing thermalization losses, and the transparent photons would be absorbed by a smaller bandgap downstream.

For two junctions with two different bandgaps connected in series, each junction would ideally operate at their respective bandgaps, the output voltage would be the sum of that of the two junctions, and the current from the two junctions would be matched (series connection). The power output at full concentration of a two junction cell would therefore be:

Equation 1-28

$$P(V) = q(V_1 + V_2)\{N(E_{G1}, E_{G2}, T_S, 0) - N(E_{G1}, E_{G2}, T_a, qV_1)\}$$

, where the subscripts denote the different junctions, with $E_{G1} < E_{G2}$. Here we made use of the definition that under full concentration $X=1/f_s$, and that the same current follows through both junctions; the term in parenthesis is the current generated by the smaller bandgap junction. The current matching constraint is described by the following:

Equation 1-29

$$N(E_{G1}, E_{G2}, T_S, 0) - N(E_{G1}, E_{G2}, T_a, qV_1) =$$

$$N(E_{G2}, \infty, T_S, 0) - N(E_{G2}, \infty, T_a, qV_2)$$

, where the terms to the right hand side of the equal sign is the current generated by the larger bandgap junction.

Two and three junction solar cells are commercial technology. Triple junction solar cells are the highest efficiency commercial cells available. However, due to the complexity of the device structure, they are currently prohibitively expensive for large scale deployment.

One of the challenges of the multijunction solar cell technology is the complexity of the device structure used to engineer three junctions in series. The intermediate band solar cell (IBSC) concept aims to achieve similar improvements to multijunction cells, but with only one junction, which should reduce device complexity and achieve cost reduction. Since IBSC is a major topic of this thesis, it will be reviewed in detail in a subsequent section. This section briefly describes the efficiency limit of the IBSCs.

IBSCs are single junction cells that have a sub-bandgap band that allows for sub-bandgap absorption, as shown in Figure 1.20. Here, the E_G denotes the semiconductor bandgap, and E_{G1} and E_{G2} are sub-bandgaps, where $E_{G1} < E_{G2}$. This allows for a larger bandgap, which reduces thermalization losses, while the sub-bandgap absorption simultaneously reduces the transmission losses. The IBSC relies of there being three quasi Fermi levels, for the conduction band (CB), valence band (VB), and the intermediate band (IB). As shown in Equation 1-9, this implies that the carrier lifetime in are relatively long lived compared to thermalization and carrier extraction. While similar to a triple junction cell discussed in the previous section, IBSCs would have a higher expected efficiency limit because for above bandgap photons they achieve better quantum efficiency. For triple junction cells, three photons are needed to generate one electron hole pair; for IBSC, only one above bandgap photon is needed to generate one electron hole pair.

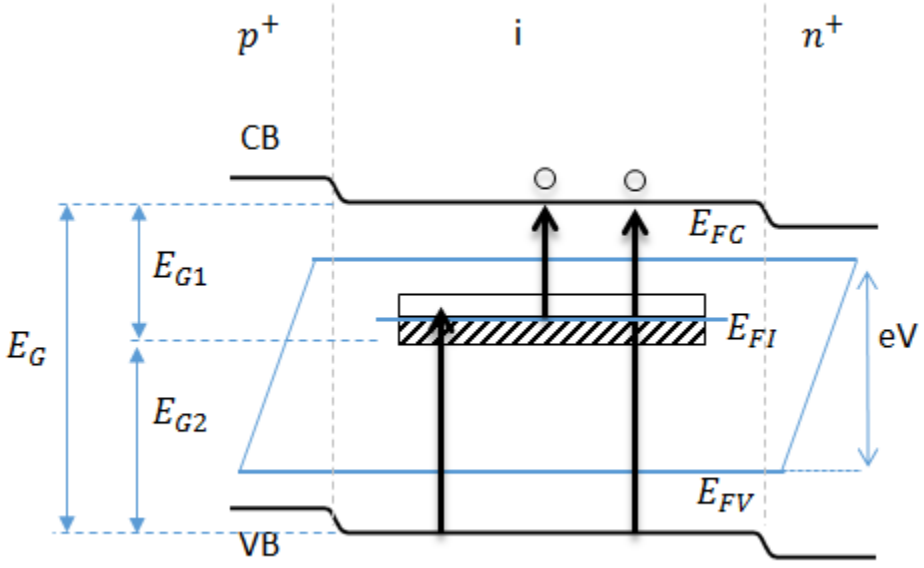

Figure 1.20 Band diagram of an Intermediate Band Solar Cell with a p-i-n device structure, showing separate quasi-Fermi level for the intermediate band.

To calculate the maximum efficiency of IBSCs, we note that there are two sources of current generation: absorption of above bandgap photons and absorption of sub-bandgap photons, as shown in the following equation,

$$J(V) = q\{N(E_G, \infty, T_S, 0) - N(E_G, \infty, T_a, E_{FC} - E_{FV})\} \quad \textbf{Equation 1-30}$$
$$+ q\{N(E_{G2}, E_G, T_S, 0) - N(E_{G2}, E_G, T_a, E_{FI} - E_{FV})\}$$

, where the first term accounts for band to band absorption and radiative recombination, and the second term accounts for the absorption and radiative recombination between the IB and the VB. Similar to triple junction cells, the net current generated by the two sub-bandgaps have to be matched. This constraint is expressed as:

$$q\{N(E_{G1}, E_{G2}, T_S, 0) - N(E_{G1}, E_{G2}, T_a, E_{FC} - E_{FI})\} \quad \textbf{Equation 1-31}$$
$$= q\{N(E_{G2}, E_G, T_S, 0) - N(E_{G2}, E_G, T_a, E_{FI} - E_{FV})\}$$

If the contacts to the external load is only in contact with the quasi-Fermi levels of the CB and VB, the output voltage would be defined by $qV = E_{FC} - E_{FV}$. The theoretical maximum efficiency of IBSC is 63.1 % at full concentration, for $E_G = 1.93\ eV$ and $E_{G1} = 0.7\ eV$[11].

Multijunction and intermediate band solar cells reduce thermalization losses by using larger bandgaps; another way to thermalization losses is to extract the carriers before they thermalize. As shown in Figure 1.21 [12], the electron and hole populations start out being in thermal equilibrium with the Sun immediately after generation. After about 1ns, the carriers are cooled to the ambient temperature by heat transfer to the lattice carried through phonons. The idea of hot carrier solar cells is to slow down that cooling

process so that some of that energy otherwise would be lost as heat can be recovered as electrical potential energy (voltage).

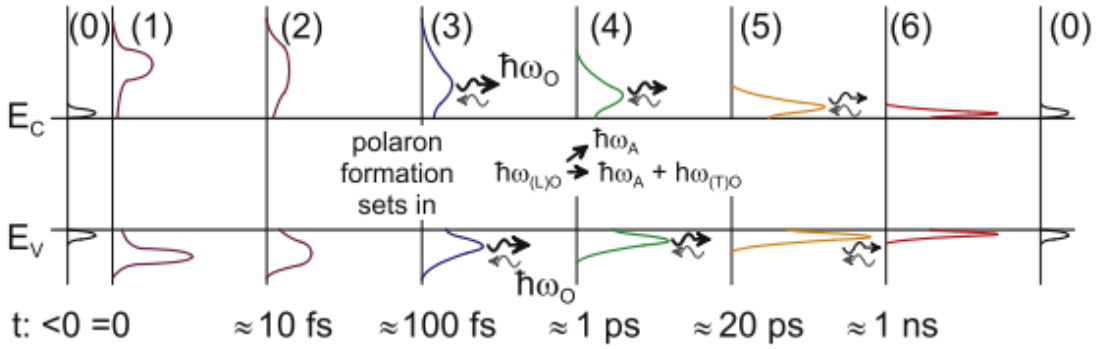

Carrier cooling kinetics in bulk semiconductor: Thermal equilibrium (0); immediately after optical generation (1); carrier–carrier scattering, impact ionisation, re-normalisation of carrier energies, Fermi–Dirac statistics (2); optical phonon emission (re-absorption) (3); decay of optical into acoustic phonons (4); further phonon emission (5), to thermal equilibrium, onset of carrier recombination (6).

Figure 1.21 Evolution in time of the carrier population after initial light generation[12].

In the analysis of hot carrier solar cells, we assume that impact ionization does not happen, so that energetic carriers do not generate other carriers by losing kinetic energy. The maximum efficiency of the solar cell is analyzed as follows. The chemical potential of a carrier, η, is the amount of energy that can potentially be extracted as electrical potential energy (voltage) to the external circuit. After thermalization, where some of this energy is lost to the lattice as heat, and all electrons end up with a lower chemical potential η_e and η_h, respectively. If we assume that thermalization has not yet happened, we expect the carriers to have more chemical potential energy, since carrier-carrier scattering conserves chemical potential and kinetic energy. The chemical potential is then expressed as:

Equation 1-32

$$\eta_i = \eta_o + \gamma E_i$$

, where E_i is the carrier kinetic energy, and "i" specifies the individual carriers. The chemical potential of the electron and hole pair would be the sum of the chemical potential for the electron and hole:

Equation 1-33

$$\Delta\mu = \eta_{eo} + \eta_{ho} + \gamma(E_e + E_h)$$

, where the chemical potential of the electron hole pair $\Delta\mu$ is excitation energy dependent since the carriers kinetic energy is dependent on E - E_G, where E is the photon energy and E_G is the bandgap. This implies that the electron hole pairs can have different chemical potentials, which is different from the case where the carriers have fully thermalized, where the chemical potential is the same for every carrier. As in Equation 1-27, the radiative recombination flux emitted from the semiconductor is expressed as

Equation 1-34

$$N(E_G, \infty, T_a, \Delta\mu(E))$$

As shown in Equation 1-34, $\Delta\mu$ is a function of the photon energy. The integrand in Equation 1-34 can be expressed as quantity that is independent of photon energy, where every electron-hole pair has the same chemical potential μ_H. If we describe the distribution as being at a higher temperature T_H as

Equation 1-35

$$T_H = \frac{T_a}{1-\gamma}$$

, then

Equation 1-36

$$N(E_G,\infty,T_a,\Delta\mu(E)) = N(E_G,\infty,T_H,\mu_H)$$

, so that carrier population is distributed as if they are at a higher temperature T_H than the semiconductor temperature T_a, hence the name "hot carrier" in hot carrier solar cells. In this case, the chemical potential of the electron hole pair $\Delta\mu(E)$ collected at the semiconductor temperature T_a is a function of collection energy E, and μ_H as follows

Equation 1-37

$$\Delta\mu = \mu_H \frac{T_a}{T_H} + E\left(1 - \frac{T_a}{T_H}\right)$$

Because the carriers are not yet thermalized, the device designer can pick an energy E_{out} at which to extract the hot carriers, such that the output chemical potential μ_{out} would be

Equation 1-38

$$\Delta\mu_{out} = \mu_H \frac{T_a}{T_H} + E_{out}\left(1 - \frac{T_a}{T_H}\right)$$

The monochromatic nature of the extraction energy E_{out} is important as it allows for isentropic cooling.

This mathematical system has two unknowns μ_H and T_H that needs two equations to specify. One equation is Equation 1-38, and another is the conservation of energy for the device as shown in the following:

Equation 1-39

$$JE_{out} = q\{Xf_S L(E_G,\infty,T_S,0) + (1 - Xf_S)L(E_G,\infty,T_a,0) - L(E_G,\infty,T_H,\mu_H)\}$$

, where

$$J(V) = q\{Xf_S\, N(E_G, \infty, T_S, 0) + (1 - Xf_S) N(E_G, \infty, T_a, 0) - N(E_G, \infty, T_H, \mu_H)\} \quad \textbf{Equation 1-40}$$

The hot carrier solar cell has a theoretical maximum efficiency of approximately 85 % at full concentration, and 65 % at 1 blackbody sun concentration.

Like hot carrier solar cells, the impact ionization solar cells works with hot carriers. Whereas hot carrier solar cells extract some of the energy from the hot carriers as increased electrical potential energy, impact ionization solar cells use some of the kinetic energy of the hot carriers to generate additional carriers. The equations used to analyze the impact ionization solar cell maximum theoretical efficiency limit is the same as those for the hot carrier solar cells- the primary difference is that $\mu_H = 0$. This is the case for thermal distributions where the particle number is not conserved. One example of this is the photon distributions for the blackbody radiation. Equation 1-39 can be used to find the output current given a designed E_{out} and μ_{out}. For 1 blackbody sun concentration, the theoretical maximum efficiency is approximately 55 % at a bandgap of around 1 eV. At full concentration, the theoretical maximum efficiency is approximately 85 %, for a material with essentially 0 bandgap.

1.11 Intermediate Band Solar Cell Concept

IBSCs are single junction cell with a p-i-n device structure, where in the "i" region incorporates an intermediate band that is electrically isolated from the "p" and "n" contacts, leading to an independent quasi Fermi level for the intermediate level distinct from those for the contacts, as shown in Figure 1.22. The intermediate band reduces the transparency losses by allowing for sub-bandgap absorption. The sub-bandgap absorption shifts the ideal semiconductor bandgap to larger values, which reduces the thermalization losses. The electrical isolation between the intermediate band and the contacts means that the cell can operate at a larger voltage as limited by the now larger bandgap, and the cell would collect more current as a result of sub-bandgap absorption, leading to increased power output and conversion efficiency[11, 13].

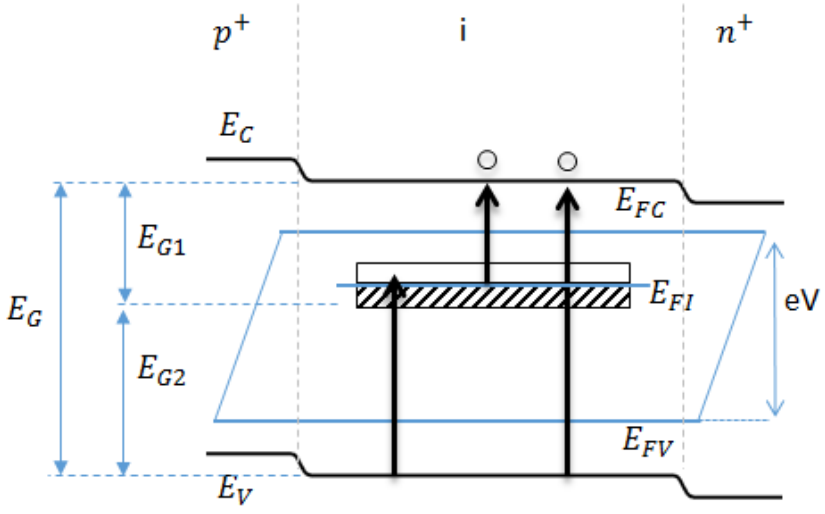

Figure 1.22 Band diagram for an intermediate band solar cell showing the quasi-Fermi levels of the conduction band, valence band, and intermediate band.

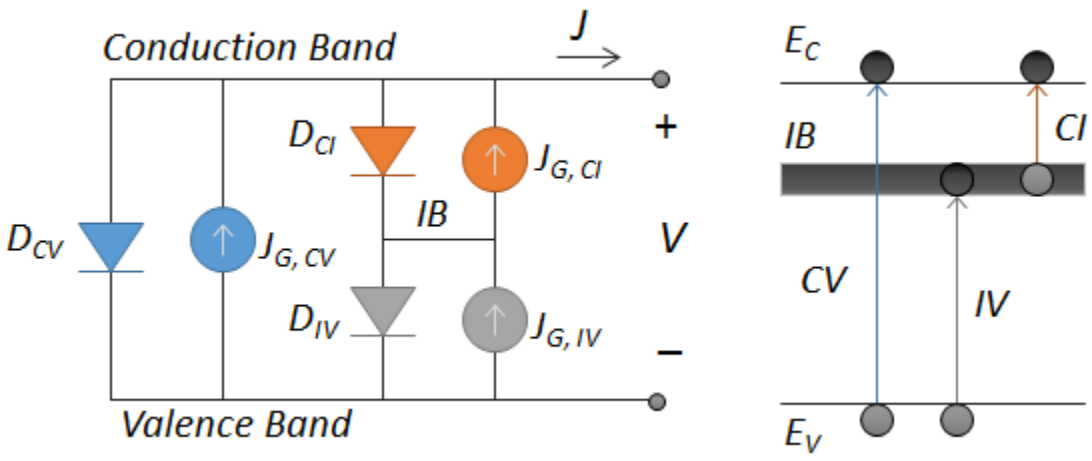

Figure 1.23 Simple circuit model of the intermediate band solar cell. Each of the generation and recombination processes are modeled by a pair of current source and ideal diode. The two sub bandgap generation recombination processes through the intermediate band is modeled by two such pairs in series.

To help understand IBSC parameters such as bandgap and intermediate band (IB) location, we developed a simple circuit model to study IBSC operation. The band to band carrier generation and recombination is modeled by a pair of current source and ideal diode, and the below bandgap two photon to one electron process with two such pairs in series, as shown in Figure 1.23. The modeling result of the efficiency contours with respect the bandgap size and the location of the IB with respect to the conduction band (CB) is shown in Figure 1.24, which indicates that IBSCs have an ideal efficiency of approximately 60 % with a bandgap of near 2 eV and an IB that is approximately 0.8 eV below the conduction band. As Figure 1.24 indicates, IBSC absorbers favor large bandgap materials. Therefore, this work focuses on material properties of wide bandgap II-VI semiconductors and IBSCs made with these materials.

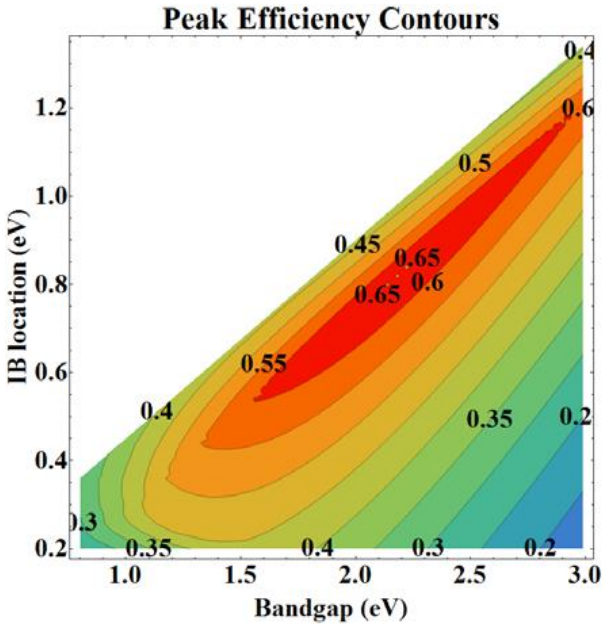

Figure 1.24 Calculated result from the simple circuit model, showing peak efficiency with respect to material bandgap and the location of the intermediate band below the conduction band.

Besides the bandgap and IB depth other ideal IB material properties implied by the circuit model include: non-overlapping absorption bands, no thermal coupling between the IB and CB, and no non-radiative recombination through the IB[13].

To make most efficient use of the solar photons' numbers and energies, it is important that the absorption bands do not overlap. For example, the band to band absorption process generates one electron with one photon, which is more efficient than the sub-bandgap two photon to one electron generation process, as shown in Figure 1.25a. Therefore, above bandgap photons should not be absorbed by sub-bandgap absorption processes. Similarly, the photons that are available to the larger of the two sub-bandgaps should not be absorbed by the smaller of the sub-bandgaps, as this would lead to reduced number of carriers generated, as shown in Figure 1.25b.

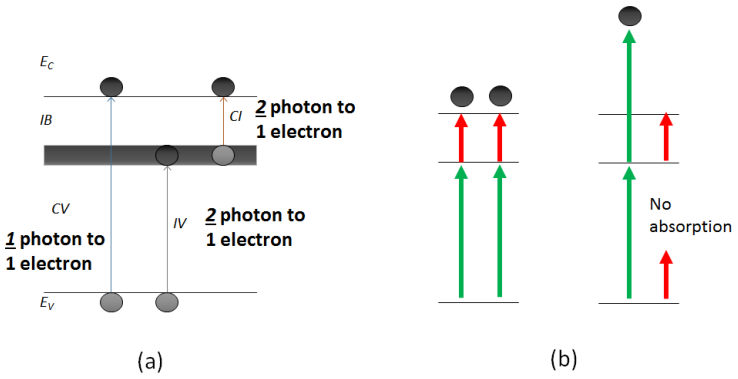

Figure 1.25 Spectral separation of absorption bands requirement: (a) The band to band generation process is more efficient than the sub-bandgap carrier generation process through the intermediate band, since the former uses one photon to generate one carrier electron hole pair, whereas the latter uses two photons. (b) Absorption of high energy photons available to higher energy absorption bands leads to loss in carrier generation.

Non-overlapping absorption band would ideally be achieved by through absorption bands that cutoff where the next largest bandgap begins absorbing as shown in Figure 1.26a, which is the case for triple junction solar cell. This is difficult to achieve in the IBSC case because all the absorption bands exist in the same space, and so a more realistic approach to achieve this may be to make the smaller sub-bandgap weaker than the larger absorption bands to reduce the competition for the high energy photons, as shown in Figure 1.26b. This would imply a thick absorber to ensure full absorption by the smallest absorption band.

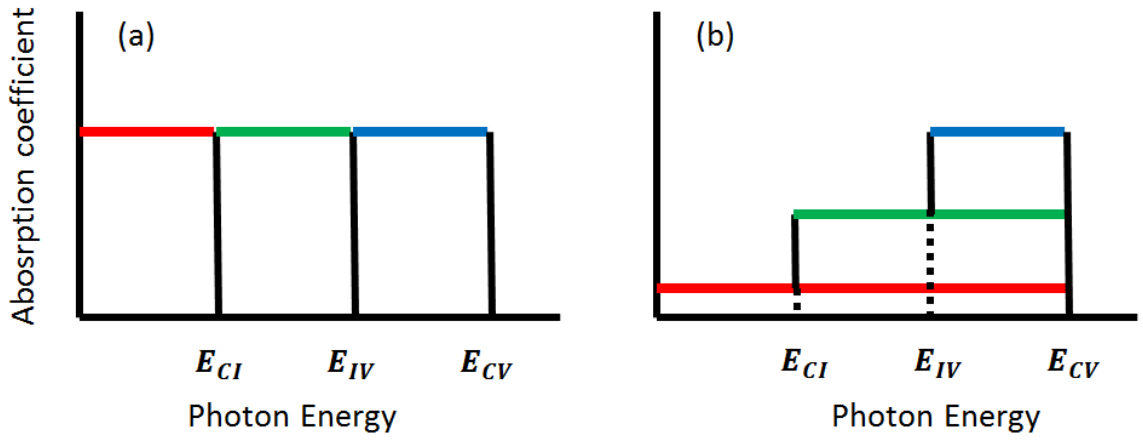

Figure 1.26 Ways to achieve non-overlapping absorption bands: (a) Absorption bands that stops absorbing above the threshold energy of the next higher energy absorption band. No known material behaves this way. (b) The smaller absorption band absorbs less strongly than the larger absorption band.

Assuming full spectral overlap, and the three absorption bands overlaps over 4 eV (essentially fully overlapped), their absorption coefficients are identically at 10^4 cm^{-1}, and that the IB is half filled throughout, Albert Lin and Jamie D. Phillips calculated that the efficiency at full concentration would be reduced to 35.1 %[14]. Besides the case shown in Figure 1.26b, they also proposed to use high low (HL) doping in the IB and spectral decoupling (SD) as practical methods to resolve the overlapping absorption band. In HL, part of the IB is left intentionally unfilled to suppress the CB-IB absorption; in SD, a section of the active region does not have and IB, so that only above bandgap absorption occurs there. They calculated that for the case of HL alone, the solar cell efficiency is raised to 52.8 %, and for the case where both HL and SD are employed, the efficiency is increased to 61.5 %[14], close to the 63.2 % ideal efficiency calculated by detailed balance, that assumes non-overlapping absorption bands.

Besides radiative transitions between IB and CB, electrons can transfer between the IB and CB through absorption and emission and phonons thermally. This can happen

if the IB and CB are within k_BT of each other, so the thermal phonons can promote IB electrons to the CB, and CB electrons can relax to the IB by emitting thermal phonons. Even if the IB and CB is separated by energy significantly larger the k_BT, CB electrons can still relax to the IB by relaxation of multiple phonons if the IB wave functions are sufficiently localized[15]. If this non-radiative relaxation lifetime is much shorter than the time it takes to collect the CB electrons, the IB ad CB is effectively coupled through phonons, thermally. Therefore, it is important that the IB and CB are separated by at least a few multiples of k_BT. As to the problem of suppression of carriers relaxing from the CB to IB through multiple phonon emission, it is not clear if there is a conclusive solution. There is an ongoing debate in the field that will be outlined in the next section.

Thermal coupling between the CB and IB would allow CB electrons to relax to the IB level in the steady state, so that they share the same quasi Fermi level, leading to an effectively reduced bandgap that limits the output voltage. In terms of the circuit model, this would represent an electrical short of the CB and IB level, as shown in Figure 1.27a, leading to a reduced output voltage, as shown in Figure 1.27b.

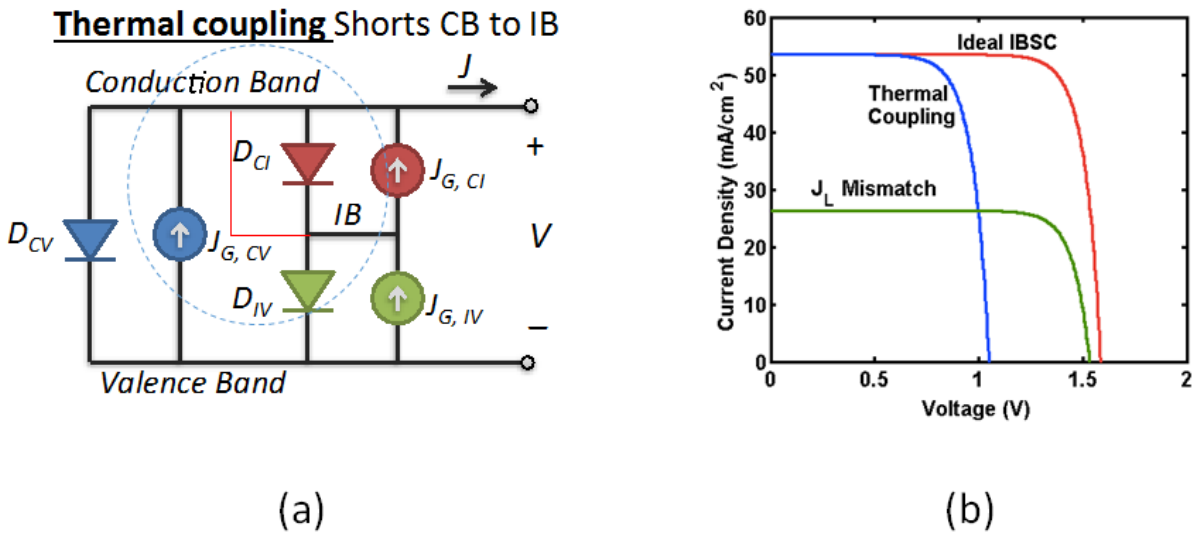

Figure 1.27 (a) thermal coupling between the intermediate band and the conduction band can be modeled as an electrical short. (b) Modeling output showing that such a short reduces the open circuit voltage of the output cell.

Radiative transitions between CB-IB and IB-VB is inevitable, and already accounted for in the detailed balance calculations for the theoretical maximum efficiency. Ideally, non-radiative recombination through the IB should be avoided, since in that case energy that could have been delivered to an external circuit would be lost to the crystal as heat.

There is a current debate in the field on whether or not non-radiative recombination through the IB can be avoided. In one scenario, proposed by Luque and colleagues[15], the non-radiative recombination through the IB can be suppressed by increasing the concentration of the IB producing dopants past the Mott transition, where the IB electronic wave functions become delocalized; In another scenario, proposed by Krich and colleagues[16], IB electronic states would always encourage non-radiative recombination through the IB, regardless of whether the IB wave functions are localized or delocalized. The major difference in the perspectives are briefly described as follows.

Non-radiative recombination through deep states in the semiconductor bandgap is often described by the configuration coordinate picture, as show in Figure 1.28 and Figure 1.29. In this picture, the horizontal axis q is a generic coordinate that describes lattice vibration of a particular mode (the results can be generalizes to all the other phonon modes as well), and the vertical axis plots the total energy of the system (which is assumed to consist of electronic plus vibrational energy). The lattice vibrations are assumed to be harmonic, and so the vibration potential is quadratic, and superimposed on the electronic energy structure (shown as horizontal lines in Figure 1.28, and already included in the solid parabolic looking lines in Figure 1.29). When not filled with an electron, the impurity induced sub-bandgap electronic state would have a parabolic energy centered about $q=0$ in this picture. When the impurity is filled with an electron, the vibration mode is disturbed, such that the equilibrium position on the generalized coordinate about which the mode vibrates is shifted. This shift makes it possible for sub-bandgap energy curve intersect with those of the conduction and valence band. The intersection allows for the electron to transfer from the CB to IB without emitting phonons, since the extra energy is used to support the large vibration amplitude of the mode. Multiple phonons are eventually emitted to reduce the amplitude to the new rest point. The two sides of the debate differ primary in interpreting the cause of the shift in the rest coordinate of the IB vibration mode once it is populated with an electron.

In the model described by [15], the shift if IB vibration coordinate is due to a Coulombic interaction of the populating electron with the charges surrounding the IB inducting impurity. If this is the case, delocalizing the electronic wave function would spread the effect of the charge of the electron in space, and induce less distortion to the

lattice around impurities. This would reduce the shift in the rest vibration position of the impurity atom, and move the intersection point A in Figure 1.28 to a higher energy, which reduces the likelihood of a conduction band electron having enough energy to reach the intersection point. This would suppress non-radiative recombination through the IB.

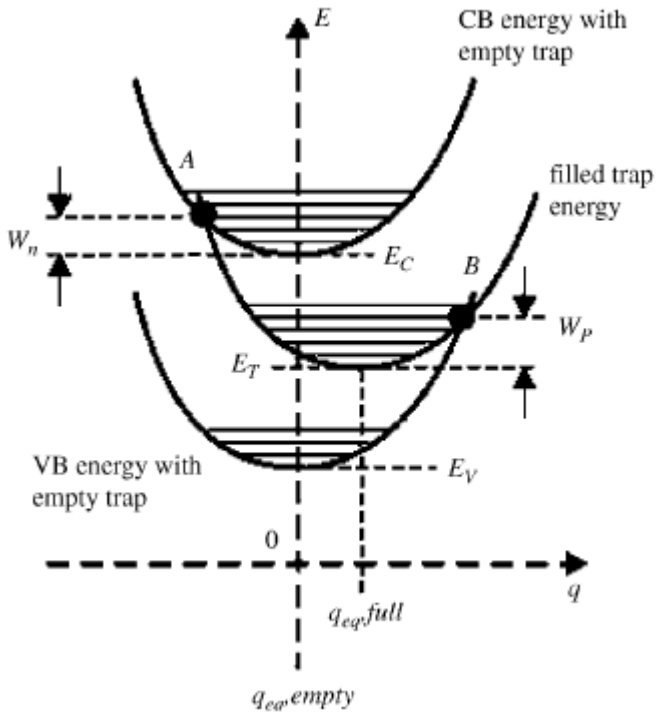

Figure 1.28 Configuration diagram of the viewpoint of [15], which argues that non-radiative recombination through the intermediate band (IB) can be suppressed if the impurities leading to the IB is of high enough concentration.

In the model described by [16], the shift in the equilibrium coordinate about which the impurity populated by an electron is due to electron phonon coupling, instead of the Coulombic interaction described in [15]. The right hand side diagram in Figure 1.29 shows that the linear change in electronic energy due to the electron-phonon interaction that shifts the equilibrium vibration coordinate from $q = 0$ to nearly $q = \delta q$; a small amount of that shift is due to change in the electronic energy λ due to Coulombic

interactions resulting from local crystal distortion around the impurity. Because the majority of the shift from $q = 0$ to $q = \delta q$ is due the electron-phonon interaction, the localized or delocalized nature of the electronic structure would not significantly affect the intersection point between the CB and IB parabolas, which determines the activation energy (E_a in Figure 1.29). While it's possible that the IB electronically energy is perturbed to shift up by many times k_BT, and raising E_a significantly to suppress non-radiative recombination, this is unlikely. The scenario presented by [16] implies that regardless of whether or not the unfilled IB state is delocalized, the electron-phonon interaction will work to localize the electronic charge about the IB inducing impurity.

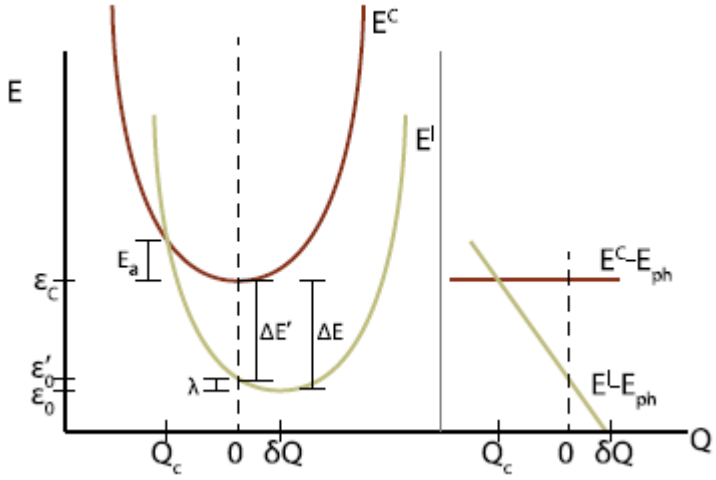

Figure 1.29 Configuration diagram of the view point of [16], which argues that the intermediate band (IB) promotes non-radiative recombination through the IB regardless of the density of the impurities that give rise to the IB.

1.12 Overview of Thesis

The overview of the thesis is shown in Figure 1.30.

Chapter 1: Description of the fundamentals of solar cell operation, the historical developments in photovoltaic technology, and the proposed next generation solar cells for

high efficiency. Detailed discussion of the Intermediate Band Solar Cell (IBSC) concept: what are the material properties required for successful IBSC operation, and current debate in the field on whether IBSC without non-radiative recombination through the IB is possible.

Chapter 2: Discussion of II-VI film on III-V substrate growth by Molecular Beam Epitaxy, with data on growth parameters of ZnSe, ZnSe:Cl, ZnSe:N, ZnTe, and ZnTe:O. Also presents a novel technique to prepare GaSb(100) substrate directly in a II-VI chamber for near lattice matched ZnTe/GaSb(100) epitaxy.

Chapter 3: Structural, chemical, and optical data on ZnTe:O, showing that oxygen location in the crystal structure influences electronic structure, and that the oxygen location in the material may be determined by Nuclear Reaction Analysis Channeling.

Chapter 4: Two-pump time resolved photoluminescence data showing time resolved electron transfer from the intermediate band (IB) to conduction band (CB) in ZnTeO. Also reveals that the CB electron lifetime is in the picosecond time scale.

Chapter 5: Device data of IBSC based on ZnTe:O. External quantum efficiency (EQE) data shows sub-bandgap response for a devices with ZnTeO absorber, but not for one with ZnTe absorber. Similarly, I-V data shows photocurrent response from sub-bandgap red laser illumination for a device with ZnTeO absorber, but not for one with ZnTe absorber.

Chapter 6: Optical, structural, and chemical data for oxygen doped II-VI ternary alloys, showing oxygen induced red shift in photoluminescence for ZnSeTeO and CdZnTeO.

Chapter 7: Conclusions and suggestions for future work.

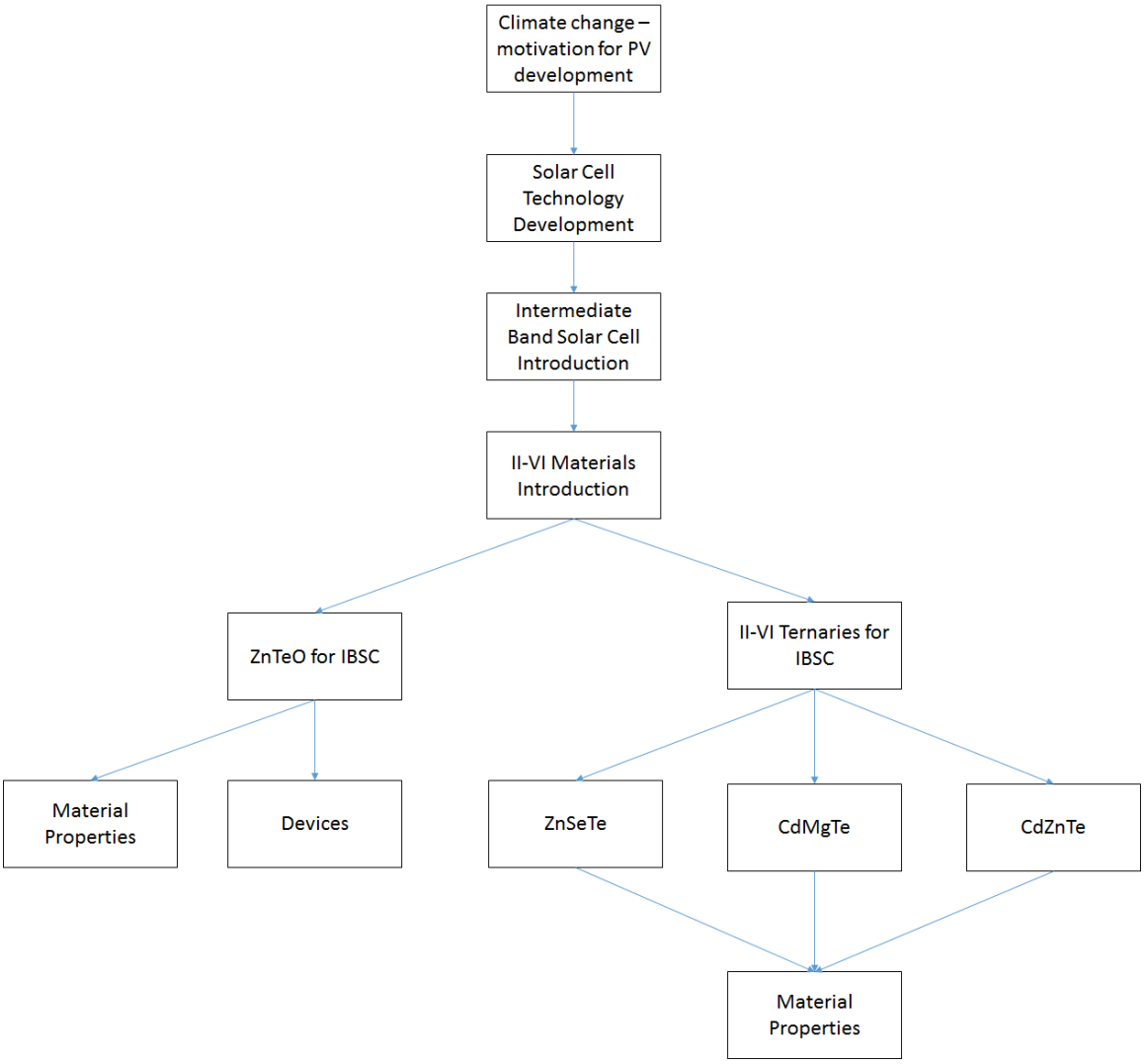

Figure 1.30 Outline of this thesis.

Chapter 2
Growth of II-VI Materials

2.1 II-VI semiconductors

II-VI semiconductors have bandgap energies ranging from infrared to ultraviolet, as shown in Figure 2.1, making them potentially useful for optoelectronic devices ranging from IR detectors to UV lasers. As several II-VI semiconductors have large bandgap, II-VI materials had received some attention for developing green and blue-green light emitting diodes (LED) and laser diodes (LD). However, significant challenges remain for devices that require high current injection, such as LEDs and LDs. For example in II-VI LDs, the device lifetime was very short at approximately 100 hours, despite advances of reducing stacking fault density to $3x10^3$ cm^{-2} for II-VI material grown on III-V substrates[17]. Similarly, II-VI LEDs grown on III-V substrates have lifetimes of approximately 300 hours despite having low stacking fault density to $3x10^3$ cm^{-2}[18]. Studies have suggested that the short device lifetimes may be related to the generation and propagation of point and extended defects in the II-VI material under higher current conditions[18], and this remains to date the major challenge towards commercialization of II-VI LED and LDs.

II-VI materials have found much more success with optoelectronic devices that operate at relatively lower current densities, namely IR detectors and solar cells with

operating current densities in the milliamp/cm^2 range (as opposed to the kiloamp/cm^2 range common in Laser diodes and LEDs), and this is the main reason this thesis work studies novel photovoltaic II-VI materials. For example, HgCdTe (MCT) materials prepared by liquid phase epitaxy (LPE) and MBE is a production technology that makes state of the art near IR and long wave IR detectors[19]. In another example, CdTe is a good solar cell material since the bandgap energy of 1.44 eV is a good match to the solar spectrum, and it can be doped both n-type and p-type[8]. Polycrystalline CdTe solar cells are currently a major solar cell production technology.

The main application focus of this thesis work is intermediate band solar cells (IBSC), which are predicted to work best for bandgap energies near 2 eV, as shown in Figure 1.24. We focus on II-VI materials for this work because of many II-VI semiconductors have large bandgaps, and several II-VI ternary alloys allow for bandgap engineering near 2 eV, which may be useful for device optimization of IBSCs. In particular, we focus on studying ZnSe, ZnTe, ZnSeTe, CdZnTe, CdMgTe materials in this work.

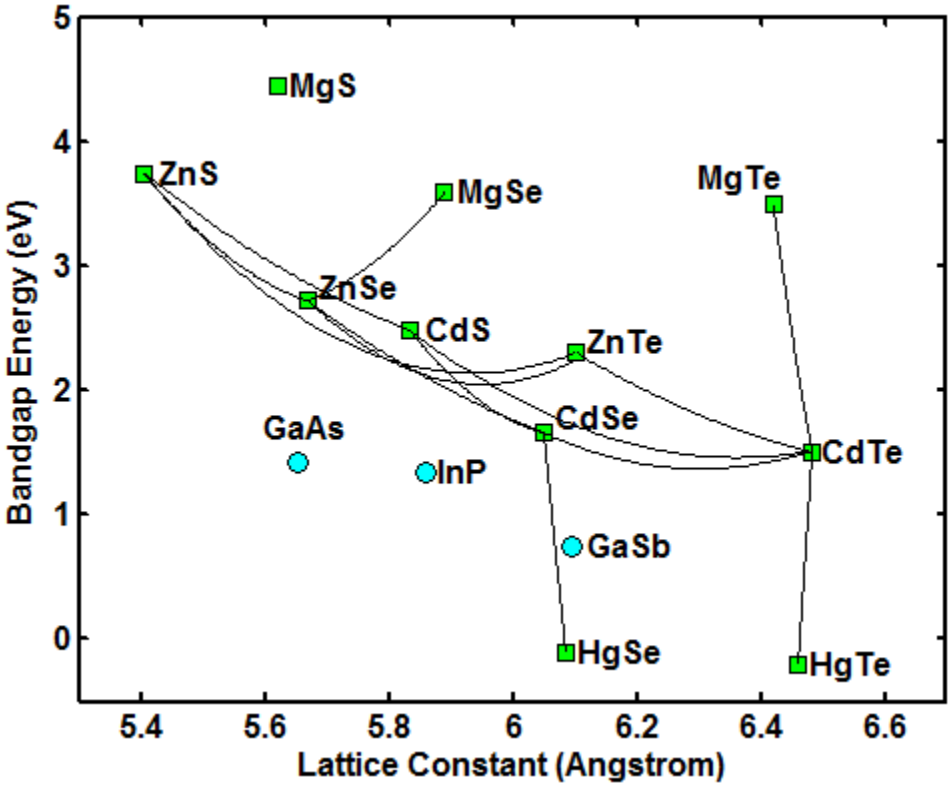

Figure 2.1 Band gap energy versus lattice parameter diagram for II-VI materials.

2.2 Molecular Beam Epitaxy of II-VI materials

Group II-VI compound semiconductors may be effectively synthesized by molecular beam epitaxy (MBE). The MBE technique provides atomic layer control over crystalline growth by exposing a heated crystalline substrate in ultra-high vacuum to beams of elemental atoms or molecules. The high purity 99.9999 %+ source material and the ultra-high vacuum environment (10^{-10} Torr base pressure) provides a clean environment for epitaxy. Solid source beams for Zn, Te, Se, CdTe, Mg, $ZnCl_2$ are generated by solid source effusion cells and an Electron Cyclotron Plasma (ECR) plasma source provides N and O molecular plasma. Since the mean free path of the source beams (~ km) are much larger than the chamber dimensions (~ m) in the vacuum conditions

typical of MBE chambers, the source beam atoms or molecules do not interact with other atoms or molecules from the source or those desorbed from growth surface, and the crystal growth process is kinetically controlled[20]. The surface reconstruction of the growth surface is monitored in-situ with Reflection High Energy Electron Diffraction (RHEED) tool mounted at grazing angle with respect to the growth surface.

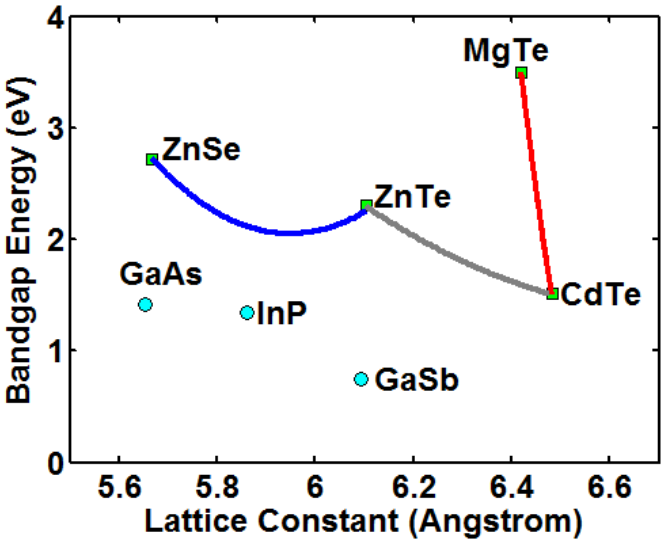

Figure 2.2 Bandgap versus lattice constant plot of the ZnSeTe and CdMgTe alloy systems, as well as some common III-V commercial substrates that are candidates for synthesizing these thin film alloy systems.

Lattice mismatch between the epitaxial film and substrate generates dislocations that degrade the optical and electrical properties of the film. The typical semiconductors grown in our chamber ZnSe, ZnTe, and CdTe and common substrates of GaAs, GaSb, and InP are plotted on a bandgap vs lattice constant plot in Figure 2.2. As shown, GaSb is near lattice matched to our material of interest ZnTe(O), and so we developed lattice matched growth of ZnTe on GaSb. The misfit between ZnTe and GaSb if 0.12%. Based on the XRD data and calculations presented in[21] misfit of ZnTeO and ZnTe is in the

range of 0.1-0.25% for the materials studied in this thesis work. In that calculation, Zinc Blend ZnO lattice constant was used, and Vegard's law was assumed to be valid.

2.3 Growth of ZnSe on GaAs

The growth of ZnSe on GaAs has received significant research attention, and serves a model system to explore common features of II-VI epitaxy on III-V substrates. Most of the discussion of this section is based on [22]. Since II-VI and III-V semiconductors have different number of valence electrons in their covalent bonds, this interface is not charge neutral. This may lead to high electric fields if the number of II-V and III-VI bonds are not equal at the interface. Surface reconstruction and defect generation would occur to relax the high electric fields at the interface. Besides valence mismatch, ZnSe and GaAs are also slightly mismatched in lattice constant (0.26% misfit), which leads to strain and generation of dislocations past a critical thickness. The critical thickness for ZnSe/GaAs grown by MBE has been experimentally measured to be approximately 100 nm[23, 24], which is comparable with the thickness of the ZnSe/GaAs layer we use in our devices. Since ZnSe is the n-type contact layer in our p-i-n device structure, as shown in Figure 5.1c, it is not designed to absorb much light and generate carriers, and so does not need to thick.

In this work, the epi-ready GaAs(100) wafers are loaded into the chamber without a native oxide wet etch. Instead, the native oxide of the GaAs substrate is removed in-situ. The substrate is first heated to 200 ^{o}C and left there for an hour to remove the moisture on the substrate. The temperature is then raised to 500 ^{o}C and held there for 5 minutes; then heated to 550 ^{o}C and held there for 5 minutes; and heated to 600 ^{o}C and held there for 5

minutes. At this point, a streaky reflection high-energy electron diffraction (RHEED) pattern can be observed as is consistent with the known oxide desorption temperature of 580ºC – 600ºC[25]. Our SIMS data shows that for some samples the native oxide desorption is incomplete (see for example Figure 3.7), we typically then heat the substrate to approximately 650 ºC, and held there for approximately a minute, after which the power supply to the substrate heater is turned off, and turned back on when near the growth temperature, which ranges from 250 ºC to 300 ºC. Since we do not have access to the As beam over pressure in our II-VI chamber during this step that is typical for III-V MBEs[26] to compensate for As preferential desorption, the substrate would start roughening if left at 650 ºC for too long (~ 5 min) as confirmed by the evolution of the RHEED pattern from streaks into spots.

In the ZnSe/GaAs system, treatment of the GaAs surface prior to ZnSe growth can affect both the charge state of the surface as well as the 2D vs 3D growth mode of the epitaxy. For growth on GaAs(100) Zn exposure on the (2 x 4) surface prior to ZnSe growth is known to lead to low defect density in the ZnSe film, and Zn treatment of the surface prior to growth on any surface reconstruction promotes the 2D, layer by layer, growth mode[22].

In the work presented in this thesis, the growth of ZnSe/GaAs(100) materials are done with a Zn flux pre-treatment. The cleaned substrate is first exposed to Zn flux with beam equivalent pressure (*BEP*) of approximately 1 x 10^{-6} Torr for 5 seconds before the Se shutter is opened to initiate the growth of the ZnSe epitaxial film. The films are typically grown with Se/Zn *BEP* ratio of 1 - 2, with Zn *BEP = 1 x* 10^{-6} Torr. The substrate temperature T_{sub} is typically 250 ºC to 300 ºC, as measured by a thermocouple

mounted near the back of the substrate. For $T_{sub} = 300\ ^oC$, the growth rate is typically 0.5 – 1 μm/hr, depending on the *Se/Zn* BEP ratio, with *Se/Zn = 1* typically at 0.5 μm/hr and *Se/Zn = 2* at 1 μm/hr. This suggests that the growth rate in growth conditions used in this work is limited by Se flux.

Following the growth the ZnSe films are characterized by X-ray diffraction (XRD) and Nomarski microscopy. Figure 2.3 shows the Nomarski microscope image of a typical ZnSe/GaAs(100) sample, showing some micron scale defects on a background of a generally smooth film. This particular sample is approximately 640 nm in thickness, XRD is typically performed in the (004) reflection, and the full-width-half-max (FWHM) of the ZnSe(004) film peak is typically approximately 300 arc-seconds. Figure 2.4 shows the XRD data in the (004) reflection for a ZnSe/GaAs(100) sample grown with Se/Zn BEP of 2, substrate temperature of 300 ^{o}C, with a thickness of 1.4 μm, shows a XRD ZnSe (004) film peak FWHM of 260 arc-seconds. Since one way the XRD peak can be broadened is by rotations introduced into the crystal lattice by dislocations, the FWHM of the XRD peak is related to the threading dislocation density of the film. The theory of measuring dislocation density of (001) Zinc Blende crystals with XRD has been presented by Ayers[27], and has been applied to the ZnSe/GaAs(100) system by Constantino and co-workers[28]. This technique involves taking XRD data in several crystallographic directions, for film thicknesses that span across the critical thickness for dislocation generation[28]. XRD rocking curve data for (004), (115), (117) reflections should be sufficient to determine dislocation densities for most (001) crystals[27]. The FHWM of the XRD peak exhibits three regions with respect to increasing film thickness[28]: i) thinner than critical thickness, the FWHM decreases with increasing

thickness as crystal size get bigger in the growth direction; ii) past critical thickness, FWHM increases with increasing thickness as threading dislocations are generated; iii) past the point of maximum dislocation density, the FWHM decreases with increasing thickness, as dislocations glide toward each other and coalesce[29]. As such, the FWHM is highly dependent on film thickness in general, and past the critical thickness, larger FWHM is correlated to higher dislocation density.

The influence of growth conditions explored in this work on the crystal quality and surface morphology is discussed in the following.

Within the T_{sub} range of 250 ^{o}C to 300 ^{o}C, the crystal quality appears to be in general better for higher T_{sub}. For example, for *Se/Zn* BEP of 2, a sample grown with $T_{sub} = 250\ ^{o}C$ had XRD ZnSe (004) film peak FWHM of 420 arc-seconds, whereas that for a sample grown with $T_{sub} = 300\ ^{o}C$ was 260 arc-seconds. For our samples, the sample grown with $T_{sub} = 250\ ^{o}C$ had a thickness of 0.6 μm, whereas the sample grown with $T_{sub} = 300\ ^{o}C$ had a thickness of 1.4 μm. Therefore, for undoped ZnSe films, we typically grow at $T_{sub} = 300\ ^{o}C$. At significantly higher growth temperatures the growth rate becomes too slow. We only use lower growth temperatures of $T_{sub} = 250\ ^{o}C$ for doping the material, as explained in the next sub-section. We do note however that the result is likely influenced by the thickness differences in the samples. For example, in the data presented in [28] for ZnSe/GaAs(100), the critical thick was determined to be approximately 0.17 μm, the FHWM for (004) reflection reached a maximum of approximately 500 arc-seconds at approximately 0.5 μm thickness, and the FWHM decreased to approximately 250 arc-seconds at 0.9 μm thickness.

Within the *Se/ Zn* BEP range of 1 – 2, higher *Se/Zn* appears to improve crystal quality. For example at T_{sub} = *300 °C*, a sample grown with *Se/Zn = 1* had a XRD ZnSe(004) film peak FWHM of 300 arc-seconds, whereas that for a sample grown with *Se/Zn = 2* was 250 arc-seconds. For this reason, we typically grown undoped ZnSe/GaAs at T_{sub} = *300 °C*. We note, however, that this result may be influenced by the thickness difference of the two samples. The sample grown with *Se/Zn = 1* had a thickness of 0.94 μm, whereas the sample grown with *Se/Zn = 2* had a thickness of 1.4 μm.

Within the growth conditions considered in this thesis work, T_{sub} range of 250 °C – 300 °C and *Se/Zn* BEP ratio of 1-2, the surface morphology seems to be relatively insensitive to *Se/Zn* BEP ratio, and has better morphology at lower T_{sub} of 250 °C, We do note, however, that more detailed studies surface morphology and growth conditions are needed, since the comparison we made was between a sample grown with T_{sub} = *250 °C*, *Se/Zn = 2*, thickness of 0.64 μm and a sample grown with T_{sub} = *300 °C*, *Se/Zn = 1.5*, thickness of 1.2 μm.

Figure 2.3 Nomarski microscope image of ZnSe/GaAs(100). Sample grown with T_{sub} = 250 ºC, Se/Zn = 2, thickness of 0.64 µm

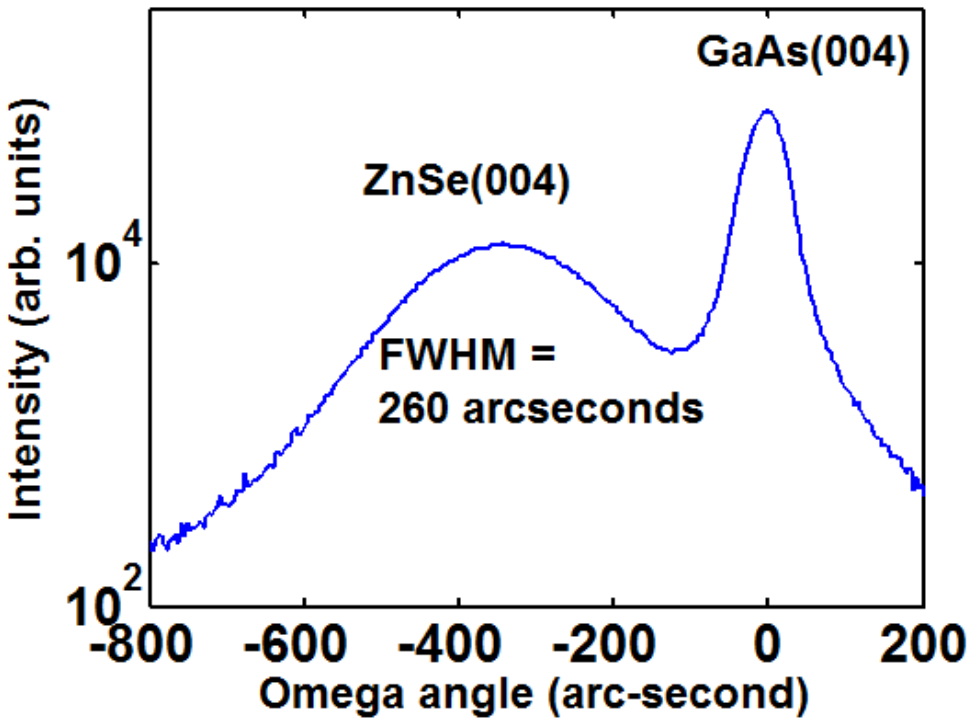

Figure 2.4 XRD data in the (004) reflection of ZnSe/GaAs(100). The sample was grown with T_{sub} = 300 °C, Se/Zn BEP ratio of 2, and film thickness of 1.4 µm.

Most II-VI materials can only be efficiently doped n type or p type, and compensation for the other doping type would be quite high, making it difficult or not possible to dope the material the other type. ZnSe can be easily doped n-type by Ga or Cl (with a $ZnCl_2$ solid source) source to 10^{18} cm^{-3} range electron concentration, up to 3 x 10^{20} cm^{-3} in some reports for $ZnCl_2$[22]. ZnSe can be doped p-type up to 10^{18} cm^{-3} with nitrogen plasma doping, although with high compensation[22, 30] of approximately 60 % activation ratio[30]. Theoretical and/or experimental studies have proposed numerous compensation mechanisms. Some references for various mechanisms listed in [22] include: native defects[31, 32], complex defects[33, 34], impurity-associated defects[35-37], bond breaking[38, 39], and solubility limit[40].

In our chamber, we dope ZnSe lightly p-type with nitrogen using an ECR plasma source to approximately 2 x 10^{17} cm^{-3} hole concentration, with mobility of approximately 10 cm^2/V-s as measured by a room temperature Hall measurement setup with the Van der Pauw geometry and Ni/Au contacts. This mobility is somewhat lower than what has been reported in the literature, and likely means that the growth process can be optimized further. For example, Van der Pauw configuration measurements of room temperature hole mobility of 38.6 cm^2/V-s and has been reported for net hole concentration 3.4 x 10^{17} cm^{-3}[41]; similarly, in a different experiment, a room temperature hole mobility of 34.3 cm^2/V-s for a net hole concentration of 3.4 x 10^{17} cm^{-3} [42]. The *Se/Zn* BEP ratio used for this sample was 2, with *Zn BEP = 0.5 x* 10^{-6} *Torr*. This *Zn BEP* is half of what we typically use for ZnSe, and may have helped with N incorporation. The substrate temperature was 275 ^oC. The nitrogen was introduced with an ECR plasma source, with plasma current of 50mA, and purified N_2 flow rate of 0.2 standard cubic centimeters per minute (sccm) at the inlet of the plasma source. While we have tried otherwise identical growth conditions but higher N_2 flow rates of 0.8 and 1 sccm, the sample was too resistive for the Hall experiment to measure Hall parameters with Indium contact. It is not clear at this point if the high resistivity was due to the Indium contact (as opposed to Ni/Au) or Plasma flow rate. We have fabricated ZnSe p-n homojunctions with this material, where n-ZnSe was produced with $ZnCl_2$ doping source, as described in the following.

We use $ZnCl_2$ solid source for chlorine doping. Since $ZnCl_2$ absorbs a lot of moisture, and the surface of the source material readily turns into liquid form in atmosphere, the freshly charged $ZnCl_2$ source material needs to be extensively baked to

remove the moisture. The temperature for the $ZnCl_2$ source during growth is typically approximately 110 ^oC. Our procedure for the source conditioning after opening the chamber is to first bake the $ZnCl_2$ at 160 ^oC for 1 day, while the chamber itself is baking. After 1 day, we lower the $ZnCl_2$ cell temperature to 110 ^oC for the remainder of the bakeout. After the chamber bakeout is complete, the source continues to bake at 100 ^oC until the background pressure of the chamber falls below in the 10^{-9} Torr range with the source hot. This source conditioning is important for successful synthesis of n-ZnSe, likely because there would otherwise be too much moisture impinging on the growth surface originating from the $ZnCl_2$ cell. This is more complicated than the source conditioning procedure for the other solid sources. The source conditioning for the other sources are as follows: they are first individually brought to 20 ^oC lower than the last recorded growth temperature, held for 6 hours, cooled down. Flux calibration is then performed, and 6 hour long growths of films containing these sources are conducted.

In this thesis work, we were able to dope achieve n-ZnSe net electron concentration n from -8 x 10^{17} cm^{-3} to -8 x 10^{18} cm^{-3}. As expected, higher doping concentration correlates to lower mobility, with a measured mobility of 314 $cm^2/V.s$ for the sample with $n = -8 \times 10^{17}\ cm^{-3}$ and a mobility of 200 $cm^2/V.s$ for the sample with $n = -8 \times 10^{18}\ cm^{-3}$. For our reactor, we noticed that the success of n type doping of ZnSe is highly dependent on substrate temperature. For $T_{sub} = 300\ ^oC$, and *Se/Zn* BEP ratio range from 1 – 1.5 with $Zn = 1 \times 10^{-6}$ Torr, n-type doping could not be achieved for $ZnCl_2$ cell temperature range 90 ^oC – 125 ^oC. Whereas when T_{sub} was reduced 250 ^oC, approximately n = -1 x 10^{18} cm^{-3} concentration was achieved for both *Se/Zn* BEP ratio of 1 and 1.5 for $ZnCl_2$ = 100 ^oC. We noticed that $ZnCl_2$ has the effect of reducing the film

growth rate. For example, for otherwise identical growth conditions, a sample grown with $ZnCl_2 = 100^oC$ yielded a film thickness of 573 nm, whereas sample grown right after it with $ZnCl_2 = 120^oC$ yielded a thickness of 413 nm. Also interesting is that for the sample with grown with $ZnCl_2 = 100\ ^oC$, $n = -1 \times 10^{18}\ cm^{-3}$ was achieved, and when $ZnCl_2$ cell temperature was raised to 120 ^{o}C, the sample became too resistive for Hall parameters to be measured. It is apparent that when the growth surface is exposed to too high a $ZnCl_2$ flux, chlorine is either not well incorporated, or incorporated in a way that is not electrically active. With this information, our procedure to consistently get n-ZnSe is to calibrate the Se/*Zn* BEP ratio to 1.5 with $Zn = 1 \times 10^{-6}\ Torr$, use $T_{sub} = 250\ ^oC$, and vary $ZnCl_2$ cell temperature between the range of 90 ^{o}C – 140 ^{o}C to obtain n-type doping.

Figure 2.5 summarizes the electron concentration *n* in samples where *n* could be measured by our Hall setup. All these samples were growth with $T_{sub} = 250\ ^oC$, and $Se/Zn = 1.5$. Figure 2.5 does not show an obvious correlation between $ZnCl_2$ temperature and *n*. This is likely because the $ZnCl_2$ source material depletes significantly with respect to the MBE growth campaign, such that the flux strength for a given cell temperature depends on the extent of use of the source material in that campaign.

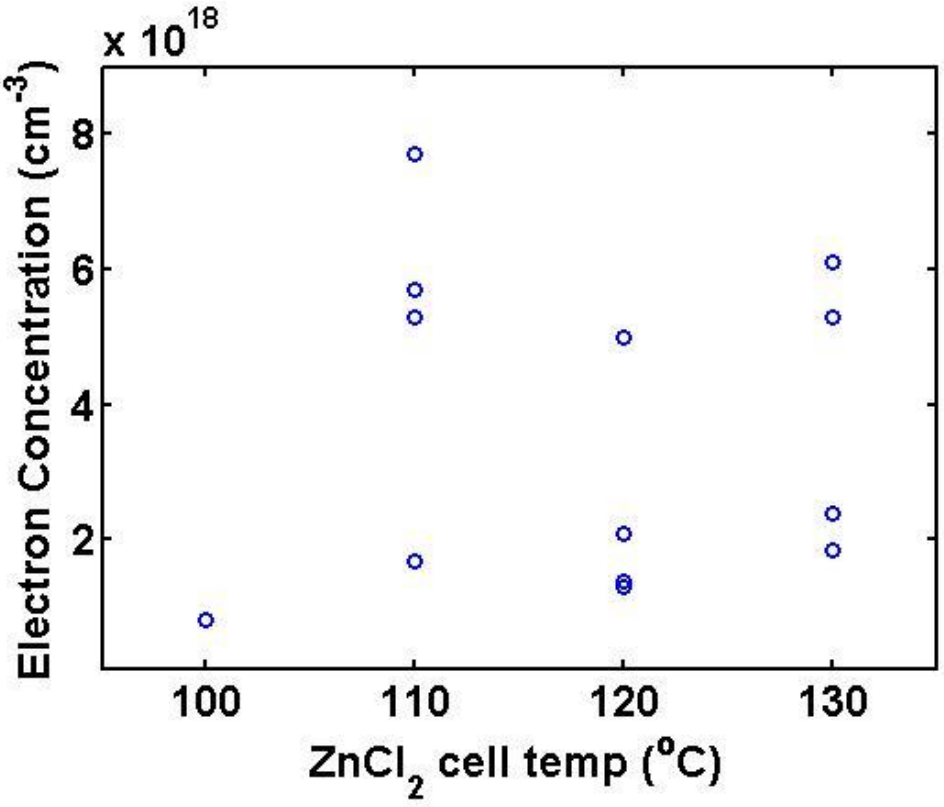

Figure 2.5 Summary of the electron concentration *n* with respect to $ZnCl_2$ cell temperature used during growth in samples where *n* could be measured by our Hall setup. All these samples were growth with T_{sub} = 250 °C, and *Se/Zn = 1.5*.

2.4 Growth of ZnTe on GaAs

Most of the ZnTe films grown for this thesis work were synthesized on GaAs (100). Once loaded into the chamber, the GaAs (100) substrate is heated to high temperatures (approximately 600° C) to remove the surface oxide. This is confirmed by observing a streaky RHEED pattern. Ideally, the oxide desorption step would be done under an As stabilizing flux in an interconnected III-V chamber, since As has a higher vapor pressure, and would preferentially desorb at elevated temperatures. We perform the oxide desorption in the II-VI chamber without an As stabilizing flux, and so the starting

surface is likely As deficient. For similar reasons to ZnSe/GaAs, the surface is exposed to Zn flux before initiating ZnTe growth.

The growth rate is typically around 1 μm/hr. The substrate temperature used for ZnTe/GaAs grown in this thesis work ranged from 300^{o} C – 350^{o} C, Zn flux was kept fixed at 1 x 10^{-6} Torr, which Te flux ranged from 1 x 10^{-6} Torr to 5 x 10^{-6} Torr.

With an ECR plasma source for nitrogen, we can easily dope ZnTe p type from approximately 4 x 10^{17} cm^{-3} to 1.9 x 10^{19} cm^{-3} hole concentration, with mobility from 30 cm^2/V.s for the p = 1.9 x 10^{19} cm^{-3} sample to 50 cm^2/V.s. for the p = 4 x 10^{17} cm^{-3} sample. ZnTe cannot be easily doped n-type. Aluminum has been used to dope ZnTe epitaxial film n-type by MBE[43], and has also been diffused into ZnTe substrate[44, 45] and ZnTe epitaxial films[46, 47] to form an n-type region. We had tried diffusing E-beam deposited Al on p-type ZnTe film grown on p-GaAs substrate, and showed p-n junction rectifying behavior, which implies the formation of an n-type region. We compared the current-voltage data with an identical structure that was not annealed to the case, and confirmed that the contribution of the rectifying behavior of the Shottky junction between Al and ZnTe is significantly weaker than that observed for the p-n junction case.

We characterized the ZnTe/GaAs materials with transmission electron microscope (TEM) and X-ray diffraction (XRD). Since there is a large lattice mismatch of approximately 7 % between ZnTe and GaAs, we expect a highly defective film and substrate interface, as shown by the TEM image in Figure 2.6. The XRD diffraction in the (004) reflection typically shows a film peak with a full width half max of approximately 300 arc-seconds, as shown in Figure 2.7. Since one way the XRD peak can be broadened is by rotations introduced into the crystal lattice by dislocations, the

FWHM of the XRD peak is related to the threading dislocation density of the film. The theory of measuring dislocation density of (001) Zinc Blende crystals with XRD has been presented by Ayers[27], and as described in the previous section, the FWHM is highly dependent on film thickness in general, and past the critical thickness, larger FWHM is correlated to higher dislocation density[28]. Hence, when comparting the FWHM between two ZnTe/GaAs(100) samples with similar thickness larger than the critical thickness, FWHM can be viewed as a relative comparison between dislocation densities. The critical thickness for the ZnTe/GaAs(100) system is approximately 15 nm[48]. Our samples in general has larger FWHM compared to those observed in the literature. For example, a typical sample from this thesis work with thickness 2.7 μm has a (004) XRD peak with FWHM of 245 arc-seconds, where as a sample reported in [48] with thickness 2.5 μm has a (004) XRD peak with FWHM of 45 arc-seconds. One reason our materials are more defective maybe that we did not have an interconnected III-V chamber to desorb the GaAs substrate native oxide under an As protective flux, as was the case for the work presented in [48], so our starting growth surface was more defective.

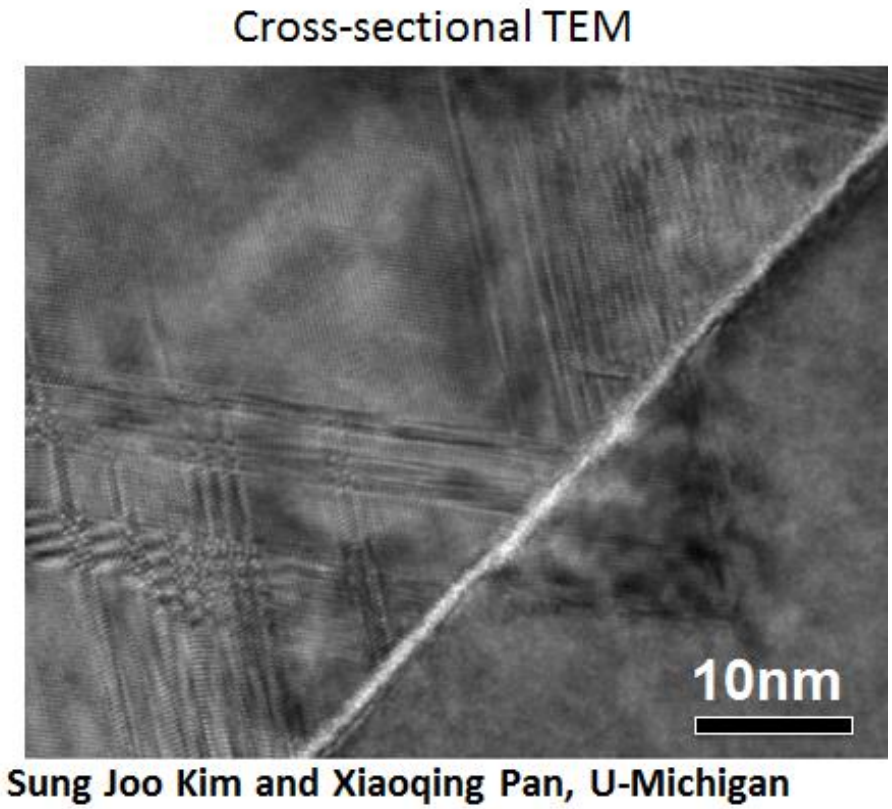

Figure 2.6 Cross sectional TEM showing highly defective interface between ZnTe film (top left) and GaAs substrate (bottom right).

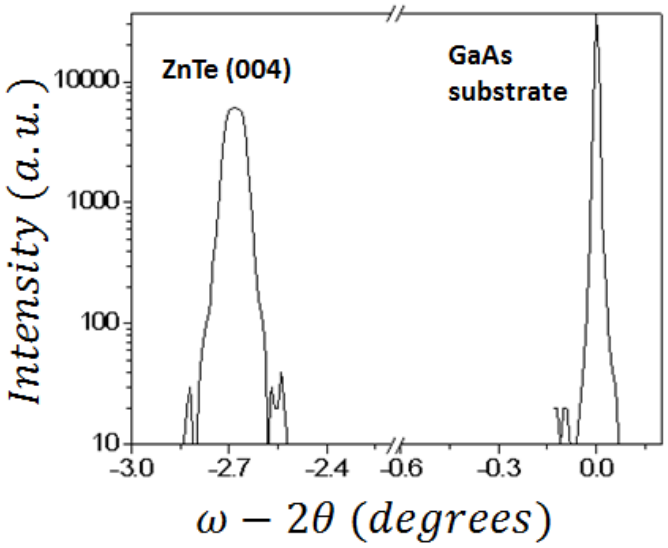

Figure 2.7 Typical XRD data in the (004) reflection for our ZnTe/GaAs(100) materials.

2.5 Latticed Matched Growth of ZnTe on GaSb

Most of our studies of optical properties of ZnTe(O) were done using material on GaAs (100), which has a 7 % lattice constant mismatch to ZnTe. We therefore expect high dislocation densities and a highly defective film to substrate interface, as evidenced by the TEM image shown in Figure 2.6. The ideal substrate to grow ZnTe on would be ZnTe substrate, which would be lattice matched to ZnTe epitaxial layer, and prevent defects related to the II-VI to III-V incompatibility at the film to substrate interface. However, ZnTe substrate technology is not mature, so the commercially available substrates are small area, and cost-prohibitive. Of the more mature commercial substrates, GaSb is near lattice matched to ZnTe, and so we developed ZnTe epitaxial growth on GaSb(100) substrates.

Growth on GaSb substrates by MBE conventionally requires a III-V growth chamber. Prior to epitaxial growth, thermal desorption of Sb_2O_3 and Ga_2O_3 native oxides requires temperatures of 500^o C or above. At these elevated temperatures, the GaSb surface may be degraded due to the preferential desorption of Sb or reaction of remnant Sb_2O_3 with the substrate[49]. Growth by molecular beam epitaxy (MBE) commonly uses an antimony or other group-V flux to stabilize the GaSb surface during this thermal cleaning step[48]. Growth of ZnTe on GaSb using this approach has been successful[48, 50] using a III-V chamber for GaSb surface preparation, followed by the growth of a GaSb buffer layer before transferring to a II-VI chamber for subsequent ZnTe growth. Successful growth of ZnTe directly on GaSb substrates without the requirement for antimony stabilizing flux and GaSb buffer would considerably reduce the complexity of the material synthesis. For example, molecular or atomic hydrogen[51-54] has been used

to deoxidize the GaSb surface without using an antimony overpressure flux, where high-quality ZnTe growth has been demonstrated following surface cleaning of GaSb with atomic hydrogen[52]. An alternative surface preparation technique for growing high quality ZnTe directly on GaSb substrates without a group-V stabilizing flux or any gas sources for surface preparation is presented in this work. The technique includes GaSb substrate etching with concentrated HCl to remove native antimony oxides[49] , followed by thermal oxide desorption in combination with native oxide dissociation via the introduction of $ZnCl_2$ from a standard effusion cell. This technique is convenient for II-VI materials growth, where $ZnCl_2$ is already a common source material used for n-type doping[55-58].

ZnTe was grown on GaSb (100) substrates by molecular beam epitaxy (MBE) using solid source effusion cells for Zn, Te, and $ZnCl_2$. The GaSb substrates were manufactured by Wafer Technology using the LEC growth method. ZnTe epitaxial growth was compared for a) as-received GaSb substrates, b) substrates that were HCl etched prior to loading, and c) substrates that were HCl etched prior to loading and etched in situ using the $ZnCl_2$ effusion source. For experiments where GaSb substrates were etched prior to loading, they were first cleaned with Acetone and 2-Propanol, followed by a 5 minute HCl etch, 2-Propanol rinse, and N2 blow dry prior to loading into the MBE chamber. After loading into the chamber, substrates were first heated to 200 ^{o}C for one hour, and then heated slowly until native oxide desorption was observed by in situ reflection high-energy electron diffraction (RHEED), where a GaSb (1x3) surface reconstruction was observed.

For samples where ZnCl2 flux was used, GaSb substrates were exposed to the $ZnCl_2$ flux (effusion cell temperature 120 ^oC) when the substrate temperature exceeded 200 ^oC, and exposure to $ZnCl_2$ was removed when the substrate was cooled to approximately 380 ^oC following oxide desorption. ZnTe growth was performed at a substrate temperature of 300^o C, beam equivalent pressure (BEP) for Zn and Te at 1.0 x 10^{-6} Torr with the *Te/Zn* BEP ratio of 1 and nominal growth rate of 1 μm/hr. The macroscopic surface morphology was characterized by a laser confocal microscope with Nomarski prism at the Lurie Nanofabrication Facility at the University of Michigan. Atomic scale studies of the interface between the film and the substrate were performed with a high resolution transmission electron microscope (HRTEM) and scanning transmission microscope (STEM) with energy dispersive X-ray spectroscopy (STEM-EDS). The macroscopic crystalline quality was characterized by X-ray diffraction.

ZnTe was first grown on an as-received GaSb substrate. As the substrate temperature was gradually increased to remove the native oxide, a spotty RHEED pattern appeared near a substrate temperature of 500 ^oC, with no distinguishable streaky pattern observed. The spotty RHEED pattern is indicative of a rough surface, attributed to preferential desorption of Sb from the surface at elevated temperatures, and possible reaction of antimony oxides with the GaSb substrate[49, 59]. In select experiments, the substrate temperature was further increased following the observation of a spotty RHEED pattern, to a temperature near 600 ^oC. The spotty RHEED pattern abruptly disappeared upon further heating, likely due to extreme degradation of the GaSb surface.

For samples that were cooled soon after the observation of the spotty RHEED pattern, ZnTe was directly grown on the substrate once the substrate growth temperature of 300 ^{o}C was reached. The rough surface morphology suggested by RHEED was further supported by the resulting ZnTe surface morphology, as shown in the laser confocal microscope image in Figure 2.8(a). A high density of oval defects is observed. Similar oval defects have been observed [60], characterized with AFM as pits[60], and interpreted with RHEED studies[61] to be resulting from Sb desorption from the surface [60]. This interpretation is further supported by Energy dispersive X-ray spectroscopy measurements on the pits from GaSb samples that were removed from the chamber following native oxide desorption and prior to ZnTe growth. In these samples, a reduced concentration of Sb at the center of the pit and an increased Ga concentration are observed, as shown in Figure 2.9.

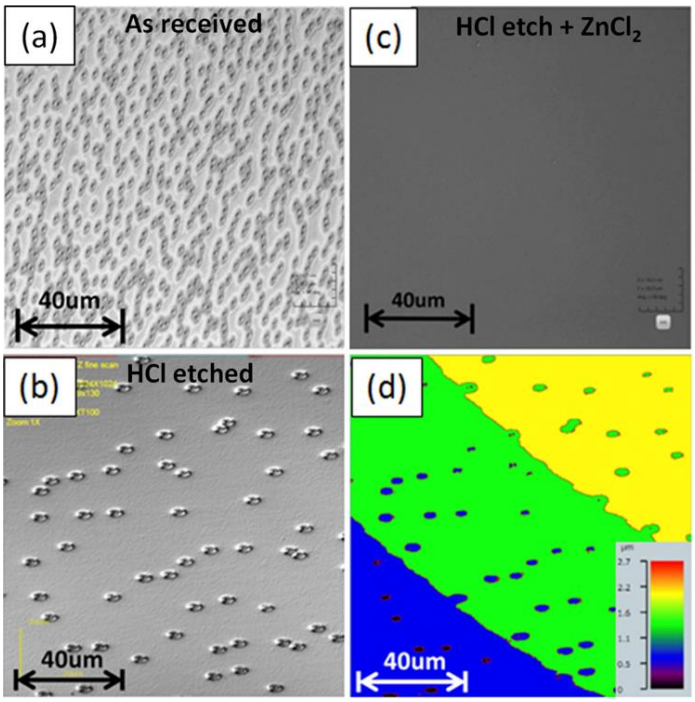

Figure 2.8 Nomarski micrograph for ZnTe/GaAs grown with (a) as received substrate, (b) substrate etched in HCl prior to loading, and (c) substrate etched in HCl prior to loading and etched with $ZnCl_2$ during the thermal clean step. (d) is a height contour plot of (b), showing the oval defects to be pits.

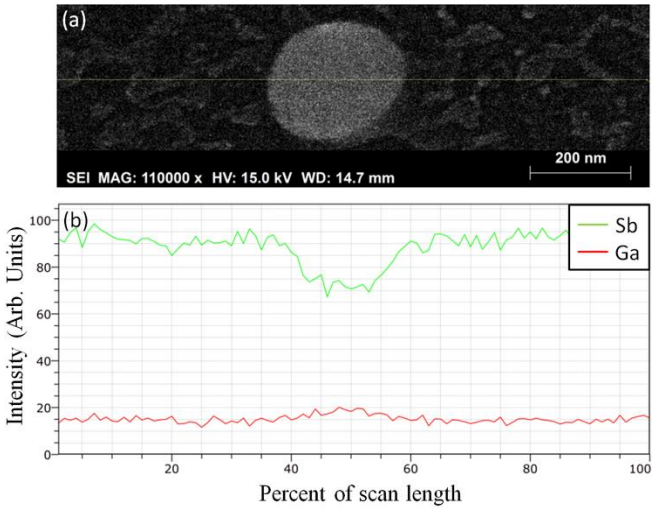

Figure 2.9 (a) SEM image of a region containing an oval defect on an as-received wafer that was heated under vacuum until the appearance of a spotty RHEED pattern. The line across the SEM image illustrates the region of the EDX line scan (b). Sb depletion is significant near the center of the oval defect.

Substrates that were etched with HCl prior to loading exhibited significantly improved native oxide desorption and surface morphology. A streaky RHEED pattern emerged near a substrate temperature of 490 ^{o}C, indicating a smooth crystalline surface. The resulting ZnTe surface morphology is dramatically improved, as shown in the laser confocal microscope image in Figure 2.8(b). However, a significant density of oval defects, which Figure 2.8(d) reveals to be pits, is still observed, and likely too high to serve as useful material for optoelectronic devices. The improvement observed with HCl preparation is consistent with prior reports[49, 62, 63], and is attributed to a reduced native Sb_2O_3 thickness and subsequent roughening of the GaSb surface due to reaction of the oxide with GaSb to form Ga_2O_3 and Sb. To reduce the substrate temperature required to desorb the native Sb_2O_3 and Ga_2O_3 oxides, a $ZnCl_2$ flux is introduced. The $ZnCl_2$ exposure during the thermal clean step resulted in a significant reduction in the temperature required for native oxide desorption, as evidenced by a streaky RHEED

pattern observed near a substrate temperature of 440 ºC. A smooth macroscopic surface that is free of oval defects is observed when using the $ZnCl_2$ exposure, as shown in the Nomarski image of Figure 2.8(c). The microstructure of the ZnTe/GaSb interface observed by HRTEM and STEM (Figure 2.10) reveals an interface with an epitaxial relationship between ZnTe and GaSb substrate for the case of $ZnCl_2$ treatment. STEM-EDS (Figure 2.11) further shows an abrupt interface without significant interdiffusion. The x-ray diffraction characteristics of the ZnTe epitaxial layers grown on GaSb with the $ZnCl_2$ surface clean also demonstrate improved characteristics, as shown in the ω-2θ rocking curves of Figure. The ZnTe (004) and GaSb (004) reflections are observed for all sample treatments, with a significant reduction in the ZnTe peak full width at half maximum from 210 arcsec to 40 arcsec The thicknesses of the films in Figure 2.12a, b, and c are about 580 nm, 1000 nm, and 700 nm respectively, as determined by optical reflectance.

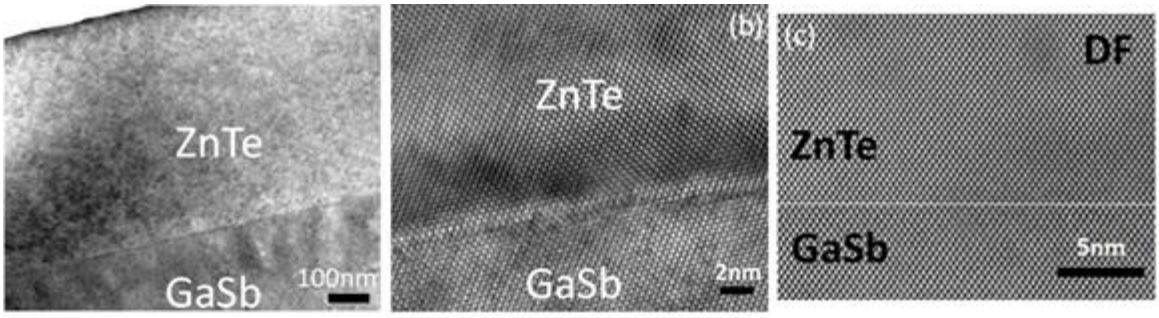

Figure 2.10 (a) low magnification and (b) high magnification HRTEM micrograph of ZnTe/GaSb showing an abrupt interface between ZnTe and GaSb substrate (c) HR-STEM data of the ZnTe/GaSb interface.

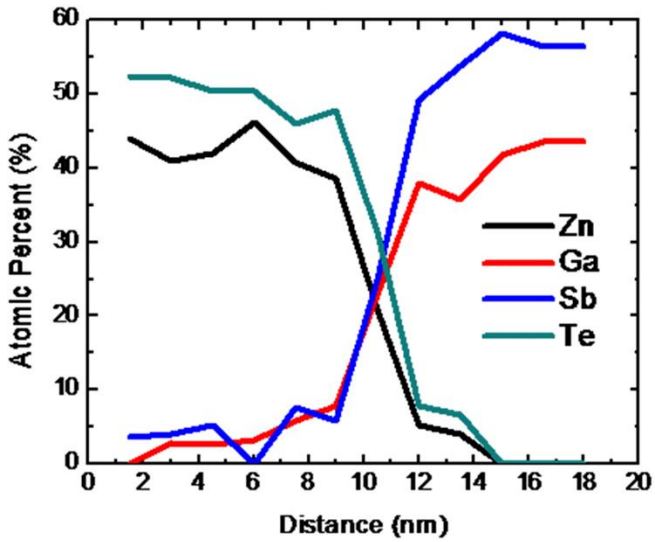

Figure 2.11 STEM-EDS line-scan data across the ZnTe/GaSb interface.

We interpret these observations as follows. HCl etch and 2-Propanol rinse has been previously reported to reduce the GaSb native oxide thickness and resulting in a surface that is Sb rich[63]. After loading into vacuum and thermal desorption of residual surface oxide begins, antimony oxides desorb at relatively low temperatures (near 350 ^{o}C), whereas gallium oxides desorb at higher substrate temperatures (above 500 ^{o}C)[64]. At elevated temperatures without sufficient Sb over pressure, Sb desorbs and results in Sb deficient pits[60] that serve as centers for formation of oval defect pits. When introducing $ZnCl_2$, the chlorine component etches the gallium oxides, leading to lower substrate temperature required for gallium oxide desorption. The formation of volatile GaClx compounds[65-67] is well documented in literature for GaAs substrate etching with Cl containing compounds. Sb preferential desorption is less likely to occur at lower substrate temperatures, leading to reduced oval defects in the grown films.

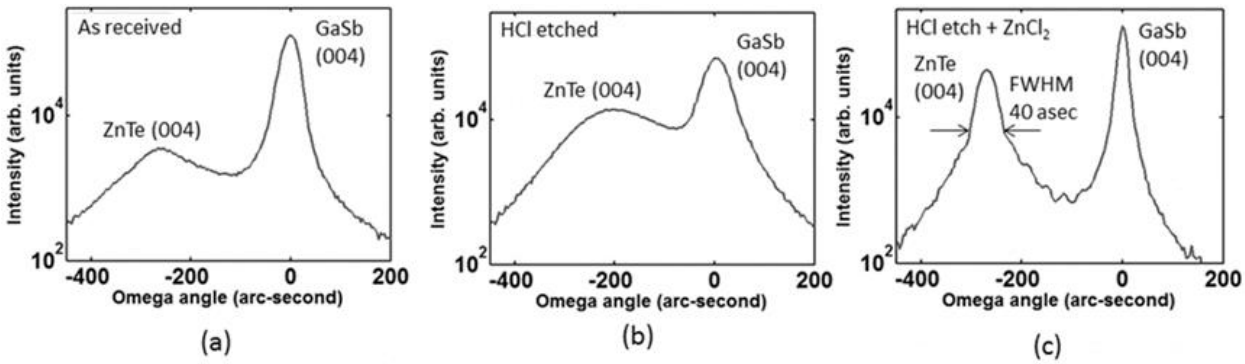

Figure 2.12 X-ray diffraction ω-2Θ data for ZnTe/GaAs grown with (a) as received substrate, (b) substrate etched in HCl prior to loading, and (c) substrate etched in HCl prior to loading and etched with $ZnCl_2$ during the thermal clean step.

A technique for growing high-quality ZnTe on GaSb (100) by molecular beam epitaxy without a group-V flux to stabilize the surface has been presented. The combination of an HCl substrate etch prior to substrate loading and the introduction of a $ZnCl_2$ flux during thermal oxide desorption are used to reduce the temperature required to obtain a surface reconstruction suitable for epitaxial growth and free from oval defects. Subsequent growth of ZnTe using this procedure results in a specular surface, ZnTe/GaSb interface with epitaxial relationship and without significant interdiffusion, and good ZnTe structural properties. This procedure has been repeated in the authors' lab 16 times, and provides a path to achieve ZnTe/GaSb epitaxial layers for device applications without the requirement of an interconnected vacuum chamber dedicated to III-V materials.

While the II-VI materials grown on III-V substrates presented in this Chapter contained significant defect density and were not ideal for high performance device applications, they were perhaps of adequate equality to study fundamental properties of

novel materials and photovoltaic concepts such as highly mismatched alloys and intermediated band solar cells, as presented in later Chapters.

Chapter 3
ZnTeO for IBSC

3.1 Highly Mismatched Alloys

Highly mismatched alloys (HMA) are compound semiconductors with isoelectric dopants that are much more or much less electronegative compared to the host atoms. HMAs have interesting properties such as large bandgap bowing with dilute alloying. For example, 1 % nitrogen alloying into GaAs leads to approximately 15 % reduction in band gap of GaAs[68]. The small dopant atom is much more electronegative than the host it replaced, and so would attract delocalized electrons of any energy, changing the potential energy experienced by the conduction band electrons in the crystal. The Band Anticrossing (BAC) model models this effect by a first order perturbation theory where the dopant energy level E_L was said to identically perturb the energy level of all the conduction band extended states E(k) characterized by the momentum vector, and the perturbation energy is modeled as an off diagonal matrix element $V_{ML}=C_{ML}\,x$, where C_{ML} is an empirical coupling constant, and x is dopant alloy composition. Solving the eigenvalue problem for the perturbed Hamiltonian

$$\begin{bmatrix} E(k)-E_M(k) & V_{ML} \\ V_{ML} & E(k)-E_L \end{bmatrix} = 0 \qquad \textbf{Equation 3-1}$$

, leading to the two band anticrossing solutions

$$E_{\pm}(k) = \frac{1}{2}\left(E_L + E_M(k) \pm \sqrt{\left(E_L - E_M(k)\right)^2 + 4V_{ML}^2} \right)$$

Equation 3-2

, which represent the original conduction band being restructured into two sub-bands $E_+(k)$ and $E_-(k)$ [69]. By modeling the coupling parameter V_{ML} as alloy concentration (x) dependent, the BAC model is able to account for the large bandgap bowing with small increase in x, treating E_- band as the new conduction band, since the E_- band decreases in energy with increasing x. The band anticrossing model is illustrated in Figure 3.1. Figure 3.1a illustrates the original conduction band and valence band Energy-Momentum dispersion curves, as well as the local energy level modeled as a flat line dispersion curve to represent the large spread in momentum space. Figure 3.1b shows the restructured conduction sub-bands $E_+(k)$ and $E_-(k)$ as a result of band anticrossing interactions between the original conduction band and the localized dopant level.

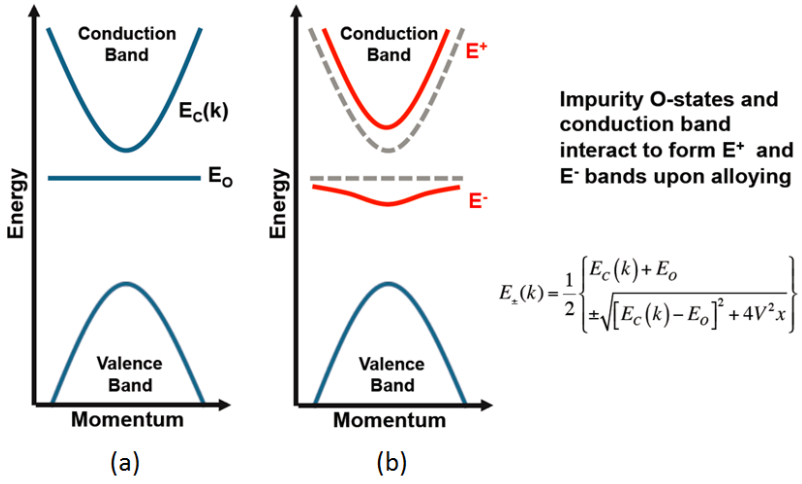

Figure 3.1 Energy-Momentum (E-K) diagram Formation of the intermediate band through band anticrossing effects between the local dopant level and the extended conduction band states. (a) E-K diagram showing the

parabolic conduction band, valence band, and local state. (b) E-K diagram of the restructured conduction band into E^+ and E^- sub-bands shown in red.

IBSCs favor large bandgap semiconductor, as shown in Figure 1.6, we therefore studied a II-VI large bandgap semiconductor ZnTe (E_G=*2.3 eV*) for applications in IBSC. When alloyed with oxygen, ZnTeO is an HMA due to the large mismatch in electronegativity between Te and *O*. The E_- band in HMAs have been proposed to be used as an intermediate band (IB) in Intermediate Band Solar Cells (IBSC)[70].

ZnTeO is predicted to form a narrow energy band (E_- band) below the conduction band minimum upon dilute oxygen incorporation in ZnTe[71, 72], and has been proposed for use in IBSCs[72, 73]. ZnTe has a room temperature bandgap of 2.3 eV, and O introduces a localized electronic state approximately 0.4 eV beneath the conduction band (CB). According to Figure 1.6, the ideal IB location is approximately 0.8 eV below the CB. According to the BAC model in Equation 3-2, one way to make the IB deeper is to increase the oxygen concentration.

Another way to tune the IB location may be through engineering the oxygen clustering configuration, a factor not taken into account by the BAC model. For example, clustering and non-substitutional doping location of nitrogen[74] has been studied in the GaAs:N HMA system. For that system, is has been shown that rapid thermal annealing can reduce the interstitial N while preserving the total N concentration, and this reduction in interstitial N increases carrier concentration and carrier mobility in n-type doped samples[75]. This implies N in interstitial position traps electrons and scatters carriers in transport. The changes to electronic structure as result of N in interstitial versus substitutional position has been experimentally studied by persistent photoconductivity

(PCC)[76]. PCC, which implies a change in the impurity induced level by light towards the conduction band minimum, was correlated with the fraction of N in interstitial doping sites in that work. This may imply a way to engineer the electronic structure of isoelectronic dopant induced energy levels in HMAs: by controlling the dopant location and clustering configuration in the crystal lattice.

The BAC model described the coupling between dopant atoms and extended electronic states with only one parameter, which can account for only one dopant configuration, likely the configuration where the dopant is isolation and do not interact with other dopants. There are some density function theory (DFT) calculations in the literature for the ZnTeO system that allows for oxygen clustering, where oxygen atoms are close enough to each other to interact[77, 78]. These DFT calculations show that oxygen clustering configuration strongly influences electronic structure, and in some cases makes the IB level deeper[77]. Also shown in one calculation is that clustering leads to more delocalized IB electronic wave functions, which may suppress the IB non-radiative recombination through the IB[78].

3.2 Material Synthesis

ZnTe and ZnTeO films were grown on GaAs (100) substrates by molecular beam epitaxy (MBE), with solid sources for Zn and Te, and an electron cyclotron resonance (ECR) plasma source for oxygen. The substrate temperature (T_{sub}) during growth ranged between 300 ^{o}C and 350 ^{o}C. The nominal beam equivalent pressure (*BEP*) for the Zn and Te flux was measured with an ion gauge, with Zn *BEP* at 10^{-6} Torr and *Te/Zn* flux ratio in the range from 1 to 5. A mass flow controller and leak valve were used to control the

oxygen partial pressure in the range from 10^{-7} Torr to 10^{-5} Torr. Post growth rapid thermal annealing (RTA) was performed on select samples in an N_2 environment.

3.3 Chemical Properties

Surface oxide was found on both ZnTe and ZnTe:O films, as shown by the TeO_2 X-ray photoelectron spectroscopy (XPS) signal shown in Figure 3.2. The XPS tool is equipped with sputtering capabilities to remove the surface layer, so that when the bulk material is reached, the TeO_2 XPS signal is absent. This also rules out the TeO_2 bond configurations in the bulk of the samples intentionally doped with oxygen. In the bulk of the samples, oxygen incorporation for the ZnTe:O samples is confirmed with the observation of O 1s XPS signals, which are not detected in ZnTe samples, as shown in Figure 3.3.

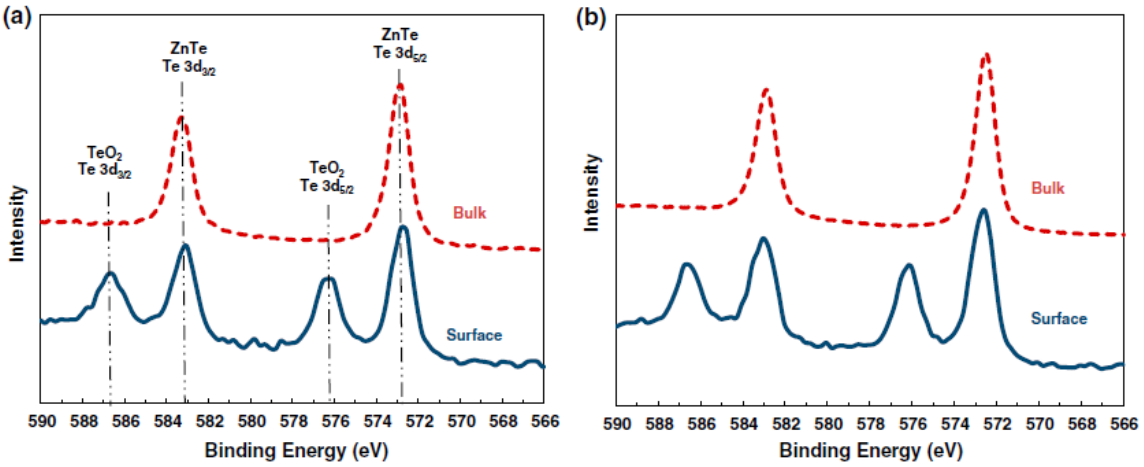

Figure 3.2 X-ray photoelectron spectroscopy data of (a) a film that was not intentionally doped with oxygen, and (b) a film intentionally doped with oxygen by introducing oxygen plasma with partial pressure of 10^{-5} Torr during MBE growth. For both samples, TeO_2 signal was detected at the surface, but not in the bulk[21].

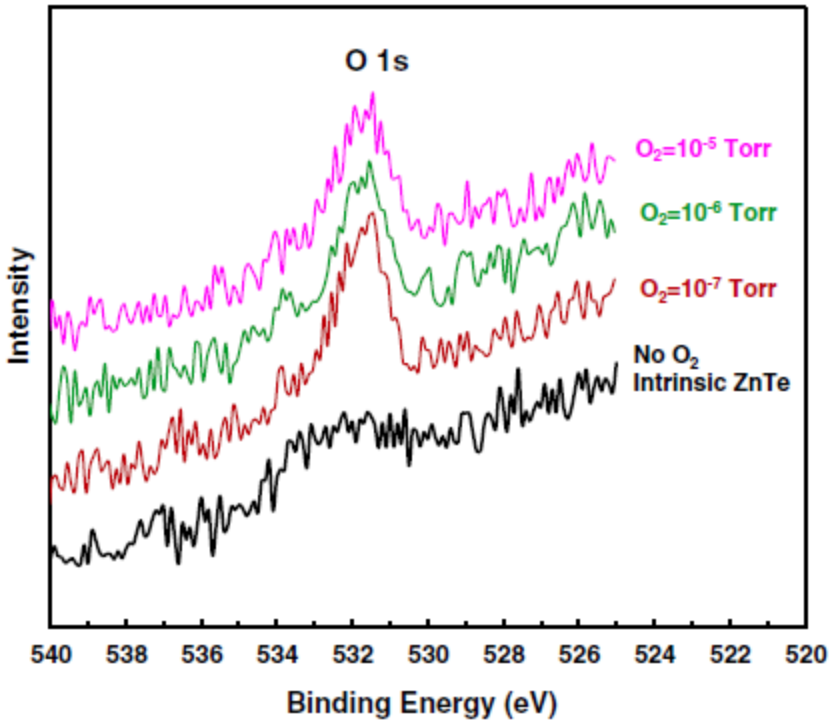

Figure 3.3 XPS data for a film grown without intentional oxygen doping and other films with varying oxygen plasma partial pressure during growth. As shown, the O 1s signal is relatively low for the sample with no intentional incorporation of oxygen[21].

The oxygen concentration was determined by nuclear reaction analysis (NRA) using the $O^{16}(d,p)O^{17}$ response, where a deuteron reacts with O^{16} to form a proton and O^{17},with a beam energy of 1060 keV and the detector placed at 150° from the incident beam. The measurements were done using a 1.7 MV Tandentron accelerator in the Michigan Ion Beam Laboratory at the University of Michigan. An 18 μm thick Mylar film was used to block the strong Rutherford backscattering spectrometry (RBS) signal to enhance the weaker NRA signal. The spectra for the ZnTeO/GaAs samples grown with different oxygen *BEP* of 10^{-7} Torr and 10^{-5} Torr were acquired for a beam collected charge of approximately 500 μC. Each spectrum was fitted using the SIMNRA software to determine the oxygen concentration.

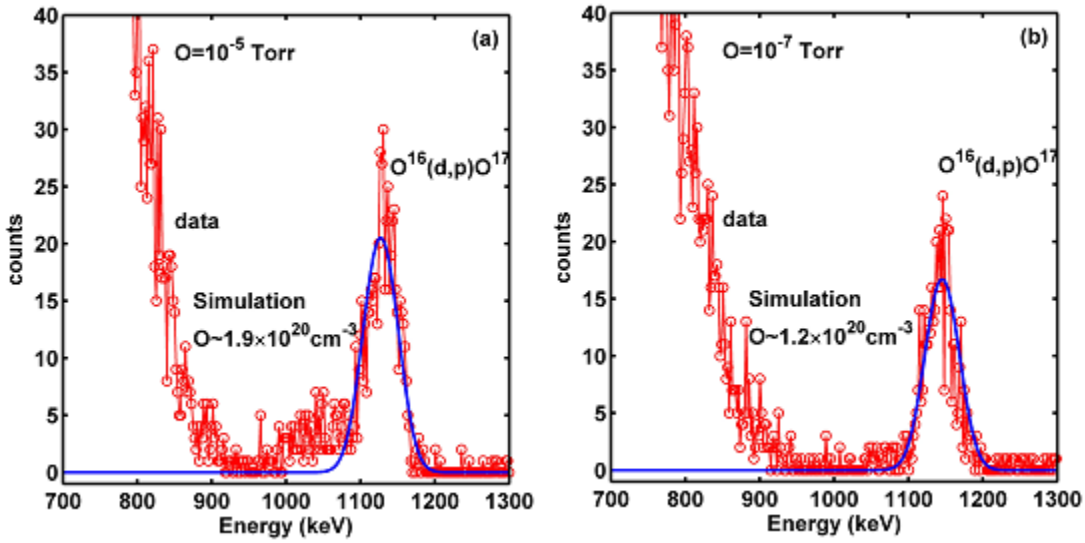

Figure 3.4 NRA spectra and SIMNRA fit for ZnTeO/GaAs growth with (a) *O BEP*=10^{-7} Torr and (b) 10^{-5} Torr, both resulting in an oxygen concentration on the order of 10^{20} cm^{-3}. The samples were grown with T_{sub}=300 °C and *Te/Zn*=1.

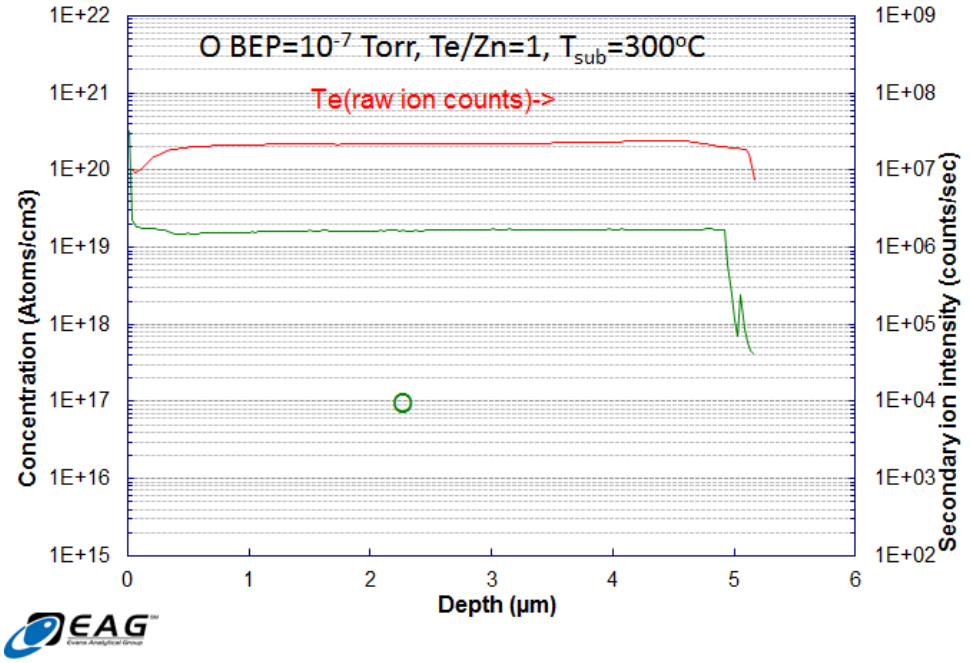

Figure 3.5 Secondary ion mass spectroscopy data for ZnTeO sample grown with O partial pressure of 10^{-7} Torr

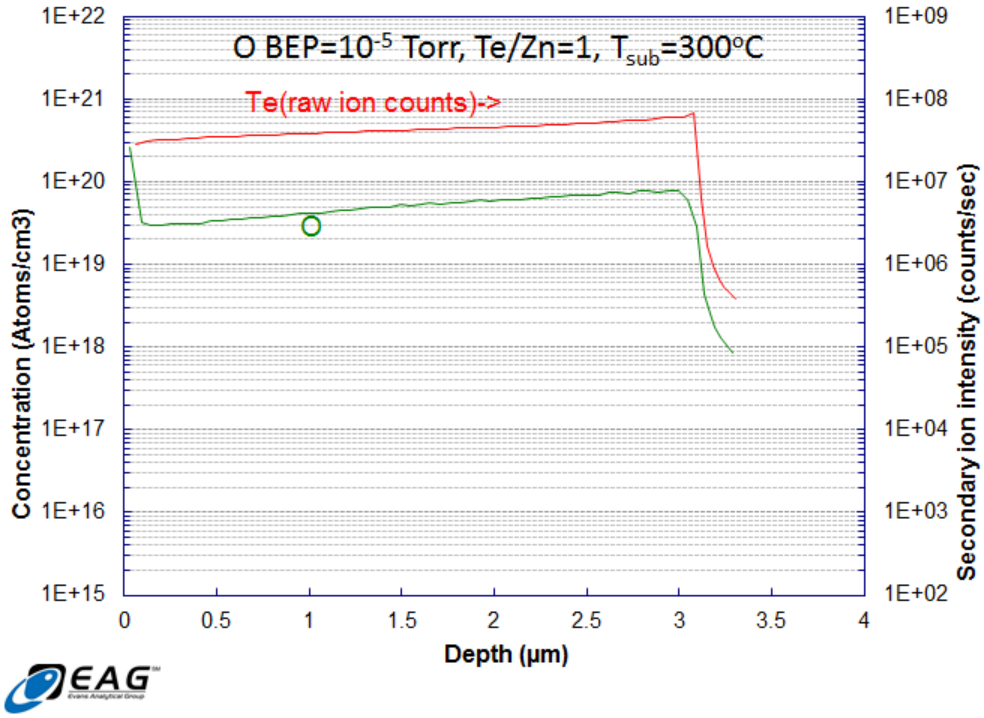

Figure 3.6 Secondary ion mass spectroscopy data for ZnTeO sample grown with O partial pressure of 10^{-5} Torr

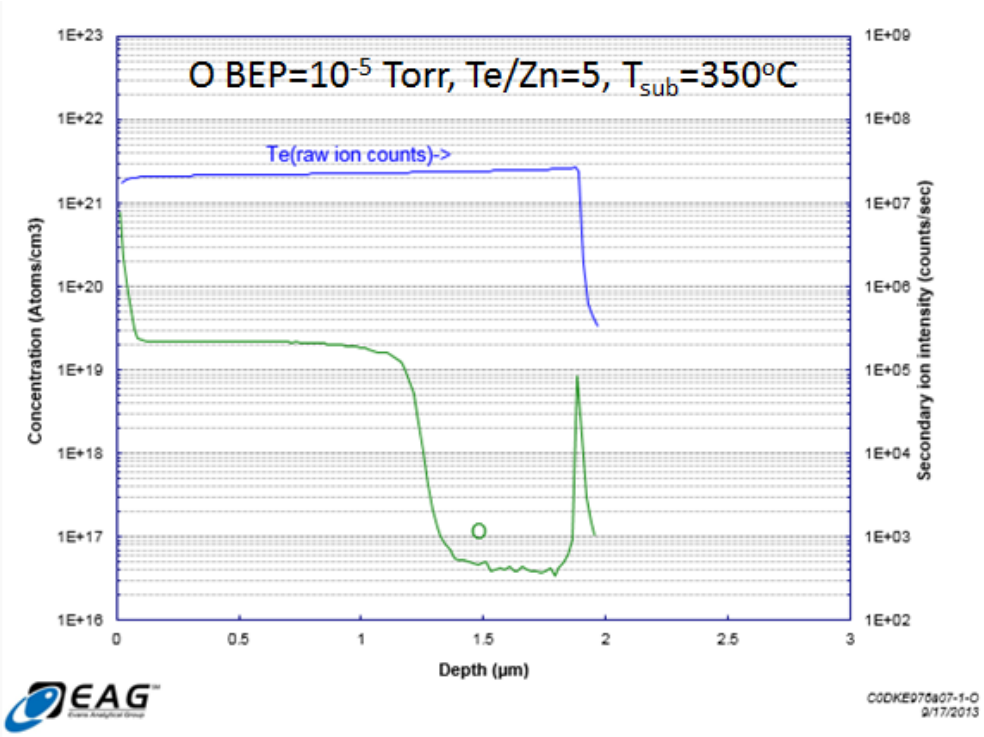

Figure 3.7 Secondary ion mass spectroscopy data for ZnTeO sample grown with O partial pressure of 10^{-5} Torr, T_{sub}=350 ºC, Te/Zn flux ratio of 5.

The oxygen concentration in ZnTe was determined to be $1.2x10^{20}$ cm^{-3} and $1.9x10^{20}$ cm^{-3} for the oxygen partial pressure of 10^{-7} Torr and 10^{-5} Torr, respectively, as shown by the NRA results in Figure 3.4. Despite the dramatically different oxygen partial pressure, the incorporation of oxygen is similar and has been observed repeatedly on a series of samples grown under similar conditions. Independent secondary ion mass spectroscopy (SIMS) measurements have also indicated similar results, where varying the oxygen partial pressure during growth demonstrate a weak dependence of oxygen concentration on oxygen flow rate and an oxygen concentration on the order of 10^{20} cm^{-3}, agreeing with the NRA results, as shown in Figure 3.5 and Figure 3.6. As shown by Figure 3.6 and Figure 3.7, SIMS measurements also show similar oxygen concentration for two samples grown with *Te/Zn*=1, T_{sub} of 300 ºC and *Te/Zn*=5, T_{sub} of 350 ºC,

respectively, indicating that the oxygen incorporation is not strongly dependent on the range of *Te/Zn* ratio and T_{sub} investigated in these experiments. This oxygen concentration corresponds to approximately 0.5 % O in ZnTe, and is not limited by solubility of O in ZnTe or phase transition or separation between zinc blend ZnTe and wurtzite ZnO. Prior reports have in fact demonstrated zinc blend ZnTeO alloys with oxygen content exceeding 1 % using the MBE technique[79]. While we are not aware of calculations in the literature for the solubility limit of O in ZnTe, O ion implantation studies for a similar system CdTe:O have shown saturation behavior for O mole fraction equivalent implant doses beyond 2%[80].

Figure 3.8 shows the high resolution XRD data in the (004) reflection of a sample with no intentional oxygen doping, and samples with intentional oxygen doping but grown with different oxygen partial pressures of 10^{-7}, 10^{-6}, and 10^{-5} Torr. Since oxygen is much more electronegative than Te, when doped in the substitution location, oxygen incorporation would shrink the lattice, leading to an increase in the Bragg angle, as shown in Figure 3.8. The previous section has shown that the oxygen doped samples have similar oxygen concentrations regardless of the oxygen partial pressures used during growth. Therefore, if oxygen is purely in substitutional location, the peak positions for the samples prepared with oxygen partial pressures of 10^{-7}, 10^{-6}, and 10^{-5} Torr should be similar. Since Figure 3.8 shows that these peak positions are different and not monotonic with increasing oxygen partial pressures, indicating that the oxygen configuration within the lattice is likely different for the samples, and the oxygen location is influenced by the oxygen partial pressure used during growth. For example, substitutional O in Te site would shrink the lattice while interstitial O would expand the lattice, so one way to

interpret the data in Figure 3.8 may be different fractions of interstitial and substitutional O in the samples. The following sub-section discusses an experimental technique that more directly measures the oxygen location.

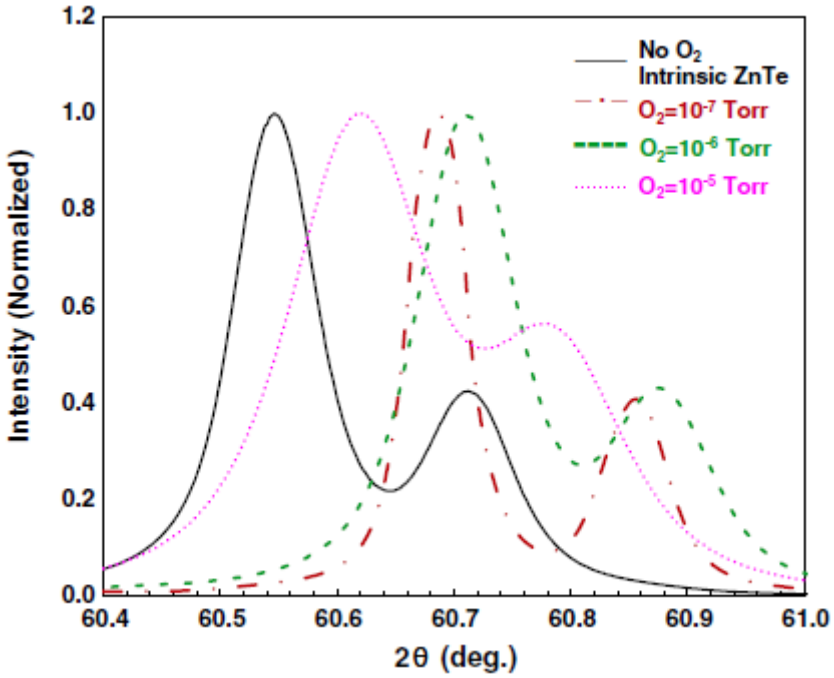

Figure 3.8 XRD data in the (004) reflection for a film grown without intentional oxygen doping and other films with varying oxygen plasma partial pressure during growth. The peak shift is not monotonic with increasing O beam equivalent pressure, suggesting that the oxygen configuration within the samples are likely different[21].

It has been shown experimentally and theoretically that the dopant location with respect to other dopants and with respect to the crystal lattice in highly mismatched alloys (HMA) strongly influences the electronic structure and properties of HMAs.

For example, in the well-studied GaAs:N system, interstitial N has been experimentally demonstrated to strongly influence electronic structure and electronic properties. Interstitial N was shown to be correlated to decreased electron carrier concentration and mobility, indicating carrier trapping and scattering centers[75].

Interstitial N has also been correlated to the observation of persistent photoconductivity in GaAs:N[76].

Similarly for the ZnTe:O HMA system, calculations have shown that the band structure of O_{Te} in isolation significantly differ from O_{Te} in different clustering configurations[77]. The calculation showed that O_{Te} in isolation produces larger CB-IB separation with higher O concentration[77] that is consistent with the band anticrossing (BAC) model[81]. However, when nearby O_{Te} impurities interact with each other, different relaxed atomic positions and electronic structure result in the merging of the CB and IB with increasing oxygen concentration [72, 77], in contradiction with the BAC model.

It is therefore very interesting to study the location of the isoelectronic dopant in HMAs. For the ZnTe:O system, the oxygen location in the dilute limit has been identified as substitutional in the Te site, or O_{Te}, experimentally by Merz[82]. In that study, O^{16} versus O^{18} isotope shift in the photoluminescence (PL) data for the J = 2 (total angular momentum of the excitons trapped by the oxygen impurity) zero phonon line identified oxygen impurity as responsible for the observed PL spectrum. Zeeman splitting data of the J = 2 line did not change in position or number of lines in [100], [111], [011], and [101] directions, indicating that the O was incorporated as a point defect. It was assumed that O substitutional in the Te site because O formed strong tetrahedral bond, and because the PL spectrum was simple[82]. Ling and co-workers performed a calculation comparing the formation energies of O in tetrahedral interstitial sites and substitutional sites for Zn and Te, and found that the O_{Te} has the least formation energy, and clustering O_{Te} leads to significant changes in band structure[77]. Experimental evidence for

interacting O_{Te} was reported by Seong and co-workers[83]. In that work, they excited the sample with a laser with energy less than zero phonon lines of the isolated O_{Te}, and observed a series of zero phonon lines and phonon side bands that looked qualitatively similar to the O_{Te} spectrum. They associated those lower energy signals to interacting O_{Te} pairs with different separations[83]. This is analogous to the better studied N-N pair studies done for the GaP:N system by Thomas and co-workers[84], where zero phonon lines with lower energy but similar phonon sidebands compared to the isolated N_P were observed, the strength of this absorption was proportional to the square of the total N concentration, and that the Zeeman splitting spectrum yielded different number of peaks in different directions. These pieces of evidence were consistent with the view that the observed PL was related to pairs of interacting nitrogen, and so were analyzed as interacting pairs of nitrogen with different separation distances, and were assumed to be in the P substitutional position (N_P)[84].

The above mentioned studies for ZnTe:O showed that O was in the Te substitutional position in the dilute limit, and that O_{Te} interacting with each other may explain some of the PL data and are predicted to change the electronic structure of the material. The above mentioned studies did not mention the $(O\text{-}O)_{Te}$ and $(O\text{-}Te)_{Te}$ split interstitials, where a pair of two O atoms or one O and one Te atom share the Te site in the Zinc Blende lattice. In a similar and well-studied system of GaAs:N, $(N\text{-}N)_{As}$ and $(N\text{-}As)_{As}$ split interstitials have been shown to be dominant at higher N concentrations, and significantly influence the electronic properties of the material. These split interstitials have been predicted to be dominant and introduce energy levels deep in the bandgap with high N concentrations of greater than 4%[85]. The split interstitial energy levels have

been observed experimentally with deep level transient spectroscopy[86], where identification was made by comparing the observed deep levels with As site related defect levels in GaAs and comparing with theoretically predicted split interstitial levels from [85]. Since the GaAs:N and ZnTe:O systems are similar, as Ga and As atoms are similar in size to Zn and Te, and both N and O are highly electronegative, it is reasonable to assume that $(O\text{-}O)_{Te}$ and $(O\text{-}Te)_{Te}$ split interstitials are likely present and important in ZnTe:O samples with high O content.

Nuclear reaction analysis (NRA) channeling is an experiment that can reveal some information on the dopant location within a crystal lattice. When aligned to certain crystal orientations of the Zinc Blende lattice called channels, the bulk atoms would be directly behind the surface atoms, such that a particle beam aligned to a channel would only be scattered by the surface atoms. When not aligned to a channel, the bulk atoms can scatter the incoming particle beam, so that most of the scattered signal is due to bulk atoms. Since a substitutional impurity atom replaces an existing crystal host atom, a bulk impurity atom in the substitutional site would not scatter incoming particles that are aligned to a channel, where as a non-substitutional impurity atom would. Figure 3.9, Figure 3.10, Figure 3.11, and Figure 3.12 compare the host lattice with respect to the ideal interstitial and split interstitial O locations down the <100>, <110>, and <111> channels.

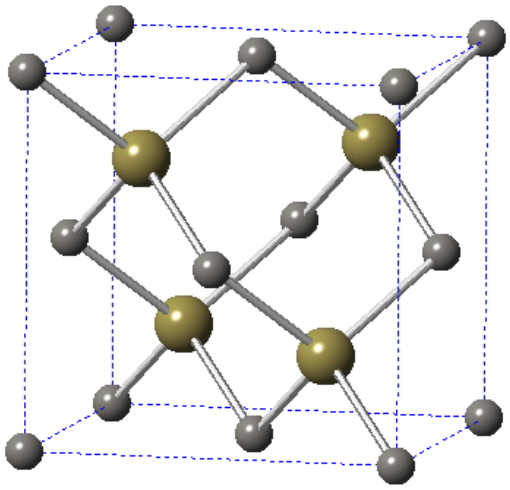

Figure 3.9 ZnTe cubic lattice, with Zn atoms colored grey, Te atoms colored green. Image generated by CrystalMaker software.

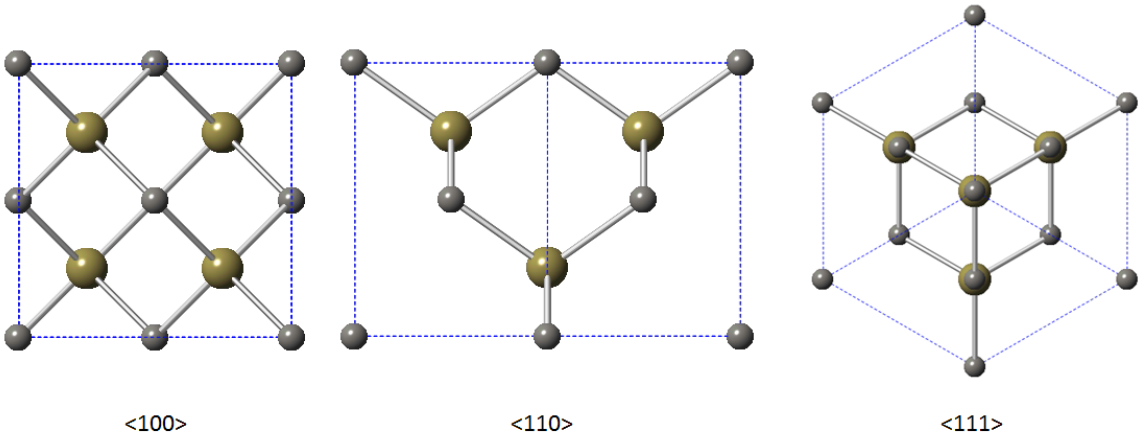

Figure 3.10 ZnTe cubic lattice viewed down the <100>, <110>, and <111> channels, with Zn atoms colored grey, Te atoms colored green. Image generated by CrystalMaker software.

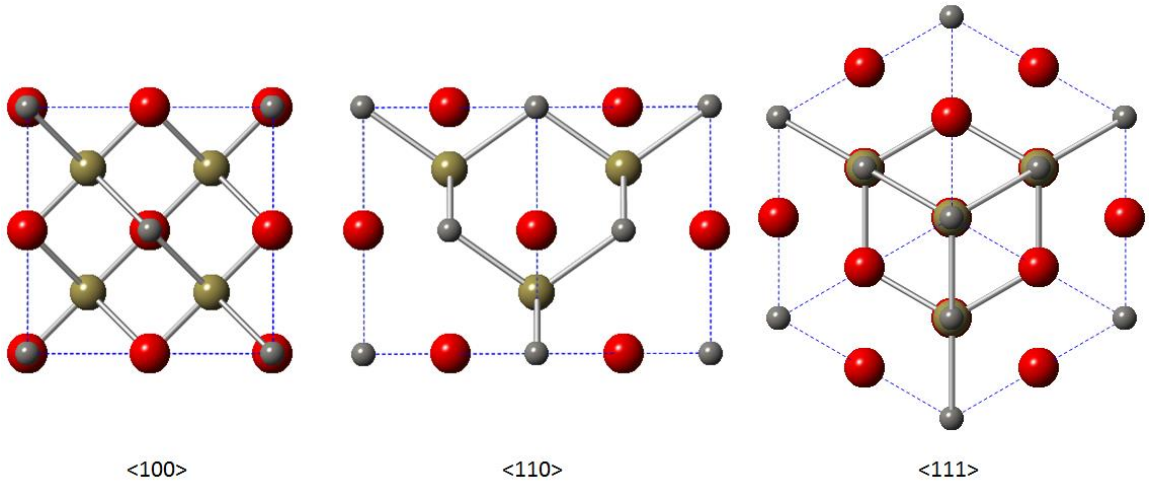

Figure 3.11 ZnTe cubic lattice with O in ideal interstitial position, viewed down the <100>, <110>, and <111> channels. Zn atoms colored grey, Te atoms colored green, and O atoms colored red. Image generated by CrystalMaker software.

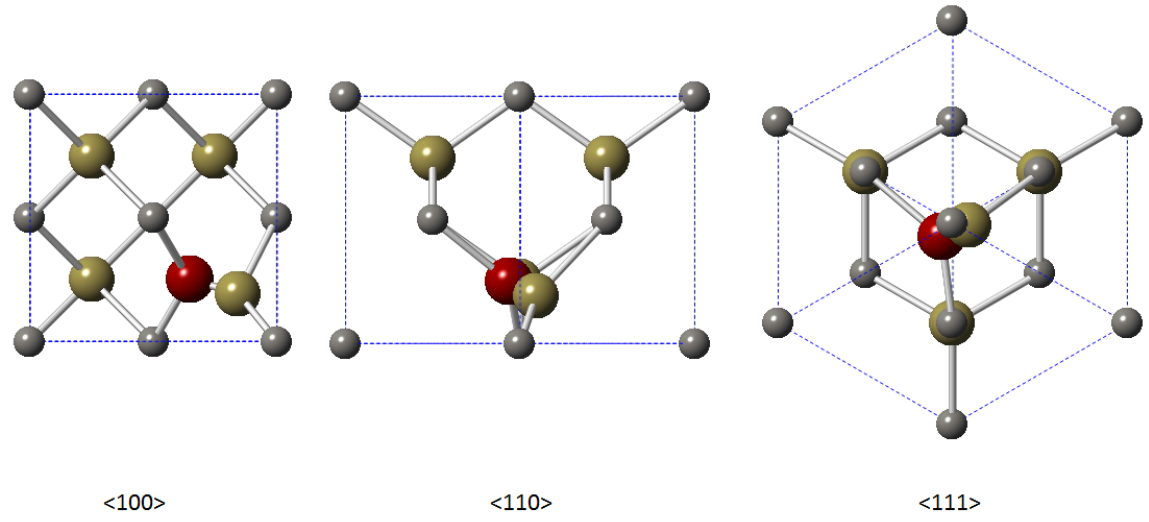

Figure 3.12 ZnTe cubic lattice with O-Te split interstitial in the Te site, viewed down the <100>, <110>, and <111> channels. Zn atoms colored grey, Te atoms colored green. Image generated by CrystalMaker software.

Assuming that the crystal is a uniform, one obtains the following expression for percentage of dopants in the substitutional position[87]:

$$f = \frac{1-\chi(O)}{1-\chi_{\min}(ZnTe)}$$ **Equation 3-3**

, where f is the fraction O atoms in the Te substitutional position, $\chi(O)$ is the ratio between channeling and non-channeling NRA yield for O, and $\chi_{min}(ZnTe)$ is the ratio between channeling and non-channeling RBS yield for the Zn and Te host lattice atoms. In deriving Equation 3-3, the assumption that the film is uniform is assumed, such that z, the fraction of Te sites filled with O, is the same on the surface as it is for bulk, as follows[87]:

$$z = \frac{N_S[O_{Te}]}{N_S[Te_{Te}]} = \frac{N_S[O_{Te}^{surf}]}{N_S[Te_{Te}^{surf}]}$$ **Equation 3-4**

, where $N_S[i]$ is the number of atoms per unit area of species i.

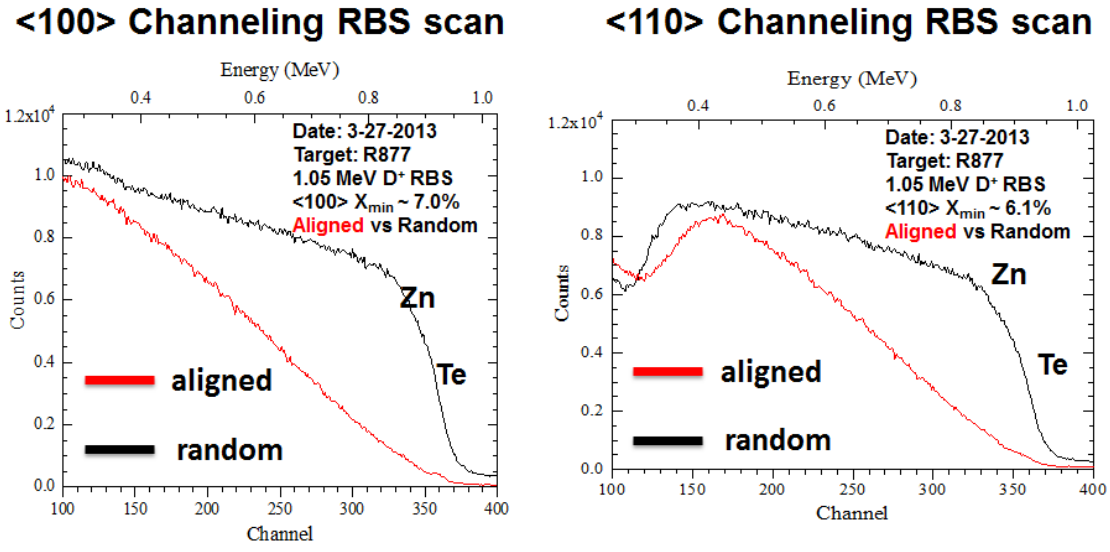

Figure 3.13 Rutherford Back Scattering data for ZnTeO/GaAs(100) sample showing a much reduced signal when aligned to the <100> (left) and <110> channels.

The NRA channeling experiments were performed at Los Alamos National Laboratory. The sample was mounted on a 5 axis goniometer to perform channeling experiment with the $O^{16}(d,p)O^{17}$ NRA signal. The goniometer has a lateral resolution of 1μm and angular resolution of 0.01°. The NRA protons (p) were measured with a silicon surface barrier detector placed at 135°. Rutherford Back Scattering (RBS) signals from the back scattered deuterium (b) beam was collected by another silicon surface barrier detector placed at 167°. The RBS signal was used to align to the <100> and <110> channels by performing an angular scan, as shown in Figure 3.13. For <100> and <110> channels, the $\chi_{min}(ZnTe)$ were 7% and 6.1% respectively. Once aligned to the channels, NRA signal for the $O^{16}(d,p)O^{17}$ protons were recorded, and compared to such signals in random crystal orientation, as shown in Figure 3.14, yielding $\chi(O)$ of 96% and 105% for <100> and <110> channels, respectively. Applying Equation 3-3, we obtain the fraction of O in Te substitution sites $f = 4\%$ and $f = -5\%$ for <100> and <110> channels respectively. The negative number *f* is due to experimental error in measuring a larger than 100% $\chi(O)$ for <110> direction. The important message of the *f* calculation is that it appears that Equation 3-3 suggests that most of the O is not in the substitution position. This low *f* value appears unreasonable given that the *f* values measured for a similar GaAs:N system is typically at least 50% for high N concentration of 4.7×10^{20} cm^{-3}, and 92% for low N concentration of 1.4×10^{20} cm^{-3} [74, 87]. On the other hand, our O concentration is typically approximately 1×10^{20} cm^{-3}. Since our PL data, for example, see Figure 3.16, is similar to the PL spectrum that has been associated with O_{Te} [82], if the *f* calculations are correct, the non substitutional O either have the same energy levels

as O_{Te} or do not emit PL. However, this is unlikely, since HMA dopant location strongly influences electronic structure, as outlined in the introduction of this subsection, and PL signal that is lower in energy than that from isolated O_{Te} has been reported in the literature for high O concentration of 1.09%[88].

One possibility to explain this apparent inconsistency may be that the assumption in Equation 3-4 that the film is uniform is not correct in our samples. For example, typical SIMS data shown in Figure 3.6 shows that the surface has an order of magnitude higher oxygen content than the bulk. The assumption in Equation 3-4, that the ratio of Te sites being filled by O atoms is the same for surface and bulk may not be true, since the surface has significantly higher oxygen concentration. In the similar GaAsN system, for example, it has been shown that at higher N concentration, $(N\text{-}N)_{As}$ and $(N\text{-}As)_{As}$ split interstitials, dominate[85, 86]. Moreover, we also know that the top surface does not have a purely zinc blend crystal structure, since TeO_2 XPS signals were detected at the top surface, as shown in Figure 3.2. The different crystal structure of TeO_2 surface and cubic ZnTe bulk may account in part for the observed independence of the O NRA signal with respect to aligning to the ZnTe bulk <100> and <110> channels. For future studies, it would be interesting to perform an oxide etch immediately prior to loading into the analysis vacuum chamber.

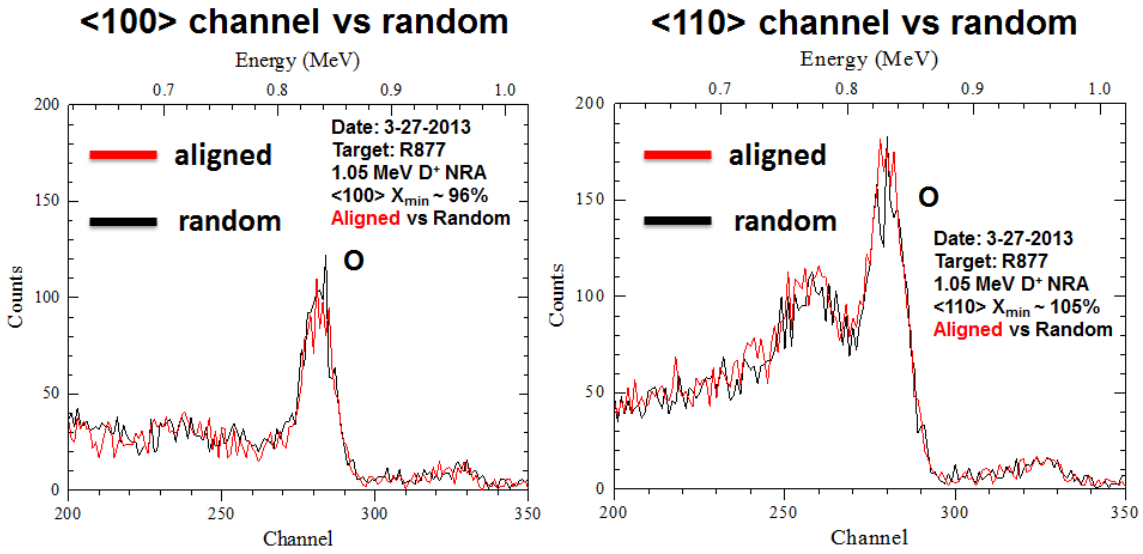

Figure 3.14 Nuclear reaction analysis data for a ZnTeO/GaAs(100) sample for the cases of aligned and not aligned to the <100> (left) and <110> (right) channels.

3.4 Optical properties

ZnTe has a bandgap of 2.4 eV at 20 K, where oxygen incorporation results in electronic states within the bandgap with radiative emission at 1.9 eV. The origin of excitonic peaks near the ZnTe band edge and the identification of the 1.9 eV peak as O_{Te} has been studied previously[82, 89, 90]. Common features in the reported spectrum include sharp excitonic features near the ZnTe band edge, and weak oxygen phonon side band states with a peak at 1.9 eV that consist of phonon replicas associated with ZnTe LO phonons.

PL spectra were collected using a monochrometer, photomultiplier tube, and lock-in techniques. The excitation sources for the setup include a 405 nm solid state laser and a 325 nm He-Cd CW laser. For the 405 nm laser, there is a laser line filter immediately after the laser source, and a 435 nm long pass filter immediately before the

monochrometer. The setup is equipped with a closed cycle helium cryostat that regulates temperature from 20 K to 300 K.

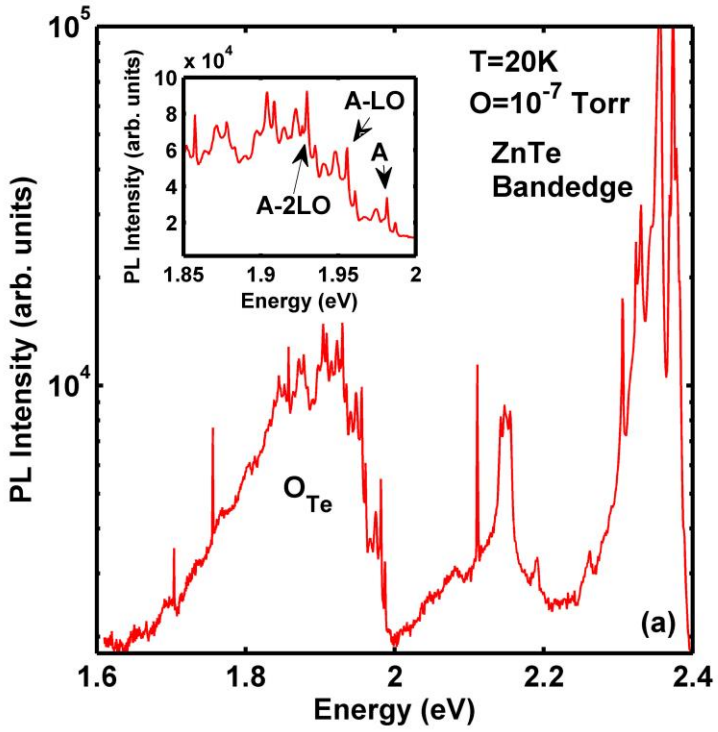

Figure 3.15 Low temperature PL spectra of ZnTeO with *O BEP*=10^{-7} Torr showing the excitonic states near the 2.4 eV ZnTe band edge and the O_{Te} state near 1.9 eV, and (inset) corresponding phonon replicas. The FWHM of the 1.9 eV, 2.15 eV, 2.3 eV features are 127 meV, 21 meV, 9 meV, respectively.

The optical properties of material with low oxygen flow rate are shown in Figure 3.15. The PL spectrum consists of sharp excitonic features near the ZnTe band edge (~2.4 eV at 20 K), a peak at 2.15 eV that is referred to as the Y-band in literature [89, 91, 92], as well as the O_{Te} peak at 1.9eV. Closer examination of the O_{Te} response reveals phonon replicas with a period of 26 meV, corresponding to the ZnTe LO phonon[82, 93]. The ZnTe band edge features are significantly stronger than the O_{Te} peak, in agreement with previous observations[91, 92]. Samples grown with higher oxygen *BEP* (10^{-5} Torr) exhibit a significant increase in PL emission near the O_{Te} peak of 1.9 eV, approximately

two orders of magnitude, coinciding with a quenching of band edge emission (Figure 3.16). The quenching of the band edge emission makes it not possible to track the bandgap size as a function of oxygen concentration in our samples by PL. However, this type of study has been reported in the literature for high oxygen concentration of up to 1% with the photoreflectance technique[79]. The O_{Te} emission for the sample with higher *O BEP* of 10^{-5} Torr exhibits a line shape similar to the established O_{Te} feature, but with increased inhomogeneous broadening.

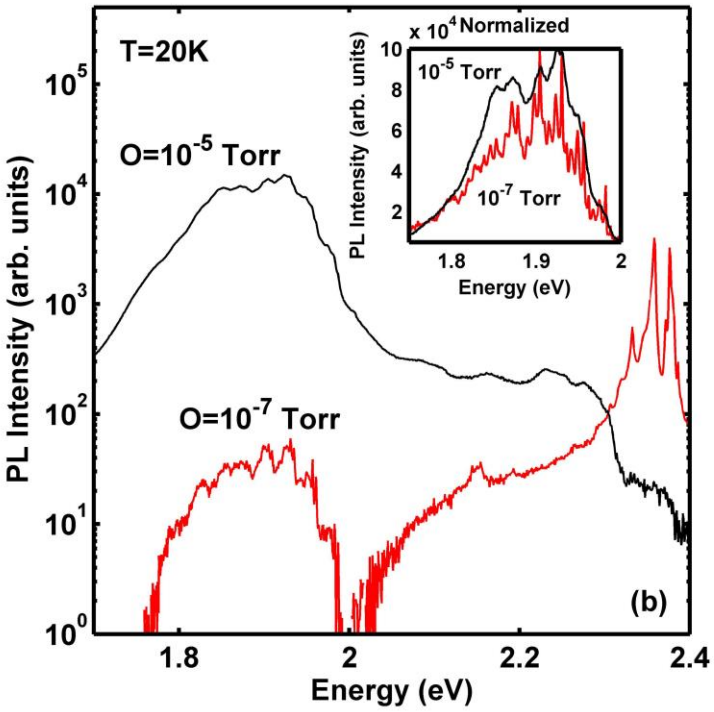

Figure 3.16 Comparison of ZnTeO grown with *O BEP*=10^{-7} Torr and 10^{-5} Torr showing a dramatic increase in the O_{Te} emission near 1.9 eV. The FWHM for the 1.9 eV feature for the *O BEP* = 10^{-5} *Torr* case is 131 meV. The growth conditions for the *O BEP*=10^{-7} Torr and 10^{-5} Torr samples were T_{sub}=300 ºC and *Te/Zn*=1, and T_{sub}=350 ºC and *Te/Zn*=5, respectively.

The NRA and SIMS measurements indicate that the samples grown with 10^{-7} Torr and 10^{-5} Torr oxygen *BEP* both have a similar oxygen concentration of approximately 10^{20} cm^{-3}, as shown in Figure 3.6, Figure 3.13, and Figure 3.14. The dramatically

different PL behavior, yet similar oxygen concentration, suggests that the location of oxygen within the lattice differs. The primary effect of varying the oxygen flow from 10^{-7} Torr to 10^{-5} Torr may be to alter the oxygen organization within the ZnTe lattice.

Native deep level emission in ZnTe has been previously observed[91, 94-97] where prior calculations suggested V_{Zn}[31], Te_{Zn}[98] or Zn_{Te}[99] as likely native defects, and prior experiments have suggested the possibility of V_{Te}[100], or Zn[100] for the observed response at 1.8 eV. The close energetic proximity of the radiative O_{Te} and native deep level emission can confound the interpretation of optical characteristics of ZnTeO material, and are important to distinguish and understand for optoelectronic device applications. In this work, the optical characteristics and relative radiative efficiency of native deep level emission and O_{Te} emission are compared.

The room temperature PL of ZnTeO/GaAs is dominated by a peak near 1.8 eV, distinct from the O_{Te} state near 1.9 eV. The native deep level radiative emission in ZnTe may be a source of the peak at 1.8 eV. To confirm this, a ZnTe sample grown without oxygen was compared before and after RTA annealing (400 ^{o}C for 1 min). The resulting low temperature PL is shown in Figure 3.17, where there is a distinct introduction of the native deep level emission at 1.8 eV upon the RTA treatment. Contrary to conventional wisdom, the introduction of the defect emission actually increases the net radiative emission in comparison to the ZnTe sample prior to RTA, by approximately an order of magnitude. The increase in integrated intensity is even larger than the peak intensity increase due to the broad spectral emission of the native deep level, and is remarkably strong with the observation of strong red emission at room temperature by the naked eye upon mild laser excitation.

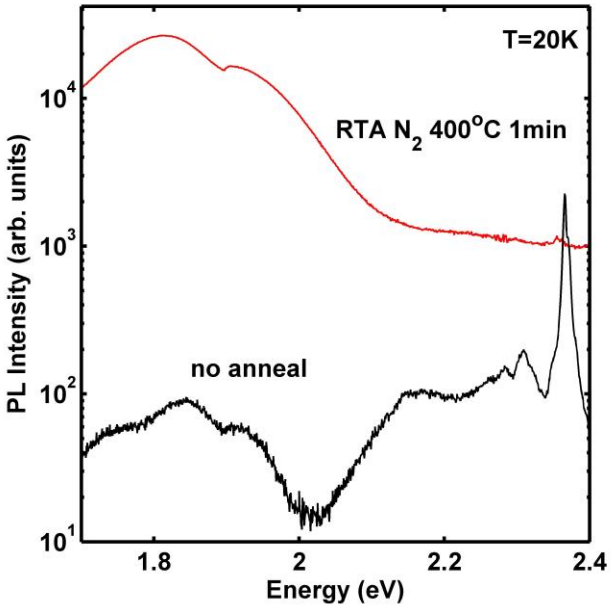

Figure 3.17 Low temperature PL spectra of ZnTe/GaAs before and after RTA annealing, demonstrating a large increase in native deep level emission near 1.8eV. The sample was grown with T_{sub}=300 ºC and *Te/Zn*=1.

Temperature dependent studies were performed on the RTA ZnTe sample and ZnTeO sample with high oxygen partial pressure to compare the nature of radiative defects state near 1.8 eV and the O_{Te} state near 1.9 eV. The temperature dependent PL of the RTA ZnTe sample is shown in Figure 3.18a, with a peak near 1.8 eV at low temperature and gradual red shift with increasing temperature. In contrast, the ZnTeO sample demonstrates two distinct contributions: one centered at 1.9 eV attributed to the O_{Te} emission and one at 1.8 eV attributed to the native deep level emission. The temperature dependent PL for the ZnTeO sample (Figure 3.18b) shows that the O_{Te} emission quenches at increasing temperature, with emission at room temperature dominated by the native deep level emission.

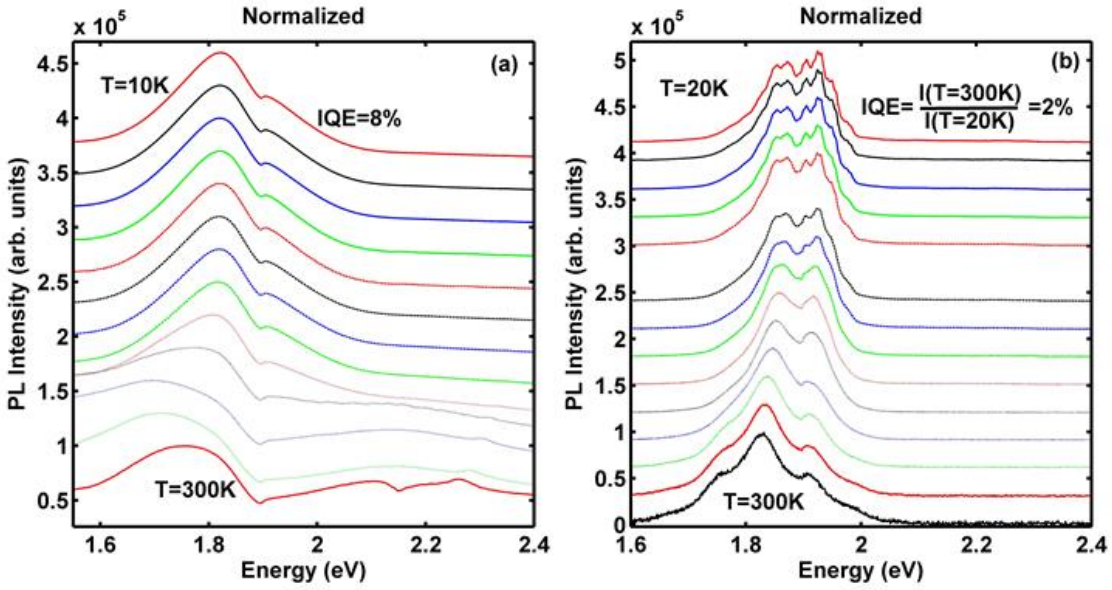

Figure 3.18 Temperature dependent PL for (a) RTA ZnTe and (b) ZnTeO. The data is normalized to illustrate the peak evolution for the O_{Te} state and the defect state. The growth conditions for the RTA ZnTe and ZnTeO samples were T_{sub}=300 ºC and *Te/Zn*=1, and T_{sub}=350 ºC and *Te/Zn*=5, respectively. An *O BEP* of 10^{-5} Torr was used for ZnTeO.

The native deep level emission and O_{Te} emission are relatively strong for the ZnTeO material with high oxygen *BEP*, where the native deep level emission appears to dominate regardless of oxygen content. With this observation, what is desirable for device applications? The internal quantum efficiency (*IQE*) can be defined as the ratio of room temperature PL peak intensity relative to the low temperature PL peak intensity, assuming that non-radiative recombination is suppressed at low temperature. The dominant PL peak intensity at each given temperature was used for the *IQE* experiments. While the correct method for *IQE* determination would use the integrated PL intensities, peak intensities were chosen here for convenience and without significant difference in the interpretation of the data. For the ZnTe RTA sample without oxygen, the *IQE* is approximately 8 %, relative to approximately 2 % for the ZnTeO sample. RTA treatment of the ZnTeO sample results in an overall decrease in PL intensity dominated by native

deep level emission at 1.8 eV (Figure 3.19a). In a separate experiment, we have examined the oxygen content in ZnTeO grown under similar conditions, before and after similar RTA treatment. The SIMS data indicated no detectable change in oxygen concentration in the ZnTeO after RTA, with the only observable difference being a higher oxygen concentration at the surface after RTA.

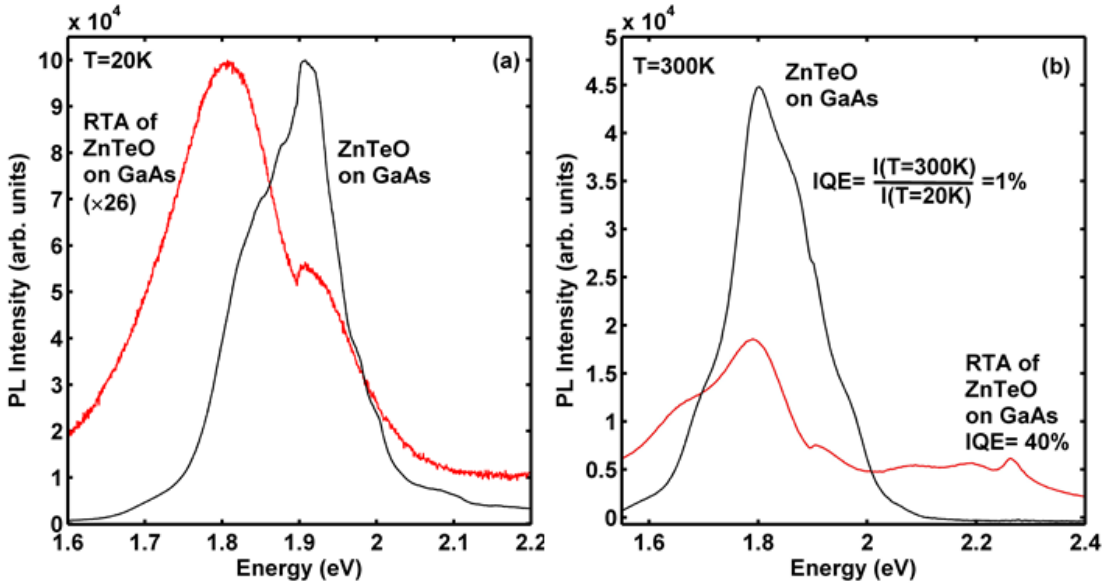

Figure 3.19 Comparison of PL spectra for ZnTeO before and after RTA at (a) *T*=20 K demonstrating reduced PL intensity and red shift towards native deep level emission and (b) *T*=300 K showing dominant emission. The sample was grown with T_{sub}=350 ºC, *Te/Zn*=2, and *O BEP* of 10^{-5} Torr.

The apparent *IQE* from temperature dependent PL measurements increases from 1 % prior to the RTA treatment to 40 % after RTA annealing (Figure 3.19b), consistent with the previous observation that the defect state has a higher *IQE* than the oxygen state. However, the overall PL peak intensity is reduced by a factor of 26, along with the red shift towards the 1.8 eV deep level emission. One possible interpretation is that the RTA may increase the density of native point defects such as V_{Zn}, some of which may serve as radiative defect states at 1.8 eV, while also introducing additional non-radiative

recombination pathways. While the RTA treatment was kept at relatively low temperatures, the favored pathway for point defect formation would be the incongruent loss of zinc, with remaining excess tellurium and/or formation of tellurium precipitates[97]. This is consistent with the increased deep level emission possibly from V_{Zn} and $Zn_{Te,}$ and increased non-radiative recombination centers, possibly due to tellurium precipitates. Despite the apparent radiative efficiency via the *IQE* extraction, the overall decrease in PL emission over all temperatures suggests that the RTA treatment introduces non-radiative recombination pathways that are not frozen out at low temperature. The interpretation that the ratio of PL intensities from room temperature to low temperature reflects the true internal quantum efficiency is therefore not accurate.

The higher PL intensity for samples where oxygen emission is dominant is consistent with independent experiments on the influence of *Te/Zn* flux ratio during growth. Non-optimal *Te/Zn* flux ratio results in reduced overall PL intensity and significant native deep level emission at 1.8 eV. It is unclear whether or not the reduced PL intensity observed in these studies due to RTA or non-optimal *Te/Zn* flux ratio provides a direct correlation between non-radiative recombination pathways and the native deep level emission. At this time, however, the overall radiative emission (peak emission and integrated intensity) are highest for samples where native deep level emission at 1.8 eV is low, underscoring the importance of minimizing these defects for optoelectronic applications.

The introduction of oxygen at varying partial pressure between 10^{-7} Torr to 10^{-5} Torr during MBE growth results in similar oxygen incorporation, but dramatically different optical properties. The suppression of band edge emission and increase in O_{Te}

emission at higher partial pressure, but similar oxygen concentration, suggests that the organization of oxygen within the ZnTe crystal is likely differing. The native deep level emission is induced in ZnTe near 1.8 eV via RTA or non-optimal *Te/Zn* flux ratio during growth. The native deep level emission exhibits reduced temperature dependent behavior and dominates emission at room temperature. However, the overall PL is reduced in samples where the native deep level emission is apparent, suggesting that these defects are related to, or coincide with, non-radiative pathways. These studies suggest that the future development of ZnTeO dilute alloys for optoelectronics relies on the reduction of defects related to the 1.8 eV native deep level emission, despite their radiative nature in proximity to O_{Te} emission.

The absorption coefficient of the VB-IB transition has been studied and is reported in the literature[101]. In this thesis work, we investigated the optical absorption of the IB to CB transition using FTIR, and found that the absorption coefficient is approximately 200 cm^{-1}, as shown in Figure 3.20.

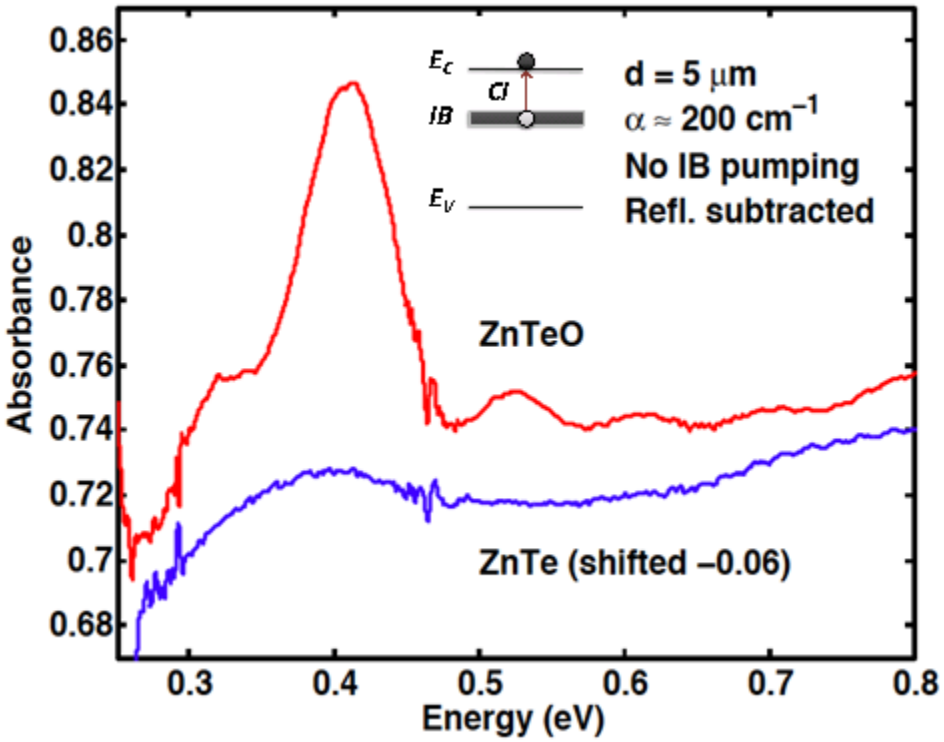

Figure 3.20 Absorption spectrum data obtained by FTIR for the IB-CB optical transition of ZnTeO/GaAs[102].

Chapter 4
ZnTeO Carrier Dynamics

4.1 Introduction

ZnTeO is a promising material for X-ray scintillators and a potentially interesting material for next generation photovoltaics.

In the case of X-ray scintillators, ZnTeO as a X-ray phosphor material has the some of the fastest decay time of ~1 μs, largest gain efficiency of, and lowest afterglow with respect to common material systems[103, 104], which are important for fast time resolution, brightness, and signal to noise, respectively, for the final X-ray detection system. It is interesting to study the carrier dynamics of this material system to further increase to brightness (reduced non radiative recombination) and temporal response (decreased radiative lifetime). Oxygen, the phosphor, introduces an electronic state 0.4 eV beneath the conduction band (CB)[82] of ZnTe, which has a bandgap of 2.3 eV. ZnTeO is a highly mismatched alloy (HMA) where O is much more electronegative than the host Te. O and HMA effects between O and the CB of ZnTe have been predicted to form a sub-bandgap band[1]. When the oxygen concentration is high, the oxygen related states have been said to merge into a band, and called an intermediate band (IB). The radiative transition useful for X-ray scintillator application is the IB-VB transition, where VB is the valence band. Lifetime data of the radiative and non-radiative transitions are

highly relevant since, for example, improved time resolution for scintillators based on this material would rely on reduced lifetime of the IB-VB radiative transition, and a higher brightness of such devices would depend on increased overall non-radiative recombination lifetime.

The IBSC concept exceeds the Shockley Queisser (SQ) efficiency limit by recovering some losses due to bandgap transparency while maintaining the SQ operating voltage. The IBSC utilizes sub-bandgap light to generate carriers via two radiative transitions through an intermediate band in the bandgap (E_G). Assuming only radiative transitions and no electrical contact to the IB, the upper limit on the open circuit voltage (V_{OC}) remains E_G/q[11]. It has been suggested that the oxygen induced IB in ZnTeO may useful to form an IBSC absorber[105]. The two photon current generation process has been confirmed in several material systems the photocurrent was generated with two sub-bandgap CW lasers[106-108]. However, the temporal transients of this process has not been reported.

We report a novel TRPL technique involving two sub-bandgap pumps to study IBSC materials that is sensitive to the transient electron population transfer from IB to CB.

The TRPL data shows simultaneous enhancement of CB-VB PL and depletion of IB-VB PL in ZnTeO, and reveals that the integrated CB PL enhancement is less than the IB PL depletion. Transient absorption data further shows rapid loss of CB carriers in ZnTeO compared to that in a ZnTe sample during femtosecond time scale, suggesting ultrafast recombination pathways. TA data showing lifetime recovery of CB electrons in ZnTeO with increasing visible pump power, and steady state PL data showing blue shift

with increasing excitation laser power suggests that fast recombination pathways can be deactivated by high injection.

4.2 Experimental

ZnTeO was grown on GaSb(100) and GaAs(100) substrates by molecular beam epitaxy with solid sources for Zn, Te, and an ECR plasma source for oxygen. The growth is approximately 1um/hr, the two pump TRPL experiment was performed at Argonne National Laboratory, with an ultrafast laser system with two optical parametric amplifiers (OPA), allowing for wavelength tuning across the visible to near IR. The sample is first excited with a 440 nm pulse that promotes electrons into the conduction band, followed by a second pulse centered at 1270 nm that is more energetic than the IB-CB transition, but less energetic than VB-IB transition. A motorized delay stage controls the delay between the two pump pulses. A streak camera then records the TRPL signal.

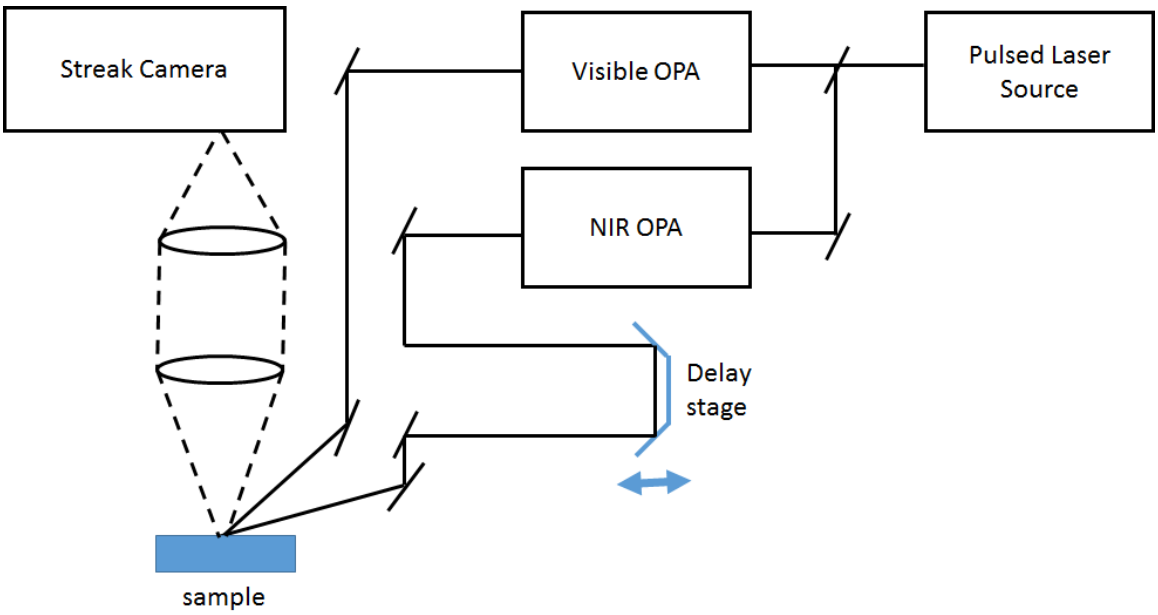

Figure 4.1 Schematic of the two pump time resolved photoluminescence experiment.

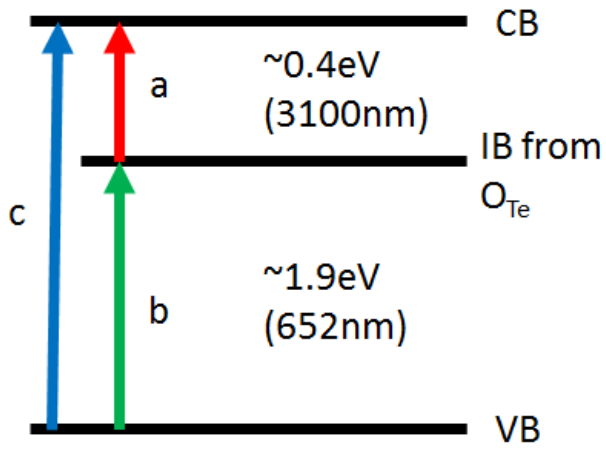

Figure 4.2 Energy levels of the ZnTeO IBSC material, with an IB due to O_{Te} approximately 0.4 eV below the conduction band, and 1.9 eV above the valence band.

4.3 Results and Discussion

The intermediate band is located approximately 0.4 eV below the conduction band, and the bandgap of the material is approximately, 2.3 eV, as shown in Figure 4.2. One important requirement for IBSC materials for IB electrons to be promoted into the CB by absorbing a photon, as opposed to thermal coupling. This radiative IB-CB transition is observed in the steady state in Figure 4.3. A CW visible pump laser injected electrons, some of which relax from the CB into IB. When a near IR laser is introduced, the IB PL near 680 nm reduces in intensity, as shown in Figure 4.3, indicating a loss of the IB electron population, presumably radiatively promoted into the CB. This transition is directly observed with TRPL in Figure. Here a visible pump pulse inject carriers, some of which relax to the IB, resulting in both CB and IB PL, centered at 570 nm and 680 nm respectively, at time zero. The CB PL decays within 10's of picoseconds (ps), while the IB PL has a significantly longer lifetime. After about 1.3 nanoseconds (ns), a near IR

pulse promotes transfers a population of electrons from IB to CB, as seen by the simultaneous appearance of CB PL and depletion of IB PL in Figure 4.4.

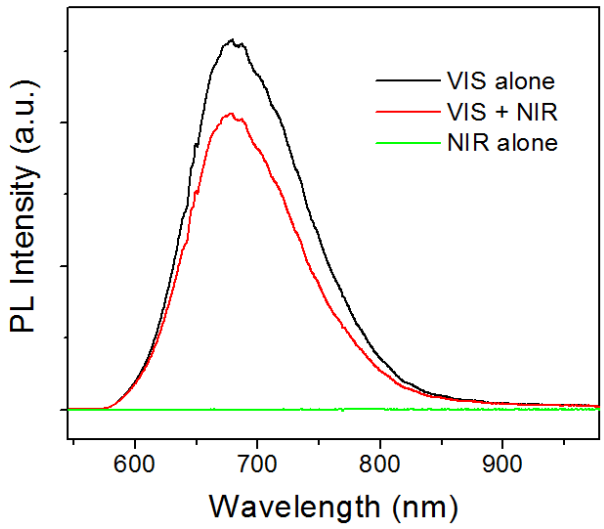

Figure 4.3 Steady state PL data showing IB PL depletion as a result of introducing a near IR pump on top of the above bandgap pump. This implies that IB electrons are radiatively promoted into the CB[109].

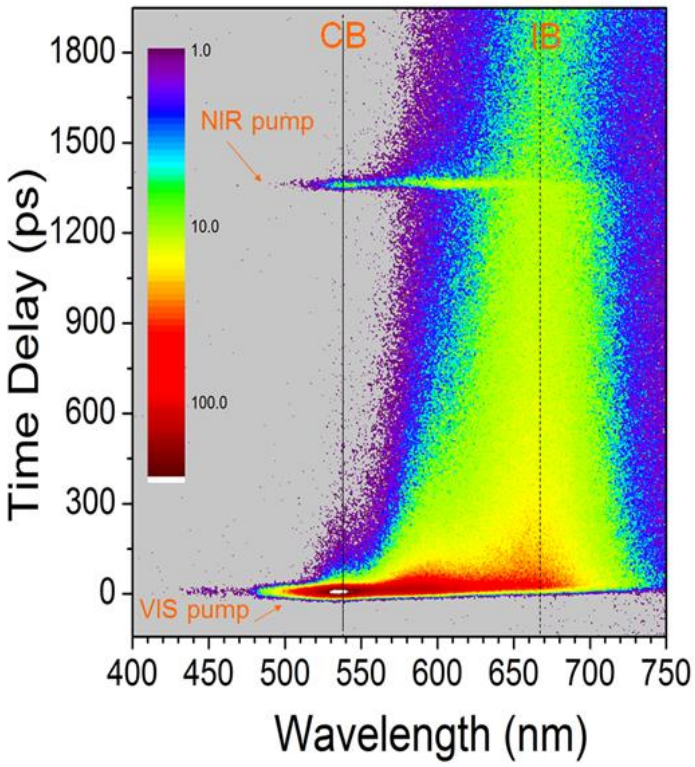

Figure 4.4 Two pump TRPL data showing direct observation of the electron transfer from IB to CB. At time zero an above bandgap pump injects carriers into the CB, some of which relaxes to the IB, resulting in both CB and IB PL. 1.3 ns later a near IR pulse transfers some electrons from IB to CB, resulting in simultaneous enhancement of the CB PL and depletion of the IB PL[109].

While the above demonstrates radiative transition between IB and CB, the additional current in IBSC needs to be injected by sub bandgap photons alone. This two sub-bandgap photon carrier generation is shown in Figure 4.5a. At time zero the sample is excited with a sub bandgap visible pump, and some CB PL is observed due to two photon absorption present at high excitation intensities. Approximately 150 ps later, a below bandgap near IR pump that is larger in energy than CB-IB, but less than IB-CB excites the sample, resulting in significant CB PL. This implies that the first pulse promoted electrons into the IB, and the second pulse promoted electrons into the CB, thus completing the carrier generation with two sub-bandgap radiative steps.

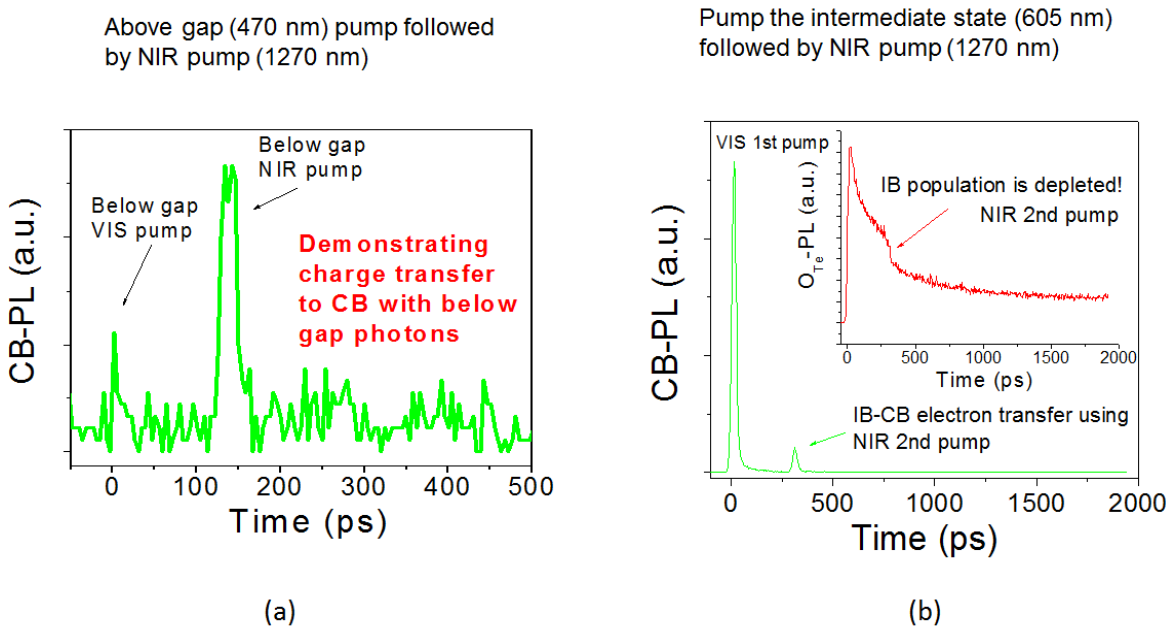

Figure 4.5 (a) visible sub-bandgap pulse followed by a near IR sub-bandgap pulse approximately 150 ps seconds later excited the sample, resulting in CB PL. This demonstrates CB electron generation from a two-step sub-bandgap radiative process. (b) Time slices at CB and IB wavelengths of the two pump TRPL data. The data shows simultaneous enhancement of the CB PL and depletion of the IB PL when the near IR pump was introduced[109].

Besides direct observation of IB to CB population transfer, the time resolution in the reported two pump TRPL provides quantitative accounting of the population transfer, as well of lifetime information important for IBSC device design. Figure 4.5b and its inset are CB and IB wavelength slices, respectively, of two pump TRPL data similar to that shown in Figure 4.4. A visible pump pulse injects carriers, some of which relaxes to the IB, resulting in both CB and IB PL that decays with respect to the time axis. Approximately 270 ps later, a near IR pulse promotes some electrons from the IB to CB, resulting in a simultaneous spike in CB PL intensity and drop in IB PL intensity. Figure 4.4 also reveals that the integrated IB PL depletion is significantly more than the CB PL accretion, implying recombination mechanisms faster than detectable by the TRPL system.

One common approach to effectively remove the SRH centers is by filling them with high injection or through doping. CB electron lifetime recovery is demonstrated in the transient absorption (TA) data in Figure 4.6a, which shows increased lifetime as a result. Figure 4.6b shows similar trap filling effects in steady state. The IB PL blue shifts towards the O_{Te} peak near 1.9 eV with increasing visible pump power, suggesting that radiative contributions from lower energy traps are filled with increasing injection, so that relaxing the O_{Te} energy level becomes more likely. As shown, the fast recombination path ways present with oxygen incorporation may be remedied by high light injection, for example concentrator solar cells, or potentially by intentional degenerate doping.

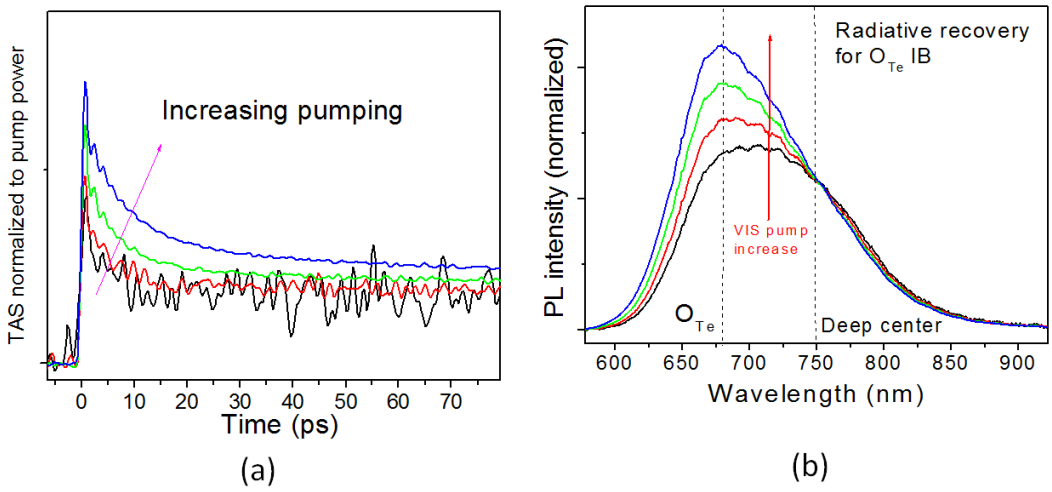

Figure 4.6 (a) Transient absorption data showing that the ZnTeO CB electron lifetime increases with increasing visible pump power, demonstrating trap filling. (b) PL data showing blue shift towards the O_{Te} peak at 1.9 eV as a result of increased excitation laser power, indicating that lower energy radiative traps are being filled[109].

4.4 Conclusion

This work presents a novel two pump TRPL technique to study transient electron excitation and relaxation in IBSC absorber materials. We show that for the ZnTeO system radiative electron transfer from the IB to the CB, as well as two step sub-bandgap carrier generation with two successive sub-bandgap photons, as required for IBSC device implementation. The CB lifetime was measured to be in the picosecond time scale, likely due to non-radiative recombination. CB lifetime recovery with increasing visible pump power, and IB PL blue shift towards the O_{Te} peak with increasing pump intensity. This suggests the fast recombination path ways present with oxygen incorporation may be remedied by high light injection, for example concentrator solar cells, or potentially by intentional degenerate doping.

Chapter 5
Devices Based on ZnTeO

5.1 Prior Work

IBSCs typically have a p-i-n device structure, where the IB material in the "i" region is electrically isolated from the contacts. While a homojunction design would ensure lattice matching of the device, II-VI materials can typically only be doped either n-type or p-type, but not both[31, 99, 110, 111]. One common explanation is self-compensation[31, 112]. Our absorber semiconductor ZnTe can easy be doped p-type by nitrogen, but it is difficult to dope it n-type, potentially due to self-compensation [99, 112] by native defect levels close to the VB in ZnTe. The presence of such native defects means the ZnTe is likely natively lightly p-type without intentional doping. Therefore, a different semiconductor that can be doped n type is needed to form an electrical junction with p-ZnTe.

To form an electrical junction with p-ZnTe, the first demonstration of ZnTeO IBSC, the electrical junction was formed with epitaxial n-type GaAs grown on n-GaAs substrate [70], as shown in Figure 5.1(a). In that work, the authors achieved sub-bandgap photovoltaic response, as well as demonstrated current generation with sub-bandgap light, a key IBSC principle. The open circuit voltage (V_{OC}) was approximately 0.45 V under AM 1.5 illumination. Ideally the V_{OC} should be limited by the material bandgap,

which is 2.3 eV for ZnTe. There is a 7 % lattice mismatch between the ZnTe/GaAs heterojunction, therefore high dislocation density is expected, as shown in Figure 2.6. The shunt path through the dislocations likely reduced the V_{OC}.

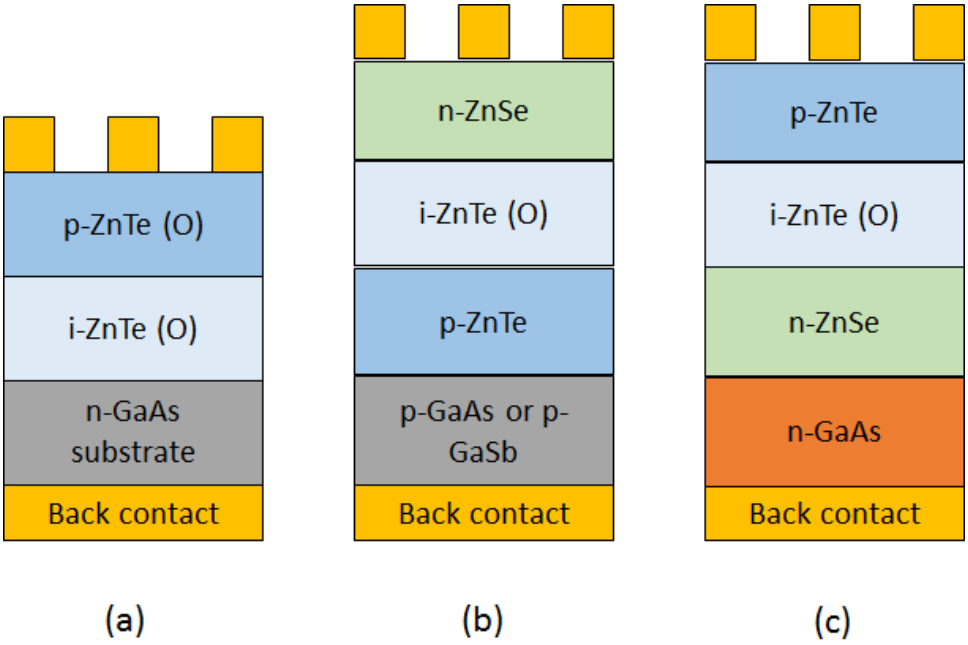

Figure 5.1 Different IBSC device structures. (a) device structure of the first demonstration of ZnTeO IBSC[70], (b) our n on p device structure, and (b) our p on n device structure.

5.2 Heterojunction Improvement

We developed near lattice matched growth of ZnTe on GaSb substrate to reduce the dislocation density, as described in Chapter 2. In addition, we also placed n-ZnSe as the top layer of the cell so as to serve as a window layer. The new device structure is shown in Figure 5.1(b). ZnSe has a larger bandgap than ZnTe, and therefore can transmit light that can be absorbed by the ZnTeO absorber. The larger bandgap of ZnSe also serves as a minority carrier blocking layer, which reflect the carriers away from the non-radiative recombination centers at the highly defective top interface between ZnSe and ZnTe. The

window layer significantly increased the above bandgap external quantum efficiency (EQE) of the devices, as shown in Figure 5.2. The combination of using a window layer and growing ZnTe on a lattice matched substrate increased the V_{OC} to 0.85 V, as shown in Figure 5.3. While a large improvement, 0.85 V is still quite small compared to the bandgap of the material at 2.3 V. This is likely due to the defective interface between ZnSe and ZnTe, as there is a 7 % lattice mismatch there. To reduce dislocations, we graded the lattice mismatch between ZnSe and ZnTe. By doing this we achieved a V_{OC} of more than 1 volt. While we improved the solar cell, significant challenges remain.

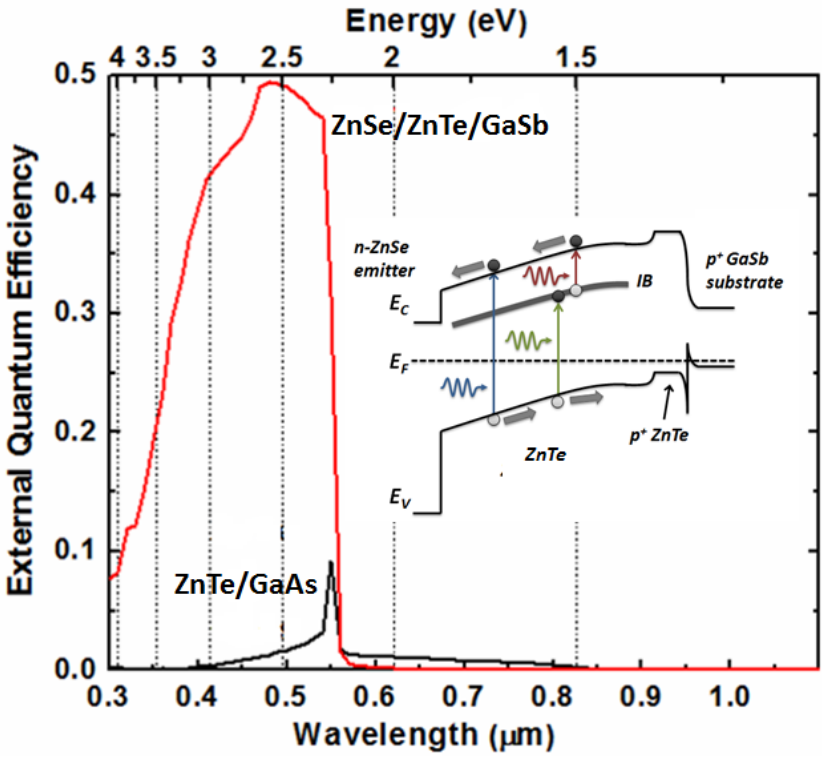

EQE Measurements thanks to E. Antolin, E. López, I. Ramiro, E. Hernández, I. Artacho, A Martí and A.Luque, *Instituto de Energía Solar, Universidad Politécnica de Madrid, Madrid, Spain*

Figure 5.2 External quantum efficiency data showing significant improvement for above bandgap light response as a result of adding a window layer.

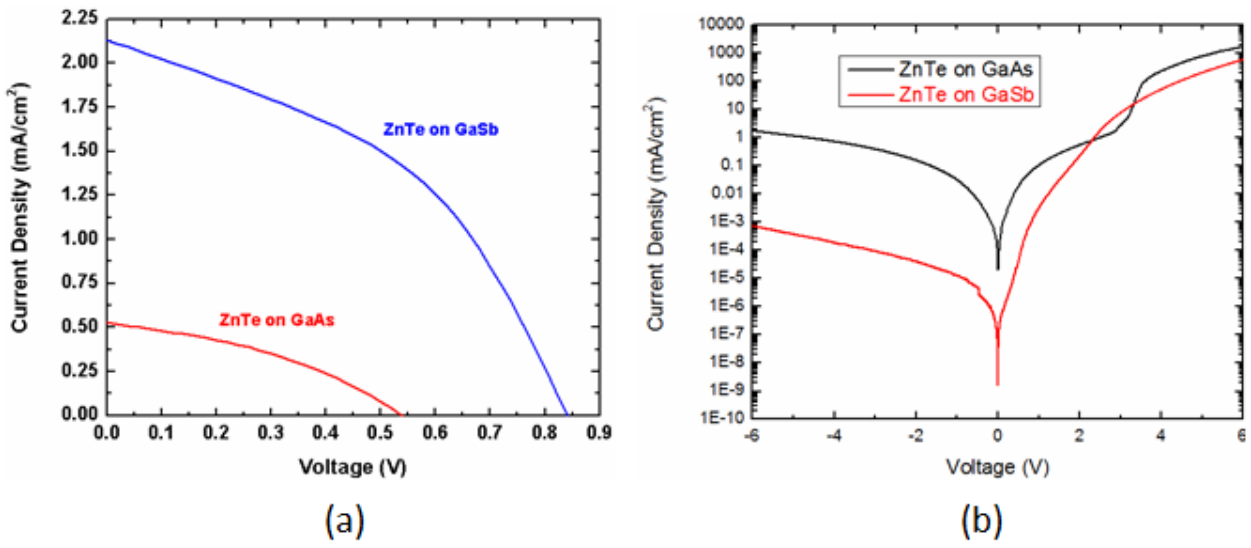

Figure 5.3 I-V curves of ZnTe based solar cells in (a) linear scale and (b) log scale, showing the growing on near lattice matched substrate improves device performance in terms of larger open circuit voltage and reduced dark current.

5.3 Sub-bandgap EQE response

As described in Chapter 1, one of the reasons intermediate band solar cells (IBSC) has a higher thermodynamic efficiency limit compared to a traditional single junction cell is because IBSCs can generate current from using sub-bandgap light. One way to study this behavior is to look at the external quantum efficiency (EQE), defined as the ratio between the electrical current extracted and the monochromatic photon current incident on the device. Sub-bandgap EQE response would indicate that sub-bandgap photons generate current.

For this study, the device structure used was p-ZnTe on n-ZnSe and n-GaAs substrate, as shown in Figure 5.1(c). The bandgap of ZnTe is approximately 2.3 eV. For a device without intentional oxygen doping, no significant sub-bandgap response is

observed, as shown in Figure 5.4. For a device with intentional oxygen doping, a small sub-bandgap response is observed, as shown in Figure 5.5.

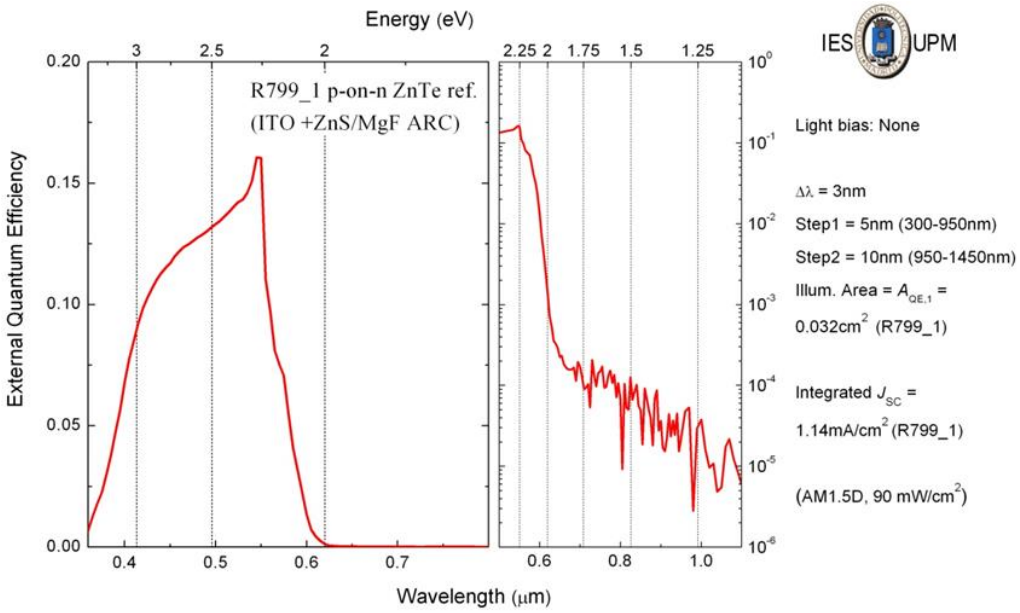

EQE Measurements thanks to E. Antolin, E. López, I. Ramiro, E. Hernández, I. Artacho, A Martí and A.Luque, *Instituto de Energía Solar, Universidad Politécnica de Madrid, Madrid, Spain*

Figure 5.4 EQE of a reference diode without intentional oxygen incorporation.

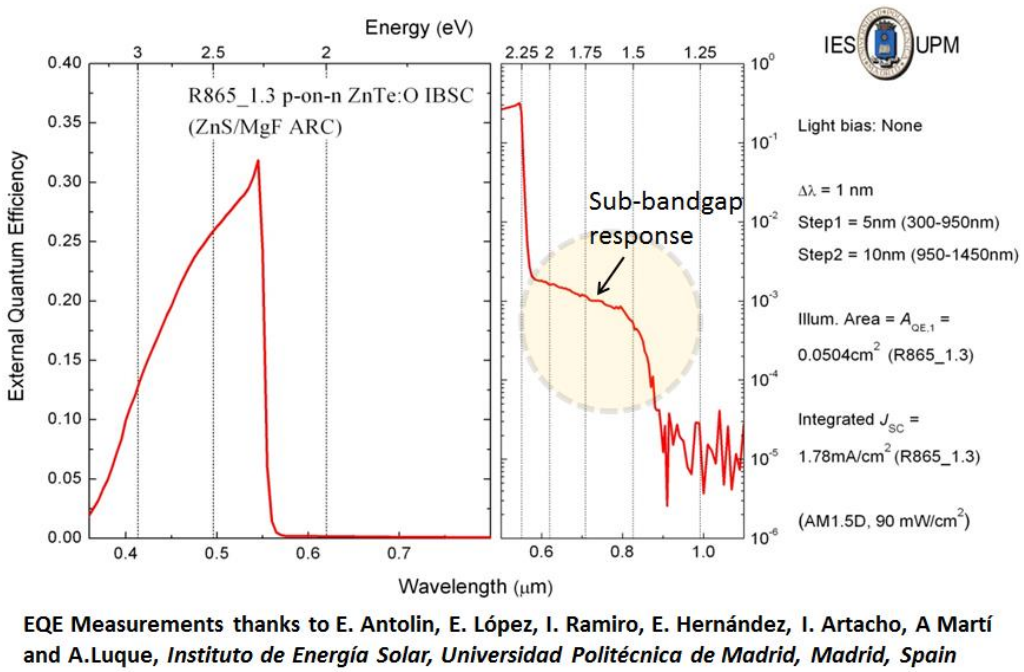

Figure 5.5 EQE of a ZnTeO IBSC device with small sub-bandgap response.

5.4 Improvements Associated with $ZnCl_2$ Doping

Chapter 4 revealed that the lifetime of conduction band electrons in ZnTeO is short (in the picosecond time scale), so that most of conduction band electrons gains from sub-bandgap photon generation is quickly decayed to the intermediate band or valence band before being collected. The fast recombination from CB to oxygen induced IB is unlikely to be radiative, since, as shown in Chapter 3, the IB-CB transition has a low absorption coefficient of approximately 200 cm^{-1} [102].

We explored the use of Cl as a way to passivate this non-radiative recombination pathway, since heating of CdTe material in $CdCl_2$ is reported to improve CdTe material quality in CdTe thin film solar cell technology[8]. We introduced Cl using a solid $ZnCl_2$ effusion cell during ZnTe(O) MBE growth, and fabricated devices with the following active regions: ZnTe, ZnTe:Cl, ZnTeO, ZnTeO:Cl. I-V curves were taken from

approximately 10 K to 300 K under halogen lamp illumination, and activation energy E_a associated with the open circuit voltage (V_{OC}) was calculated using the intercept and slope of the V_{OC} vs temperature curve. The results are summarized in Table 5-1. As shown by the results calculated by the slope method, the Cl doping significantly improves the ZnTeO material E_a while leaving that for the ZnTe material unchanged. This may suggest that Cl passivates some non-radiative recombination pathways in ZnTeO material. Carrier lifetime data is needed to confirm this.

Table 5-1 Ea extracted from the intercept and the slope of the VOC versus T curve of p-i-n solar cells with i active regions of ZnTe, ZnTe:Cl, ZnTeO, and ZnTeO:Cl.

Name	Structures	E_a, eV From intercept	E_a, eV From slope
R1024	ZnTe	1.83	1.99
R1032	ZnTe:Cl:O	1.62	1.81
R1033	ZnTe:Cl	1.62	1.97
R1034	ZnTe:O	1.43	1.57

Chapter 6
O Doped II-VI Ternaries for IBSC

II-VI ternary compounds allows for tuning of the bandgap to the 2 eV that is ideal for IBSCs, as outlined in Chapter 1. The three ternary II-VI systems that we explore are the ZnSeTe, CdMgTe, and CdZnTe system. The bandgap versus lattice constant curves of these three material systems and some common substrates are plotted in Figure 6.1. Our approach is to tune the bandgap to 2 eV, and then dope with oxygen to form the IB. Figure 6.2 shows the location of the oxygen level with respect to the conduction and valence band edges of the end point materials of ZnSe, ZnTe, and CdTe for these ternary alloy systems. Since the O level is near the conduction band edges, we expect oxygen induced IB to be close to the conduction band. One question is whether or not IB can be formed in II-VI alloys with IB doping. We start with the ZnSeTe system to demonstrate this proof of concept, as we had already developed ZnSeTe alloy growth for improving devices, as discussed in Chapter 5.

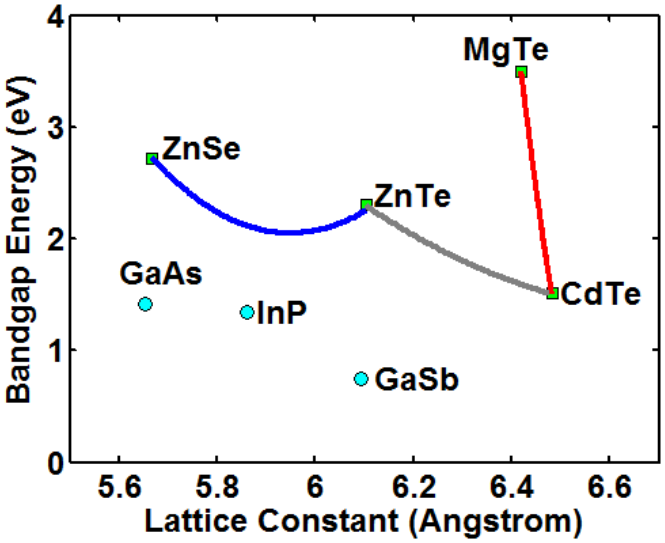

Figure 6.1 Lattice constant to bandgap plot for ZnSeTe, CdZnTe, CdMgTe II-VI ternary alloy systems, as well as common III-V substrates with lattice constants close to these material systems.

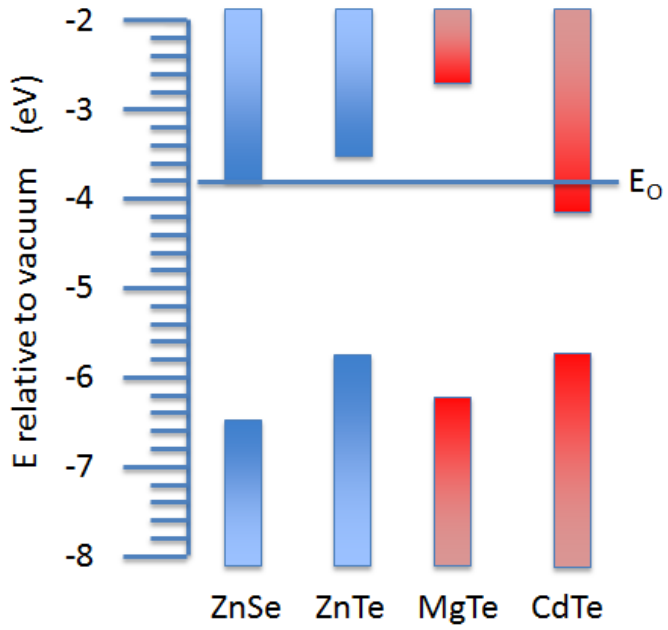

Figure 6.2 Relative energy levels of the local oxygen state with respect to the conduction and valence band edges of the end point semiconductors of the II-VI ternary alloys of interest[113, 114].

6.1 ZnSeTeO

As shown in Figure 6.1 and Figure 6.2, $ZnSe_{0.37}Te_{0.63}$ has a room temperature bandgap of near 2 eV, and that we expect an IB formation near the CB due to the proximity of the oxygen level to the CB edge of ZnSeTe. Figure 6.3 shows that the end point materials of the ZnSeTe system, namely ZnSe and ZnTe, both experience large red shifts when doped with oxygen, indicating oxygen induced IB. We therefore hope that ZnSeTeO alloy would experience a similar redshift as a result of oxygen incorporation.

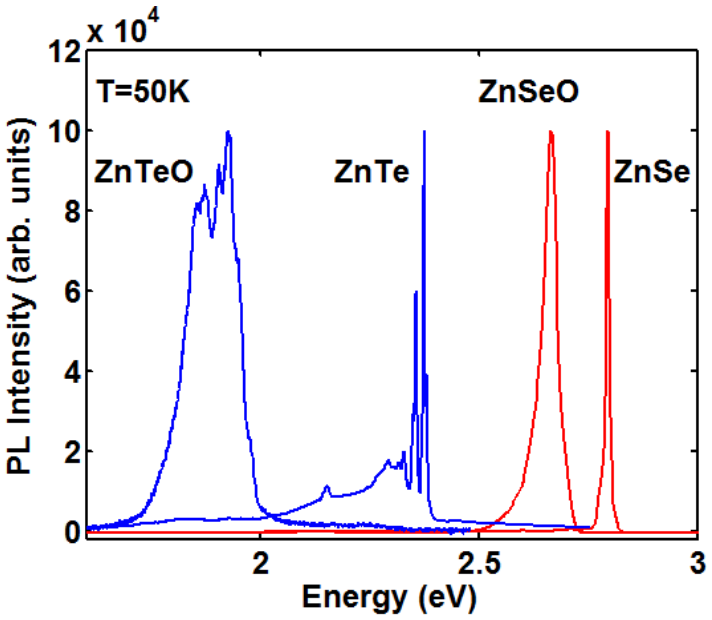

Figure 6.3 Low temperature PL for ZnTe, ZnTeO, ZnSe, ZnSeO, showing large redshift as a result of oxygen incorporation. The FWHM of the ZnTeO, ZnTe, ZnSeO, ZnSe features are 131 meV, 3 meV, 37 meV, 9 meV, respectively.

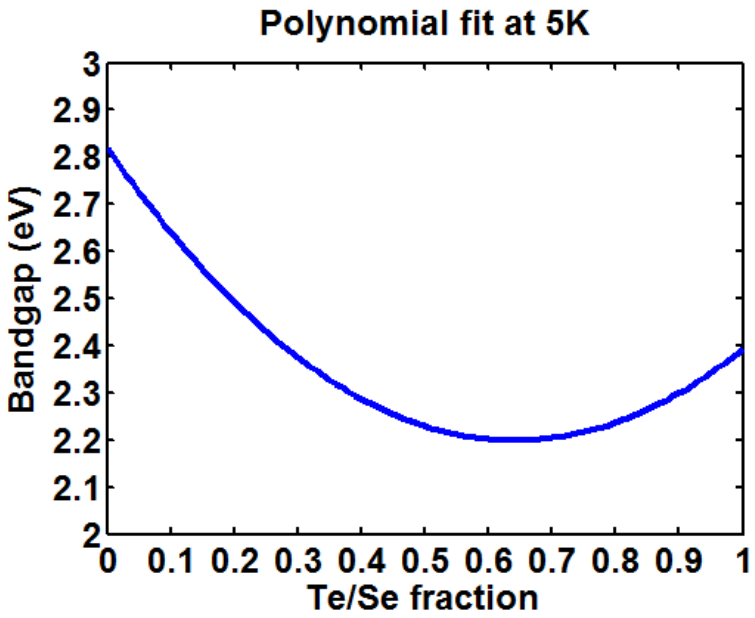

Figure 6.4 [115] Low temperature polynomial fit of the bandgap energy to Te/Se fraction.

The materials where synthesized by MBE on InP(100) substrates, since ZnSeTe is near lattice matched to InP(100) near the 2 eV bandgap region that is ideal for IBSC absorbers, as shown in Figure 6.1. $ZnSe_{0.37}Te_{0.63}$ has a room temperature bandgap of 2 eV, whereas $ZnSe_{0.53}Te_{0.47}$ is lattice matched to InP(100) substrate[115]. The InP(100) substrate was heated to 400 ^{o}C for 5 min to desorb the oxide, and the ZnSeTe growth was initiated. The Zn, Se, Te fluxes were $1x10^{-6}$, $2x10^{-6}$, and $1x10^{-6}$ Torr, respectively. The substrate temperature was 300 ^{o}C. The alloy composition was controlled by using Zn and Te fluxes that are higher than Se flux, and varying the Se flux. This was done following the recommendation of [116], which observed that that Se is preferentially incorporated over Te. The O partial pressure was 10^{-5} Torr, with 1sccm O flow rate, and 50 mA of plasma current.

We studied structural properties of the ZnSeTe/InP sample with X-ray diffraction (XRD). Figure 6.5 is XRD data in the 004 reflection for ZnSeTe/InP(100), showing near

lattice matched ZnSeTe material. However, the ZnSeTe peak is broad, and we appear to have multiple peaks, so the II-VI to III-V MBE growth of this material still needs to be optimized.

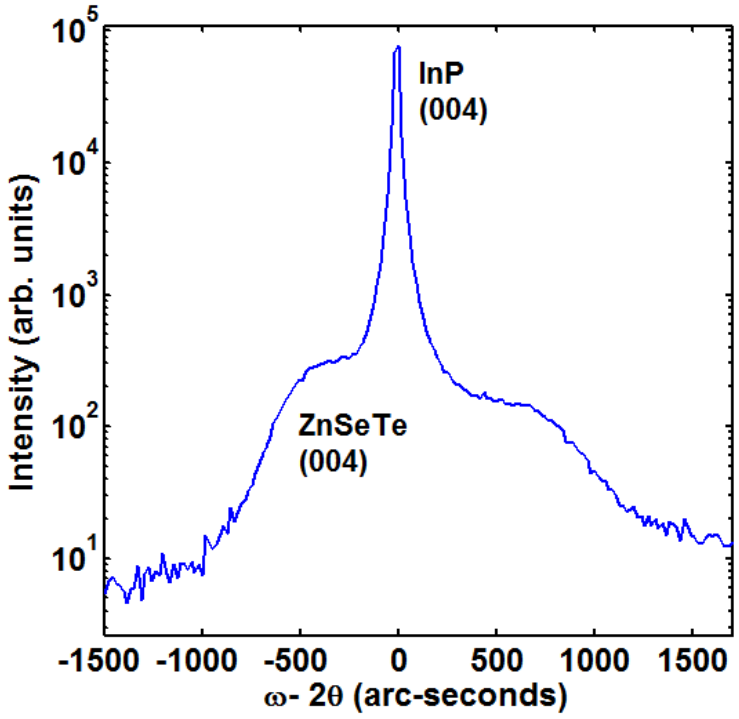

Figure 6.5 X-ray diffraction data in the 004 reflection for ZnSeTe/InP(001), showing the InP substrate peak as well as near lattice features for ZnSeTe film.

Figure 6.6 shows the low temperature photoluminescence (PL) data for the ZnSeTe and ZnSeTeO samples. The ZnSeTe sample has a PL peak at 2.13 eV, which implied 50 % Se fraction[117]. This agrees well with the XRD data in Figure 6.5, since $ZnSe_{0.53}Te_{0.47}$ is lattice matched to InP. For the ZnSeTe material system, the minimum low temperature PL peak is 2.1 eV (at 5 K)[115], as shown in Figure 6.4, which is higher in energy than the ZnSeTeO peak at 1.97 eV in Figure 6.6. This indicates that part of the observed redshift is unaccounted for by changes in ZnSeTe composition, and is likely due to O incorporation.

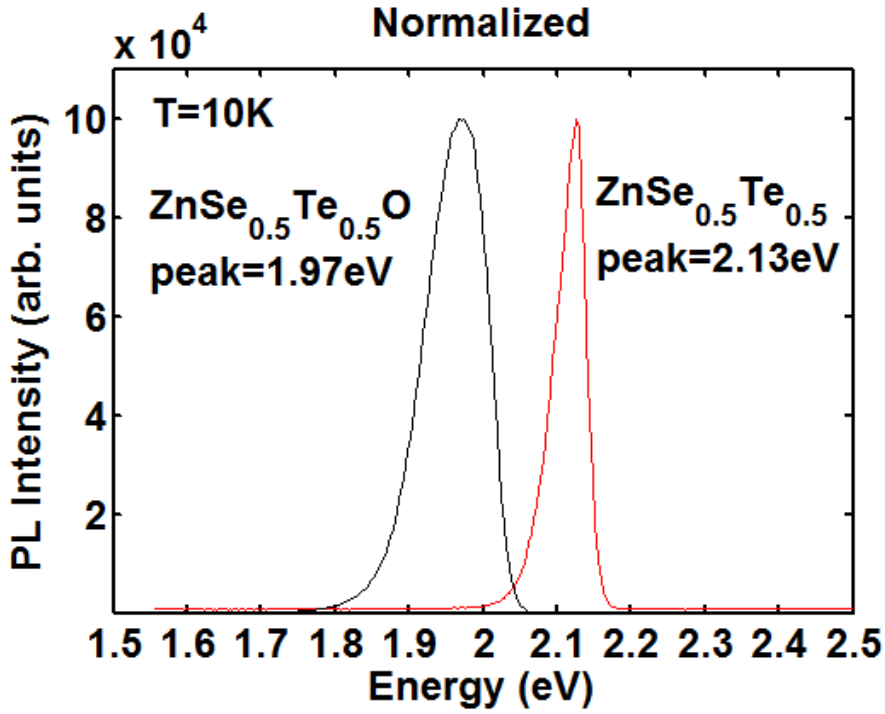

Figure 6.6 Low temperature PL for ZnSeTe and ZnSeTeO, showing redshift as a result of oxygen incorporation. The FWHM of the 1.97 eV and 2.13 eV peaks are 96 meV and 47 meV, respectively.

Temperature dependent PL for the ZnSeTeO sample is shown in Figure 6.7, and Figure 6.8 shows the peak position with respect to temperature for ZnSeTe and ZnSeTeO. As expected, the ZnSeTe peak red shifts with increasing temperature in a manner that can be described by the Varshni relation for semiconductor bandgap as a function of temperature. Also encouraging is that the ZnSeTeO peak also red shifts with increasing temperature in a Varshni like manner, potentially indicating band like behavior for the induced IB.

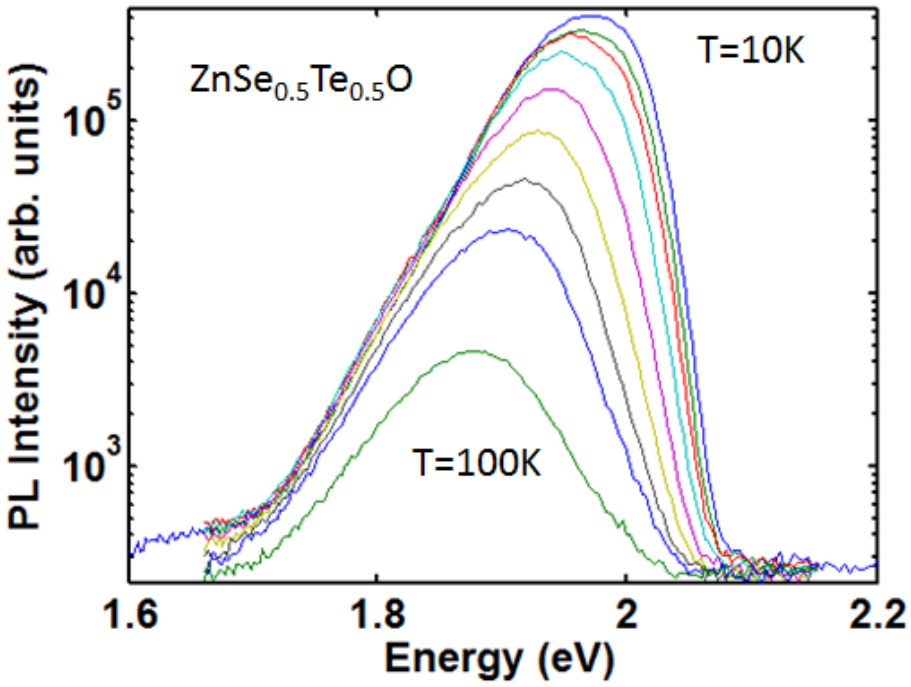

Figure 6.7 Temperature dependent photoluminescence data for the ZnSeTeO sample.

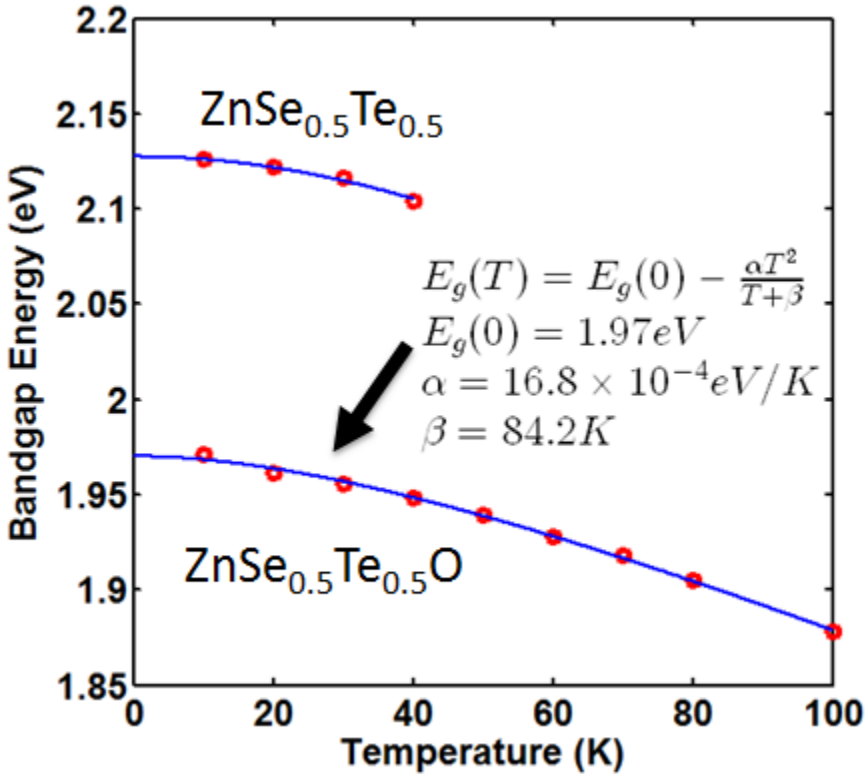

Figure 6.8 Peak energy with respect to temperature for ZnSeTe and ZnSeTeO samples, showing red shift with increasing temperature that may be described by the Varshni relation.

6.2 CdMgTeO

The CdMgTe alloy system is nearly lattice matched throughout the composition range (0.5 % mismatch), as shown in Figure 6.1. Near lattice matching decreases the dislocation densities in growing heterojunctions with different bandgaps. Example applications of such heterojunctions in solar cells include window layer and back-surface field layer. MgTe typically crystalizes in the wurtzite structure. The experimental fit plotted in Figure 6.1 is for Zinc Blende MgTe[118]. As shown in Figure 6.9, the zoomed in experimental fit from [118] shows that $Cd_{0.7}Mg_{0.3}Te$ has a bandgap of approximately 2 eV, which is near ideal for IBSC absorbers. We therefore aim to synthesize $Cd_{0.7}Mg_{0.3}Te$, and then incorporate oxygen to introduce an IB.

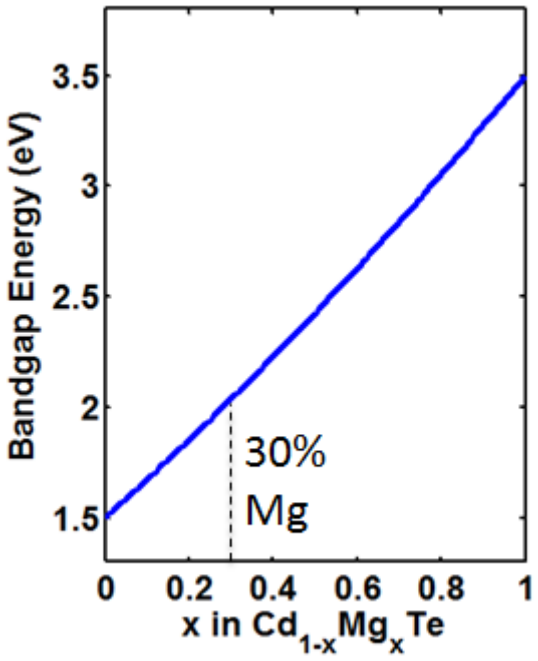

Figure 6.9 [118] Room temperature bandgap energy versus Mg fraction plot for the CdMgTe alloy system, showing a near 2 eV bandgap for 30% Mg fraction.

The materials were synthesized by MBE with solid elemental sources for Mg, Te, and a solid compound source for CdTe. The beam equivalent pressures (BEP) used were

1 x 10^{-6} Torr for Zn, 5 x 10^{-7} Torr for Te, and 2.2 x 10^{-6} Torr for CdTe. Composition was controlled by keeping the Zn, Te, and CdTe fluxes constant and varying the Mg cell temperature. The Mg flux is difficult to measure by ion gauge, potentially due to the small atom size of Mg, making it less likely to ionize. For example, growing CdMgTe with on order of magnitude lower measured Mg flux by ion gauge results in a material that quickly oxides in air to produce a black residue, consistent with MgTe grown by MBE[119].

While there are CdTe and CdZnTe substrates commercially available typically for HgCdTe IR detector applications, these substrates are cost prohibitive. To start, we grow the CdMgTe(O) material on GaAs(100) substrates. As shown in Figure 6.1, CdTe has a large 15 % lattice mismatch to GaAs(100) substrate, which in part leads to CdTe(111) instead of CdTe(100) growth for some experiment conditions[120]. To encourage single crystalline growth in the same orientation as the GaAs(100) substrate, we add a ZnTe (~8 % mismatch from GaAs) buffer to step the lattice mismatch between CdTe and GaAs. The sample structure schematic is shown in Figure 6.10. The CdTe layer between the material of interest CdMgTe and the ZnTe lattice constant buffer helped with the interpretation of PL experiments. Since CdTe (E_G = 1.44 eV) has a smaller bandgap than ZnTe (E_G = 2.3 eV), a sufficiently think CdTe layer would absorb PL emission from the ZnTe layer, so that the detected visible PL is only from the CdMgTe layer of interest.

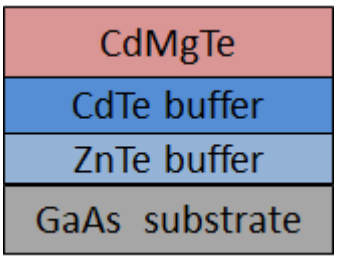

Figure 6.10 Sample structure for the CdMgTe(O) samples, where ZnTe buffer layer was included to grade the large lattice constant mismatch with the GaAs substrate.

The structural properties for samples with structure shown in Figure 6.10 were studied with XRD. Figure 6.11(a) shows the XRD data in the (004) reflection, showing the GaAs substrate peak, the CdTe buffer, as well as a peak for the material of interest. Zooming into the region near the CdMgTe peak, Figure 6.11(b) shows that the CdMgTe peak corresponds to approximately 33 % Mg fraction. Also shown in Figure 6.11(b) are vertical lines indicating that the lattice constant to Mg fraction relation is very steep in this material system, so it is difficult to accurately determine Mg fraction with this XRD data.

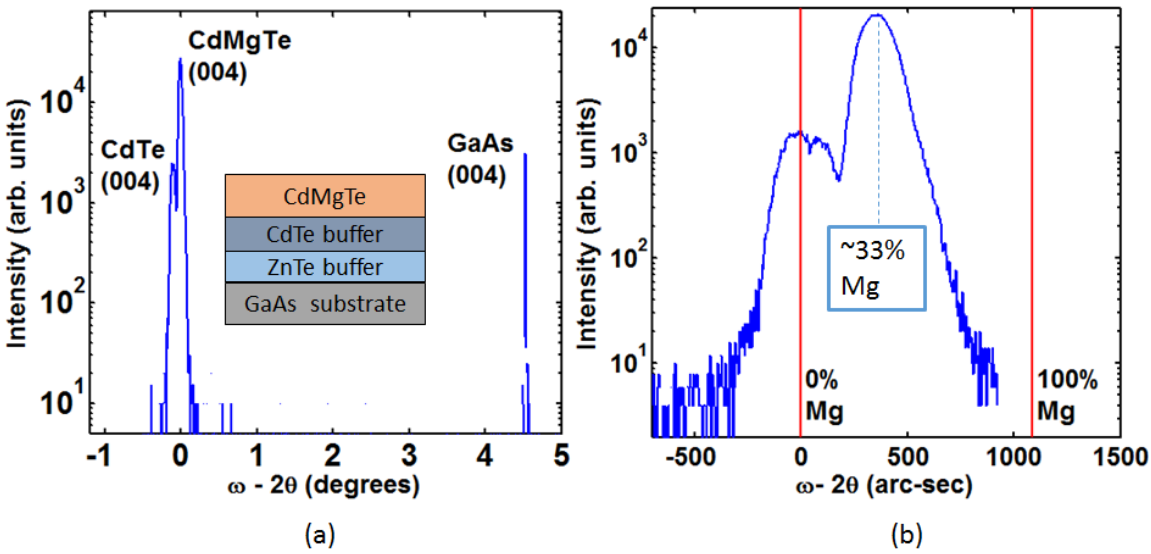

Figure 6.11 X-ray diffraction data of the CdMgTe sample in the 004 reflection. (a) Shows the GaAs substrate peak, the CdTe buffer peak, as well as the CdMgTe peak of interest. (b) Zooms in near the CdMgTe peak,

showing a peak corresponding to approximately 30 % Mg fraction. The red vertical lines show that the lattice constant to Mg fraction relation in the material is very steep.

With ECR O plasma source we achieve approximately 10^{19} cm^{-3} O concentration, as shown by the SIMS data in Figure 6.12. Also shown in Figure 6.12 is an incorporation of $5x10^{17}$ cm^{-3} O concentration for CdMgTe with no intentional oxygen doping. This may indicate that the Mg source may be oxidized. Figure 6.13 shows the XRD data for the sample with intentional O incorporation and the sample without intentional oxygen incorporation. The CdMgTe peaks for both samples are near each other, and are quite broad with respect to the lattice constant to Mg fraction relation in this material system (please see Figure 6.11b). It is difficult to distinguish changes in lattice constant as a result of oxygen incorporation, since the width of the CdMgTe peaks correspond to a 20-30 % difference in Mg fraction.

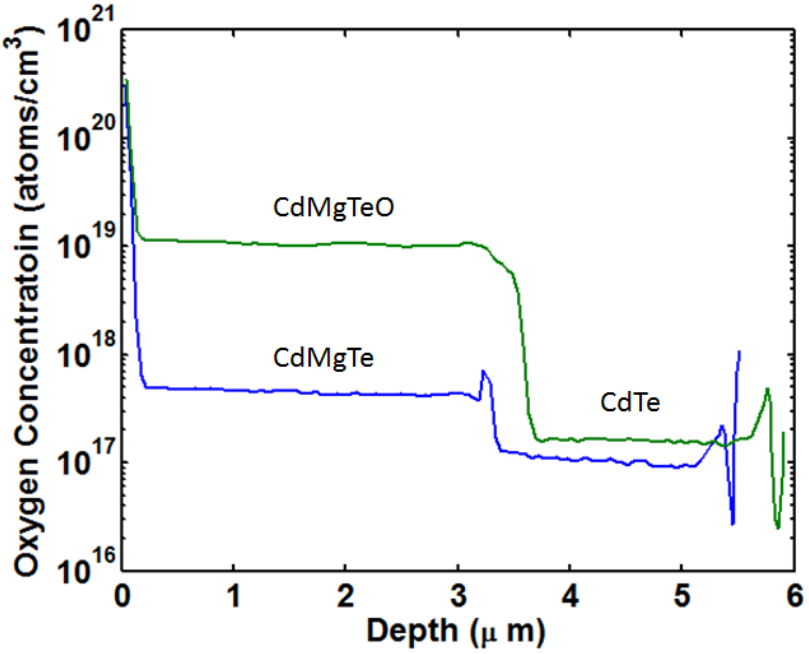

Figure 6.12 Secondary ion mass spectroscopy data for the CdMgTe and CdMgTeO sample, showing approximately 10^{19} cm^{-3} oxygen incorporation for intentionally oxygen doped sample, and $5x10^{17}$ cm^{-3} unintended oxygen incorporation in the CdMgTe sample.

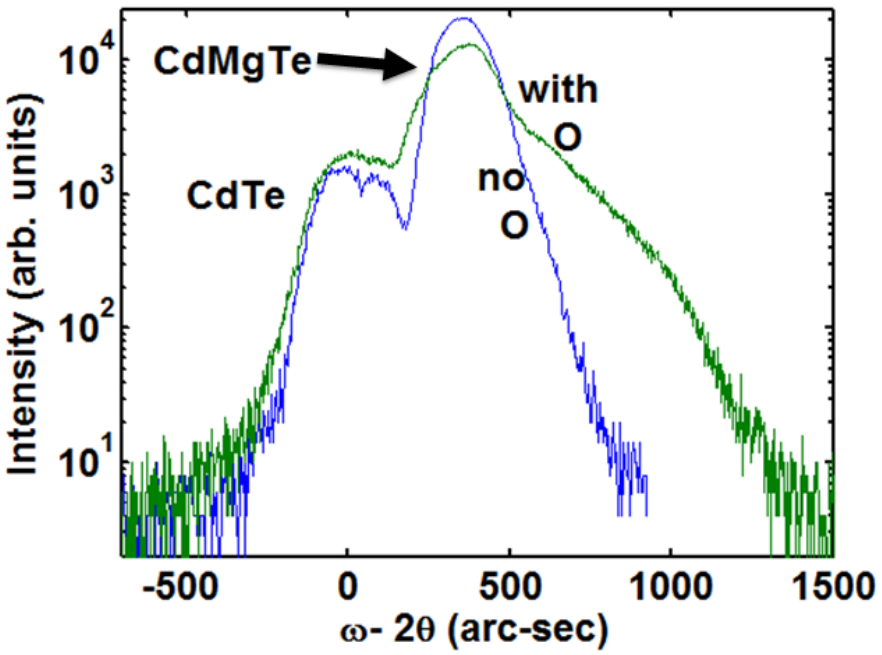

Figure 6.13 X-ray diffraction data for the CdMgTe and CdMgTeO sample in the 004 reflection, showing that both samples have similar peak positions.

The low temperature PL for the CdMgTe sample is plotted in Figure 6.14(left), showing a peak at 2.09 eV and a lower energy peak that may be related to native defects. Figure 6.14(right) plots the low temperature experimental fit from [118], and shows that the 2.09 eV peak corresponds to approximately 27 % Mg fraction, which agrees with the approximately 33% Mg fraction inferred from the XRD data in Figure 6.11(b).

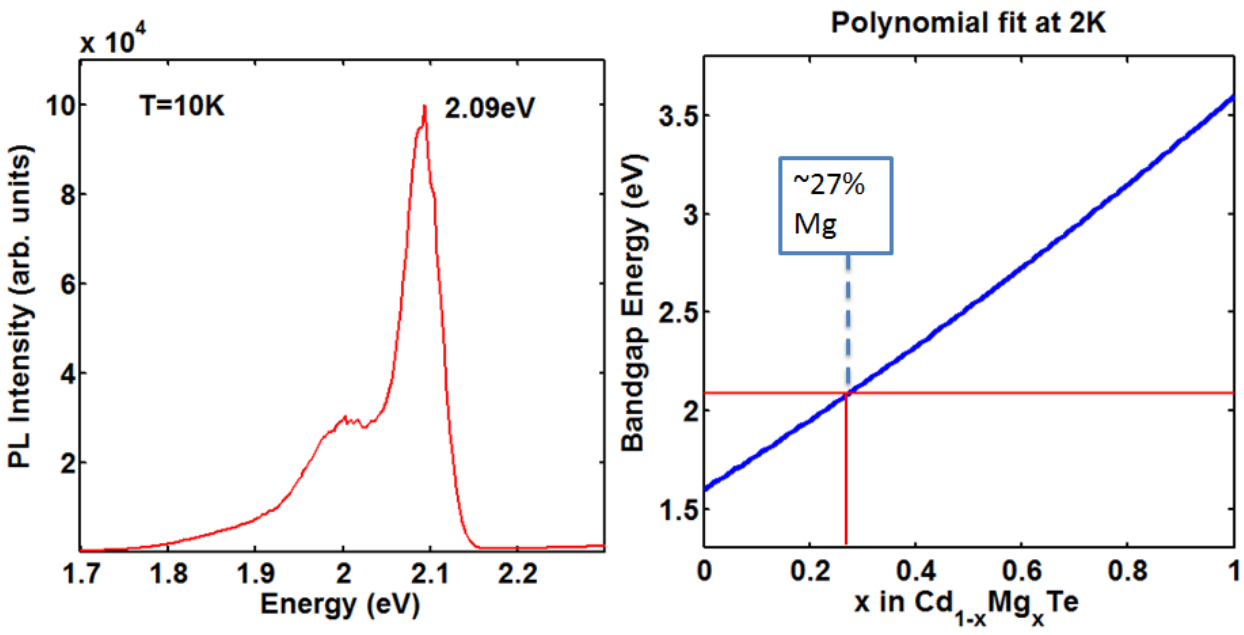

Figure 6.14 (left) Low temperature photoluminescence data for $Cd_{1-x}Mg_xTe$, showing a peak at 2.09 eV. The peak near 2 eV may be due to native defects. The FWHM of the 2.09eV peak is 45meV. (right) shows that the 2.09 eV peak corresponds to approximately x=0.27.

The low temperature PL of the CdMgTeO and CdMgTe samples are plotted in Figure 6.15(left). Oxygen incorporation introduces a red shift from 2.09 eV to 1.96 eV, however, it is not clear if this red shift is actually related to oxygen. As shown in Figure 6.15(right), a 7 % reduction in Mg fraction can also account for this redshift, and because the XRD peaks in Figure 6.13 are broad enough to mask a 7 % change in Mg fraction, the source of that PL redshift is inconclusive. To try to understand the role of oxygen in the electronic structure of this material, we performed temperature dependent PL.

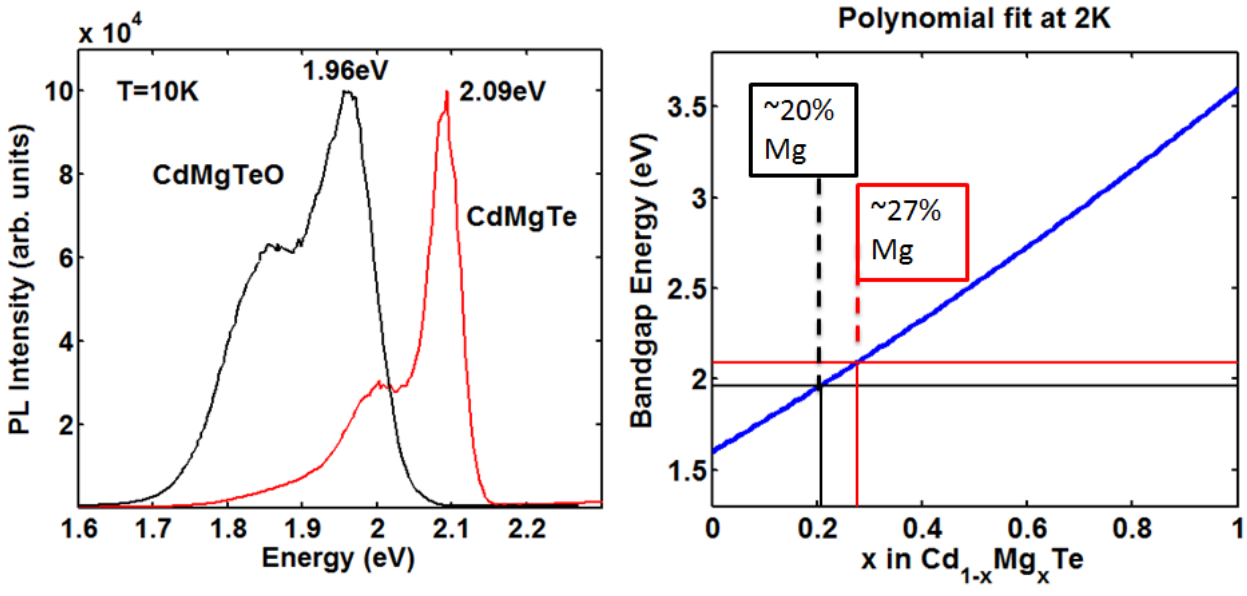

Figure 6.15 (left) Low temperature luminescence data for CdMgTe and CdMgTeO samples, showing a peak redshift from 2.09 eV to 1.96 eV as a result of oxygen doping. The FWHM of the 2.09 eV peak is 45 meV, and that for the 1.96 eV feature is 185 meV. (right) Polynomial fit for low temperature bandgap of Mg fraction shows that a 7 % change in Mg fraction can account for the observed redshift in photoluminescence.

Figure 6.16 plots the temperature dependent PL for the CdMgTe and CdMgTeO samples in log scale. There appears a to be similar set of three peaks near 1.85 eV, 1.95 eV, and 2.05 eV for the CgMgTe and CdMgTeO samples, and the effect of increased oxygen incorporation seems to be to increase the relative intensity of the two lower energy peaks with respect to the higher energy one. We speculate that the 1.85 eV and 1.95 eV peaks may be related to oxygen, and that those peaks are present in the CdMgTe sample because of unintentional oxygen incorporation during growth, as shown in Figure 6.12.

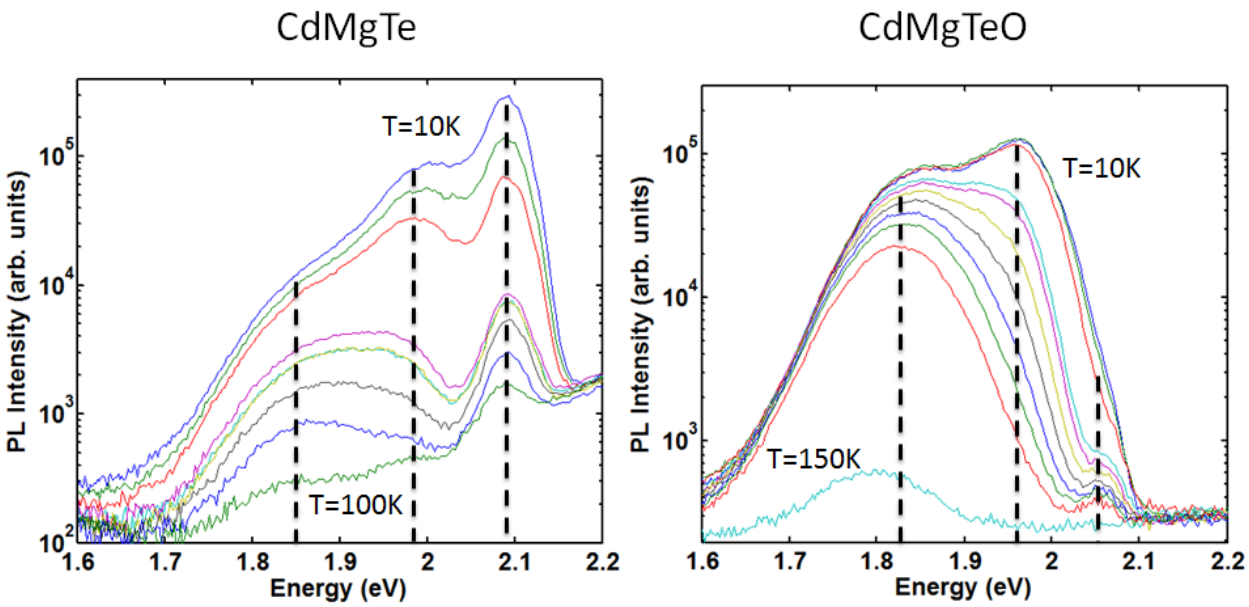

Figure 6.16 Temperature dependent PL for CdMgTe and CdMgTeO samples plotted in log scale, showing a similar set of three peaks.

6.3 CdZnTeO

Figure 6.1 shows that at about 30 % Cd fraction, the CdZnTe (CZT) material system is near 2 eV bandgap, which is ideal for IBSC application.

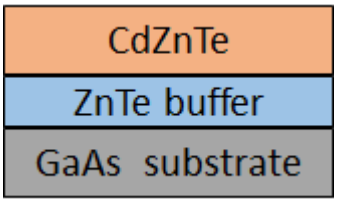

Figure 6.17 Sample structure for used to synthesize CdZnTe film on GaAs substrate.

The materials were synthesized by MBE on GaAs(100) substrates. Since CdTe is 15 % lattice mismatched from GaAs(100) substrate (as shown in Figure 6.1), we use a thin ZnTe buffer to step the lattice constant to 8 % lattice mismatch from the substrate, as shown in Figure 6.17. The Zn flux was $1x10^{-6}$ Torr, Te flux was $1x10^{-6}$ Torr, and the

CdTe flux was varied to control the CdZnTe composition. An ECR plasma source was used to introduce oxygen and nitrogen plasma to the substrate surface. For the sample with oxygen and nitrogen co-doping,

The structural properties of the film were studied by XRD. Figure 6.18 shows the XRD data of the CZT and CZTO films in the (004) reflection for film structures outlined in Figure 6.17. The data shows the GaAs substrate peak, a weak peak corresponding to the ZnTe buffer, and CZT(O) peaks. As the CZTO peak is closer to the peak compared to the CZT peak, this data suggests that the CZTO sample has higher Zn content, and therefore large bandgap compared to the CZT sample.

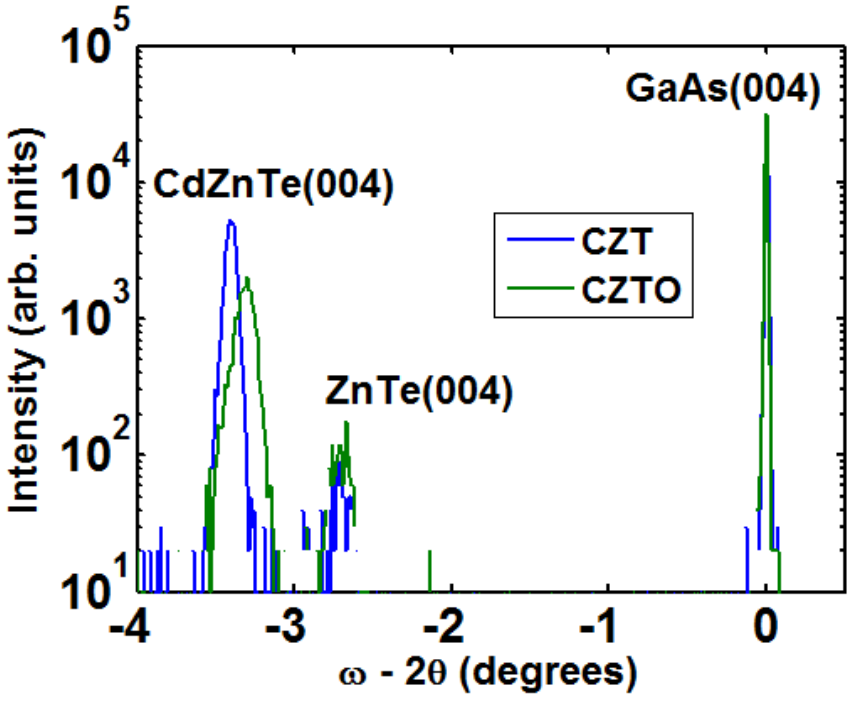

Figure 6.18 X-ray diffraction data in the (004) reflection showing the GaAs(100) substrate peak, the ZnTe buffer peak, and well as the CdZnTe(O) peak.

The low temperature PL is plotted in Figure 6.19. From the XRD data in Figure 6.18 we would expect the bandgap of the CZTO sample to be larger, yet the PL data in

Figure 6.19 shows that the CZTO sample emits at a lower energy, suggesting that the redshift is related to oxygen and not related to changes in CZT composition. From the XRD data in Figure 6.18 we expect a bandgap of approximately 2 eV for the CZT and CZTO samples. For the CZT sample, the peak near 2.05 eV is likely the band edge emission, the peak near 1.94 eV peak may be related to native defects, and the peak near 2.35 eV is related to the green pump laser for the Ti:Sapphire pulsed laser system. We also see some broad spectral features at lower energy than the 1.94eV peak that seems to overlap with the spectrum of the CZTO sample, potentially originating from an oxidized top surface of the CZT sample. This leads to the interpretation that the 1.94eV peak may be a generic defect like the so called Y-band[89, 91, 92] in the ZnTeO system, where the Y band is similarly situated between the O related signal and the band edge. For the CZTO sample, we do not see the band edge emission, potentially because the oxygen localized defect is efficient in capturing the free excitons at low temperature.

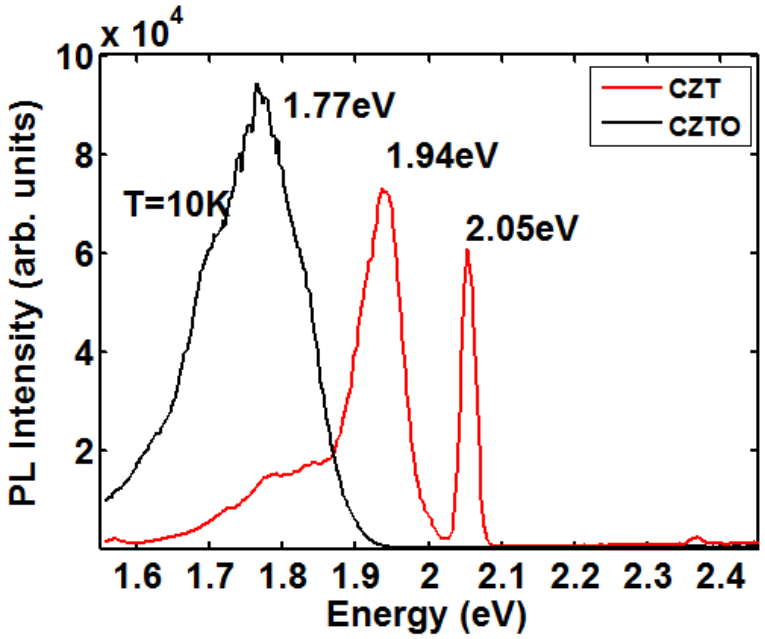

Figure 6.19 Low temperature photoluminescence data for the CdZnTe and CdZnTe samples, showing a peak redshift from 2.05 eV to 1.77 eV as a result of oxygen incorporation. The FWHM of the 1.77eV, 1.94eV, 2.05eV peaks are 162 meV, 72 meV, 24 meV, respectively.

To help make the band edge states visible, we introduce nitrogen into the sample. Nitrogen atoms form acceptor states in CZT[121]. The acceptor states are localized, and may compete with O atoms in capturing the free excitons. While not true representation of the band edge emission, the shallow acceptor states may follow temperature dependent behavior of the band edge closely, by virtue of being close to the band edge. The temperature dependent PL data for sample co-doped with nitrogen and oxygen (CZT:N,O) is shown in Figure 6.20. The peak near 2.2 eV is likely from the N acceptor near the valence band, and its energy is expected to be close to the bandgap of the material. This interpretation also agrees with reflectance data in Figure 6.21 that shows a disappearance of reflection interference fringes for wavelengths shorter than 560 nm (2.2 eV), indicating significant absorption typical for above bandgap light. The N acceptor peak red shifts with increasing temperature, and may be due to the temperature dependent

bandgap effect described by the Varshni relation. The peak near 1.75 eV is likely related to oxygen, potentially the E^- band described by the HMA model.

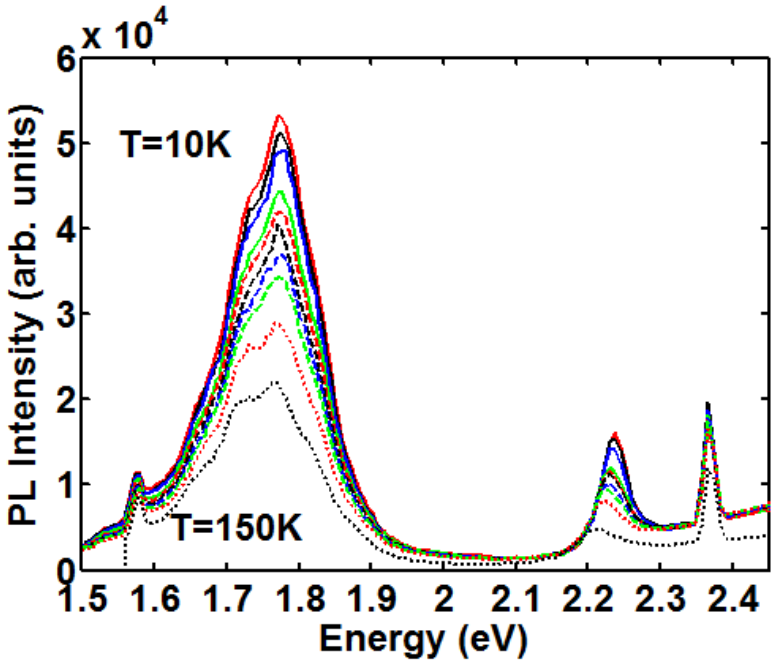

Figure 6.20 Temperature dependent photoluminescence data for CdZnTe:O,N.

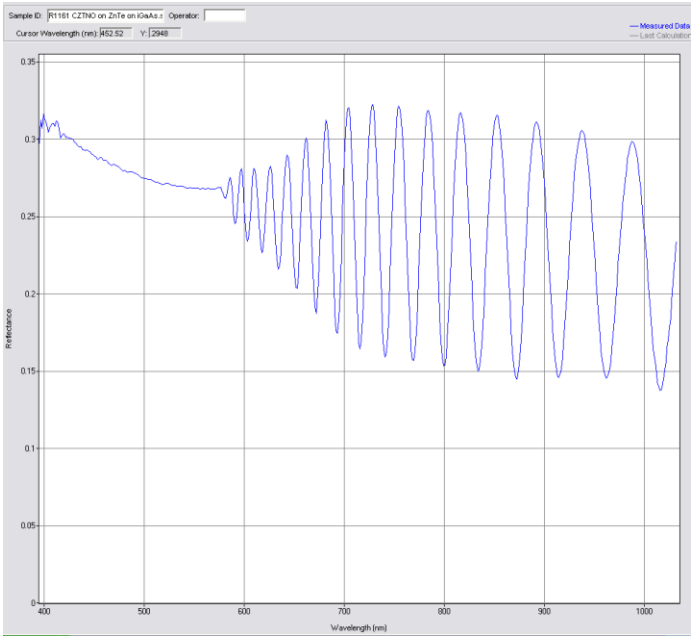

Figure 6.21 Reflectance data of CZT:NO. The disappearance of reflection interference fringes for wavelengths shorter than 560 nm (2.2 eV) indicates significant absorption typical for above bandgap light.

6.4 Conclusions

IBSCs have an ideal bandgap of 1.93 eV, and a IB that is 0.7 eV from the CB or VB[11]. This Chapter explored using II-VI ternary alloys of ZnSeTe, CdMgTe, and CdZnTe to achieve near ideal IBSC bandgap, and attempt to induce and IB through the HMA affect by isoelectronic dilute alloying with oxygen. In ZnSeTeO and CdZnTeO, oxygen induced IB was detected by low temperature PL, where as in CdMgTeO, oxygen incorporation was confirmed by SIMS, but it was not clear from PL and XRD data if an oxygen induced IB was formed. Table 6-1 summarizes some properties and results of the preliminary studies done on ZnSeTe(O), CdMgTe(O), and CdZnTe(O) II-VI ternary alloys. This work shows that using II-VI-O alloys to achieve near ideal IBSC energy levels may be possible, and may be a promising area for future research to realize high efficiency IBSCs.

Table 6-1. Summary of some properties and findings of the ternary II-VI alloy systems studied in this Chapter.

	ZnSeTe(O)	CdMgTe(O)	CdZnTe(O)
O related reshift?	yes	Don't know	Yes
O level wrt CB	below	Near resonant	Near resonant
Mixed group II or VI?	Group VI	Group II	Group II
Phase transition?	no	Wurtzite/zinc blende	no
2 eV bandgap synthesized?	yes	yes	yes

Chapter 7
Conclusions and Future Work

7.1 Summary of Thesis Work

This thesis work studied the material properties of a highly mismatched alloy ZnTeO in detail in the context of potentially being used as an IBSC absorber. Optical and chemical properties of the ZnTeO/GaAs material showed that the electronic structure of the oxygen induced energy levels are influenced by oxygen location in the crystal lattice, which can be influenced by oxygen plasma back ground pressure used during material synthesis. The non-monotonic ZnTe peak shift in the XRD data with respect to increasing O beam equivalent pressure (BEP) similarly suggests different oxygen configuration in the crystal with different O BEP during growth. Secondary Ion Mass Spectroscopy and Nuclear Reaction Analysis (NRA) data shows that the oxygen incorporation is approximately for the materials are approximately 10^{20} cm^{-3}. NRA channeling data, if analyzed assuming a homogeneous film, suggests that only a small fraction (~5%) of the oxygen is in the substitutional Te site. However, the highly non-homogeneous nature of the film potentially invalidates this interpretation.

A novel two pump time resolved photoluminescence was used to observe the time resolved electron transfer from the VB to IB, and then from IB to CB with two sub-bandgap pules, confirming the IBSC device requirement that carriers be generated via

sub-bandgap light. The data also revealed picosecond scale lifetime relaxation from CB through non-radiative channels, which implies a collection length of 10's of nanometers, which is insufficient to absorb the solar photon flux, and is a challenge for this material system.

Solar cell devices with p-i-n heterostructure structure were synthesized with p type ZnTe:N, undoped ZnTeO, and n type ZnSe:Cl. External quantum efficiency (EQE) measurements confirmed sub-bandgap EQE response for a sample with oxygen doped absorber, and confirmed that that such a sub-bandgap response was absent from a device with no intentional oxygen doping in the absorber. Similarly, I-V measurements show photocurrent generation as a result of sub-bandgap red laser illumination for a sample with an intentionally O doped absorber, but not for a sample with no intentional O doped absorber. These results confirm sub-bandgap current generation, an important requirement for the operation of IBSCs.

A novel way to prepare GaSb(100) substrate for ZnTe epitaxy was developed to enable near lattice matched growth of ZnTeO on GaSb(100). The technique involves an ex-situ HCl native oxide etch prior to loading, and an in-situ $ZnCl_2$ flux exposure during the thermal oxide removal heat up step. It is believed that the $ZnCl_2$ flux helps etch the surface oxide, so that complete oxide removal could be achieved at a lower temperature of 430 ^{o}C, at which the Sb does not preferentially desorb of the surface. This allows us to synthesize ZnTe/GaSb(100) with (004) film peak in XRD data with a FWHM of 40 arc-seconds, without the need to use an interconnected III-V chamber for the substrate preparation. The improved ZnTeO film quality enhanced IBSC device performance, and aided in the observation of time resolved electron population transfer from the IB to CB.

7.2 Suggestions for Future Work

Ternary II-VI alloys of ZnSeTe, CdMgTe, and CdZnTe with bandgaps of approximately 2 eV, near the ideal bandgap for IBSCs were synthesized. Oxygen was then introduced during synthesis to form sub-bandgap electronic states for use as IB. O related sub-bandgap states were confirmed for ZnSeTe and CdZnTe. For CdMgTe, SIMS confirmed O concentration of approximately 1 x 10^{19} cm^{-3} incorporation, but the PL and XRD data was not conclusive in determining if O induced sub-bandgap electronic states were generated. These results show that the II-VI-O materials may be promising candidates for IBSC absorber material development. Suggestions for Future Work

With regards to ZnTeO material system, the IB ideally should be approximately 0.8 eV away from the band edge, as shown Figure 1.24. Our ZnTeO materials have an IB that is 0.4 eV beneath the conduction band. One way to achieve a deeper IB is to increase the oxygen concentration. For example, approximately 0.85 eV deep IB was reported with O concentration of 1.09 %[88]. One potential way to achieve higher oxygen concentration may be to upgrade the ECR plasma source. At the moment the plasma source head is approximately 15 cm behind the cryoshroud opening of the MBE due to size non-compatibility, significantly reducing the plasma source doping efficiency.

This thesis work confirmed that electronic structure is correlated to O location in the crystal. While NRA-channeling data was taken, the interpretation of the data was made difficult by the highly non-uniform nature of the film. It would be desirable to repeat the NRA-channeling experiments with a surface oxide etch immediately prior to loading into the experiment chamber to produce a more uniform film. More studies into the influence of O location or clustering configuration on carrier transport and electronic

structure properties, such as work found in [74-76] would be useful in the understanding and control of the properties of ZnTeO.

The lifetime data on ZnTeO revealed that the carrier lifetime in the CB is in the picosecond time scale, mainly due to non-radiative recombination. The chlorine doping of ZnTeO improved the open circuit voltage of some IBSC devices, suggesting that chlorine may be passivating the ZnTeO material. Lifetime data comparing ZnTeO with and without chlorine doping is needed to test this hypothesis, and it would also be interesting to look into other ways to passivate the ZnTeO material.

One of the major limitations of our ZnSe/ZnTe heterojunctions solar cell technology is the large lattice mismatch between ZnSe and ZnTe, leading to high defect densities. One way to improve the junction is to synthesize a ZnTe homo junction instead. n-type ZnTe has been demonstrated by Al doping during MBE growth[43] and by Al diffusion[46] in the literature. Our system can potentially be upgraded with an Al effusion cell to synthesize n-ZnTe.

The O-doped II-VI ternary alloys of CdMgTe(O) and CdZnTe(O) are potentially promising candidates for IBSC absorbers. It would be interesting to replicate similar work presented in this thesis done for ZnTeO on these ternary alloys.

References

[1] J. Wu, W. Walukiewicz, and E. E. Haller, "Band structure of highly mismatched semiconductor alloys: Coherent potential approximation," *Physical Review B,* vol. 65, Jun 2002.

[2] Intergovernmental-Panel-on-Climate-Change, *Climate Change 2013, The Physical Science Basis, Working Group I Contribution to the Fifth Assessment Report of the Intergovernmental Panel on Climate Change*: Cambridge University Press, 2013.

[3] German-Advisory-Council-on-Global-Change, *Flagship Report, World in Transition, A Social Contract for Sustainability*, 2011.

[4] United-States-Department-of-Energy-National-Renewable-Energy-Laboratory, *SunShot Vision Study*, 2012.

[5] P. J. McElheny, J. K. Arch, H. S. Lin, and S. J. Fonash, "RANGE OF VALIDITY OF THE SURFACE-PHOTOVOLTAGE DIFFUSION LENGTH MEASUREMENT - A COMPUTER-SIMULATION," *Journal of Applied Physics,* vol. 64, pp. 1254-1265, Aug 1988.

[6] W. Shockley and H. J. Queisser, "DETAILED BALANCE LIMIT OF EFFICIENCY OF P-N JUNCTION SOLAR CELLS," *Journal of Applied Physics,* vol. 32, pp. 510-&, 1961.

[7] M. A. Green, "Third generation photovoltaics: Ultra-high conversion efficiency at low cost," *Progress in Photovoltaics,* vol. 9, pp. 123-135, Mar-Apr 2001.

[8] J. Nelson, *The Physics of Solar Cells*. London: Imperial College Press, 2003.

[9] G. L. Araujo and A. Marti, "ABSOLUTE LIMITING EFFICIENCIES FOR PHOTOVOLTAIC ENERGY-CONVERSION," *Solar Energy Materials and Solar Cells,* vol. 33, pp. 213-240, Jun 1994.

[10] J. Merten, J. M. Asensi, C. Voz, A. V. Shah, R. Platz, and J. Andreu, "Improved equivalent circuit and analytical model for amorphous silicon solar cells and modules," *Ieee Transactions on Electron Devices,* vol. 45, pp. 423-429, Feb 1998.

[11] A. Luque and A. Marti, "Increasing the efficiency of ideal solar cells by photon induced transitions at intermediate levels," *Physical Review Letters,* vol. 78, pp. 5014-5017, Jun 30 1997.

[12] D. Konig, K. Casalenuovo, Y. Takeda, G. Conibeer, J. F. Guillemoles, R. Patterson*, et al.*, "Hot carrier solar cells: Principles, materials and design," *Physica E-Low-Dimensional Systems & Nanostructures,* vol. 42, pp. 2862-2866, Sep 2010.

[13] A. Luque and A. Marti, "The Intermediate Band Solar Cell: Progress Toward the Realization of an Attractive Concept," *Advanced Materials,* vol. 22, pp. 160-174, Jan 2010.

[14] A. Lin and J. Phillips, "Resolving spectral overlap issue of intermediate band solar cells using non-uniform sub-bandgap state filling," *Progress in Photovoltaics,* vol. 22, pp. 1062-1069, Oct 2014.

[15] A. Luque, A. Marti, E. Antolin, and C. Tablero, "Intermediate bands versus levels in non-radiative recombination," *Physica B-Condensed Matter,* vol. 382, pp. 320-327, Jun 2006.

[16] J. J. Krich, B. I. Halperin, and A. Aspuru-Guzik, "Nonradiative lifetimes in intermediate band photovoltaics-Absence of lifetime recovery," *Journal of Applied Physics,* vol. 112, Jul 2012.

[17] K. Nakano and A. Ishibashi, "Long lived widegap II-VI lasers," in *Properties of Wide Bandgap II-VI Semiconductors*, R. Bhargava, Ed., ed London, United Kingdom: INSPEC, The Institution of Electrical Engineers, 1996, p. 191.

[18] K. Nakano, "Blue-Green Semiconductor Lasers," in *II-VI Semiconductor Materials and Their Applications*. vol. 12, M. C. Tamargo, Ed., ed New York, New York: Taylor & Francis, 2002, p. 52.

[19] D. Edwall and J. Bajaj, "HgCdTe Growth and Detector Technology," in *II-VI Semiconductor Materials and Their Applications*. vol. 12, M. C. Tamargo, Ed., ed New York, New York: Taylor & Francis Inc., 2002, pp. 1-30.

[20] K. Alavi, "Molecular Beam Epitaxy," in *Handbook of Compound Semiconductors: Growth, Processing, Characterization and Devices*, *G. E. M. Paul H. Holloway*, Ed., ed: William Andrew, 1996, pp. 84-169.

[21] L. Q. Zhou, C. Y. Chen, H. F. Jia, C. Ling, D. Banerjee, J. D. Phillips*, et al.*, "Oxygen Incorporation in ZnTeO Alloys via Molecular Beam Epitaxy," *Journal of Electronic Materials,* vol. 43, pp. 889-893, Apr 2014.

[22] T. Yao, "Molecular Beam Epitaxy of Wide Gap II-VI Compounds," in *II-VI Semiconductor Materials and Their Applications*. vol. 12, M. C. Tamargo, Ed., ed New York, New York: Taylor & Francis Inc., 2002, p. 67.

[23] G. Horsburgh, K. A. Prior, W. Meredith, I. Galbraith, B. C. Cavenett, C. R. Whitehouse*, et al.*, "Topography measurements of the critical thickness of ZnSe grown on GaAs," *Applied Physics Letters,* vol. 72, pp. 3148-3150, Jun 1998.

[24] H. Preis, T. Frey, T. Reisinger, and W. Gebhardt, "TEM-investigation on the critical thickness anisotropy of MBE-grown ZnSe/GaAs and Zn1-xMgxSe/GaAs," *Journal of Crystal Growth,* vol. 184, pp. 85-89, Feb 1998.

[25] N. Chand, "MBE GROWTH OF HIGH-QUALITY GAAS," *Journal of Crystal Growth,* vol. 97, pp. 415-429, Sep 1989.

[26] J. H. Neave, B. A. Joyce, P. J. Dobson, and N. Norton, "DYNAMICS OF FILM GROWTH OF GAAS BY MBE FROM RHEED OBSERVATIONS," *Applied Physics a-Materials Science & Processing,* vol. 31, pp. 1-8, 1983.

[27] J. E. Ayers, "THE MEASUREMENT OF THREADING DISLOCATION DENSITIES IN SEMICONDUCTOR CRYSTALS BY X-RAY-DIFFRACTION," *Journal of Crystal Growth,* vol. 135, pp. 71-77, Jan 1994.

[28] M. E. Constantino, M. A. Vidal, B. Salazar-Hernandez, H. Navarro-Contreras, M. Lopez-Lopez, M. Melendez*, et al.*, "Dislocation densities in MBE grown ZnSe epitaxial layers on GaAs by HRXRD," *Journal of Crystal Growth,* vol. 194, pp. 301-308, Dec 1998.

[29] J. E. Ayers, "NEW MODEL FOR THE THICKNESS AND MISMATCH DEPENDENCIES OF THREADING DISLOCATION DENSITIES IN MISMATCHED HETEROEPITAXIAL LAYERS," *Journal of Applied Physics,* vol. 78, pp. 3724-3726, Sep 1995.

[30] K. Kimura, S. Miwa, T. Yasuda, L. H. Kuo, A. Ohtake, C. G. Jin*, et al.*, "Molecular beam epitaxial growth of P-ZnSe:N using a novel plasma source," *Journal of Electronic Materials,* vol. 26, pp. 705-709, Jun 1997.

[31] G. Mandel, "SELF-COMPENSATION LIMITED CONDUCTIVITY IN BINARY SEMICONDUCTORS .1. THEORY," *Physical Review a-General Physics,* vol. 134, pp. 1073-&, 1964.

[32] D. B. Laks, C. G. Van De Walle, G. F. Neumark, P. E. Blochl, and S. T. Pantelides, "NATIVE DEFECTS AND SELF-COMPENSATION IN ZNSE," *Physical Review B,* vol. 45, pp. 10965-10978, May 1992.

[33] I. S. Hauksson, J. Simpson, S. Y. Wang, K. A. Prior, and B. C. Cavenett, "COMPENSATION PROCESSES IN NITROGEN DOPED ZNSE," *Applied Physics Letters,* vol. 61, pp. 2208-2210, Nov 1992.

[34] A. Garcia and J. E. Northrup, "COMPENSATION OF P-TYPE DOPING IN ZNSE - THE ROLE OF IMPURITY-NATIVE DEFECT COMPLEXES," *Physical Review Letters,* vol. 74, pp. 1131-1134, Feb 1995.

[35] D. J. Chadi and N. Troullier, "SELF-COMPENSATION IN NITROGEN-DOPED ZNSE," *Physica B,* vol. 185, pp. 128-131, Apr 1993.

[36] T. Yao, T. Matsumoto, S. Sasaki, C. K. Chung, Z. Zhu, and F. Nishiyama, "LATTICE LOCATION OF N ATOMS IN HEAVILY N-DOPED ZNSE STUDIED WITH ION-BEAMS ANALYSIS AND ITS IMPLICATION ON DEEP-LEVEL DEFECTS," *Journal of Crystal Growth,* vol. 138, pp. 290-294, Apr 1994.

[37] B. H. Cheong, C. H. Park, and K. J. Chang, "FIRST-PRINCIPLES STUDY OF THE COMPENSATION MECHANISM FOR NITROGEN ACCEPTORS IN ZNSE," *Physical Review B,* vol. 51, pp. 10610-10614, Apr 1995.

[38] D. J. Chadi, "COLUMN-V ACCEPTORS IN ZNSE - THEORY AND EXPERIMENT," *Applied Physics Letters,* vol. 59, pp. 3589-3591, Dec 1991.

[39] C. H. Park and D. J. Chadi, "BULK LATTICE INSTABILITY IN II-VI SEMICONDUCTORS AND ITS EFFECT ON IMPURITY COMPENSATION," *Physical Review Letters,* vol. 75, pp. 1134-1137, Aug 1995.

[40] D. B. Laks, C. G. Van De Walle, G. F. Neumark, and S. T. Pantelides, "ACCEPTOR DOPING IN ZNSE VERSUS ZNTE," *Applied Physics Letters,* vol. 63, pp. 1375-1377, Sep 1993.

[41] P. M. Mensz, S. Herko, K. W. Haberern, J. Gaines, and C. Ponzoni, "ELECTRICAL CHARACTERIZATION OF P-TYPE ZNSE-N AND ZN1-XMGXSYSE1-Y-N THIN-FILMS," *Applied Physics Letters,* vol. 63, pp. 2800-2802, Nov 1993.

[42] J. Han, Y. Fan, M. D. Ringle, L. He, D. C. Grillo, R. L. Gunshor*, et al.*, "OHMIC CONTACTS AND TRANSPORT-PROPERTIES IN ZNSE-BASED HETEROSTRUCTURES," *Journal of Crystal Growth,* vol. 138, pp. 464-470, Apr 1994.

[43] J. H. Chang, T. Takai, B. H. Koo, J. S. Song, T. Handa, and T. Yao, "Aluminum-doped n-type ZnTe layers grown by molecular-beam epitaxy," *Applied Physics Letters,* vol. 79, pp. 785-787, Aug 2001.

[44] M. Hanafusa, K. Sato, A. Noda, A. Arakawa, Y. Matsuda, and O. Oda, "Diffusion properties of Al in ZnTe substrates," *Journal of Applied Physics,* vol. 89, pp. 1989-1990, Feb 2001.

[45] T. Tanaka, K. Hayashida, K. Saito, M. Nishio, Q. Guo, and H. Ogawa, "Effect of surface treatment on properties of ZnTe LED fabricated by Al thermal diffusion," *Physica Status Solidi B-Basic Solid State Physics,* vol. 243, pp. 959-962, Mar 2006.

[46] T. Tanaka, K. Saito, M. Nishio, Q. X. Guo, and H. Ogawa, "Fabrication of a ZnTe light emitting diode by Al thermal diffusion into a p-ZnTe epitaxial layer on a p-ZnMgTe substrate," *Journal of Materials Science-Materials in Electronics,* vol. 20, pp. 505-509, Jan 2009.

[47] M. J. DiNezza, Q. Zhang, D. Ding, J. Fan, X. Y. Liu, J. K. Furdyna*, et al.*, "Aluminum diffusion in ZnTe films grown on GaSb substrates for n-type doping," *Physica Status Solidi C: Current Topics in Solid State Physics, Vol 9, No 8-9,* vol. 9, pp. 1720-1723, 2012.

[48] J. Fan, L. Ouyang, X. Liu, D. Ding, J. K. Furdyna, D. J. Smith*, et al.*, "Growth and material properties of ZnTe on GaAs, InP, InAs and GaSb (001) substrates for electronic and optoelectronic device applications," *Journal of Crystal Growth,* vol. 323, May 15 2011.

[49] C. J. Vineis, C. A. Wang, and K. F. Jensen, "In-situ reflectance monitoring of GaSb substrate oxide desorption," *Journal of Crystal Growth,* vol. 225, May 2001.

[50] S. Wang, D. Ding, X. Liu, X. B. Zhang, D. J. Smith, J. K. Furdyna*, et al.*, "MBE growth of II-VI materials on GaSb substrates for photovoltaic applications," *Journal of Crystal Growth,* vol. 311, pp. 2116-2119, Mar 2009.

[51] E. Weiss, O. Klin, S. Grossman, S. Greenberg, P. C. Klipstein, R. Akhvlediani*, et al.*, "Hydrogen and thermal deoxidations of InSb and GaSb substrates for molecular beam epitaxial growth," *Journal of Vacuum Science & Technology A,* vol. 25, pp. 736-745, Jul-Aug 2007.

[52] K.-K. Lee, K. Doyle, J. Chai, J. H. Dinan, and T. H. Myers, "X-Ray Photoelectron Spectroscopy Study of Oxide Removal Using Atomic Hydrogen for Large-Area II-VI Material Growth," *Journal of Electronic Materials,* vol. 41, pp. 2799-2809, Oct 2012.

[53] G. R. Bell and C. F. McConville, "Atomic hydrogen cleaning of GaSb(001) surfaces," *Applied Physics Letters,* vol. 69, pp. 2695-2697, Oct 28 1996.

[54] Z. Lu, Y. Jiang, W. I. Wang, M. C. Teich, and R. M. Osgood, "GASB-OXIDE REMOVAL AND SURFACE PASSIVATION USING AN ELECTRON-CYCLOTRON RESONANCE HYDROGEN SOURCE," *Journal of Vacuum Science & Technology B,* vol. 10, pp. 1856-1861, Jul-Aug 1992.

[55] D. Hommel, S. Scholl, T. A. Kuhn, W. Ossau, A. Waag, G. Landwehr*, et al.*, "EFFICIENT N-TYPE DOPING OF CDTE EPITAXIAL LAYERS GROWN BY PHOTO-ASSISTED MOLECULAR-BEAM EPITAXY WITH THE USE OF CHLORINE," *Materials Science and Engineering B-Solid State Materials for Advanced Technology,* vol. 16, pp. 178-181, Jan 1993.

[56] D. Hommel, A. Waag, S. Scholl, and G. Landwehr, "CHLORINE - A NEW EFFICIENT NORMAL-TYPE DOPANT IN CDTE LAYERS GROWN BY MOLECULAR-BEAM EPITAXY," *Applied Physics Letters,* vol. 61, pp. 1546-1548, Sep 1992.

[57] W. Lin, A. Cavus, L. Zeng, and M. C. Tamargo, "N-type doping of lattice-matched ZnCdSe and ZnxCdyMg1-x-ySe epilayers on InP using ZnCl2," *Journal of Applied Physics,* vol. 84, pp. 1472-1475, Aug 1998.

[58] W. Faschinger, S. Ferreira, and H. Sitter, "DOPING OF ZINC-SELENIDE-TELLURIDE," *Applied Physics Letters,* vol. 64, pp. 2682-2684, May 1994.

[59] G. P. Schwartz, G. J. Gualtieri, J. E. Griffiths, C. D. Thurmond, and B. Schwartz, "OXIDE-SUBSTRATE AND OXIDE-OXIDE CHEMICAL-REACTIONS IN THERMALLY ANNEALED ANODIC FILMS ON GASB, GAAS, AND GAP," *Journal of the Electrochemical Society,* vol. 127, pp. 2488-2499, 1980.

[60] E. J. Koerperick, L. M. Murray, D. T. Norton, T. F. Boggess, and J. P. Prineas, "Optimization of MBE-grown GaSb buffer layers and surface effects of antimony stabilization flux," *Journal of Crystal Growth,* vol. 312, pp. 185-191, Jan 2010.

[61] C. E. C. Wood, K. Singer, T. Ohashi, L. R. Dawson, and A. J. Noreika, "A PRAGMATIC APPROACH TO ADATOM-INDUCED SURFACE RECONSTRUCTION OF III-V COMPOUNDS," *Journal of Applied Physics,* vol. 54, pp. 2732-2737, 1983.

[62] C. A. Wang, D. A. Shiau, and A. Lin, "Preparation of GaSb substrates for GaSb and GaInAsSb growth by organometallic vapor phase epitaxy," *Journal of Crystal Growth,* vol. 261, pp. 385-392, Jan 2004.

[63] Z. Y. Liu, B. Hawkins, and T. F. Kuech, "Chemical and structural characterization of GaSb(100) surfaces treated by HCI-based solutions and annealed in vacuum," *Journal of Vacuum Science & Technology B,* vol. 21, pp. 71-77, Jan-Feb 2003.

[64] F. W. O. Dasilva, C. Raisin, M. Silga, M. Nouaoura, and L. Lassabatere, "CHEMICAL PREPARATION OF GASB (001) SUBSTRATES PRIOR TO MBE," *Semiconductor Science and Technology,* vol. 4, pp. 565-569, Jul 1989.

[65] A. Jenichen and C. Engler, "Etching of GaAs(100) surfaces by Cl-2: Quantum chemical calculations on the mechanisms," *Journal of Physical Chemistry B,* vol. 104, pp. 8210-8216, Aug 31 2000.

[66] T. Ohno, "REACTIONS OF CL WITH GAAS - A THEORETICAL UNDERSTANDING OF GAAS-SURFACE ETCHING," *Physical Review B,* vol. 44, pp. 8387-8390, Oct 15 1991.

[67] M. L. Yu and L. A. Delouise, "SURFACE-CHEMISTRY ON SEMICONDUCTORS STUDIED BY MOLECULAR-BEAM REACTIVE SCATTERING," *Surface Science Reports,* vol. 19, pp. 289-380, 1994 1994.

[68] J. Wu, W. Shan, and W. Walukiewicz, "Band anticrossing in highly mismatched III-V semiconductor alloys," *Semiconductor Science and Technology,* vol. 17, pp. 860-869, Aug 2002.

[69] N. Lopez, L. A. Reichertz, K. M. Yu, K. Campman, and W. Walukiewicz, "Engineering the Electronic Band Structure for Multiband Solar Cells," *Physical Review Letters,* vol. 106, Jan 2011.

[70] W. Wang, A. S. Lin, and J. D. Phillips, "Intermediate-band photovoltaic solar cell based on ZnTe:O," *Applied Physics Letters,* vol. 95, Jul 6 2009.

[71] C. Tablero, A. Marti, and A. Luque, "Analyses of the intermediate energy levels in ZnTe:O alloys," *Applied Physics Letters,* vol. 96, Mar 2010.

[72] B. Lee and L. W. Wang, "Electronic structure of ZnTe:O and its usability for intermediate band solar cell," *Applied Physics Letters,* vol. 96, Feb 2010.

[73] W. M. Wang, A. S. Lin, and J. D. Phillips, "Intermediate-band photovoltaic solar cell based on ZnTe:O," *Applied Physics Letters,* vol. 95, 2009.

[74] M. Reason, H. A. McKay, W. Ye, S. Hanson, R. S. Goldman, and V. Rotberg, "Mechanisms of nitrogen incorporation in GaAsN alloys," *Applied Physics Letters,* vol. 85, pp. 1692-1694, Sep 2004.

[75] Y. Jin, R. M. Jock, H. Cheng, Y. He, A. M. Mintarov, Y. Wang*, et al.*, "Influence of N interstitials on the electronic properties of GaAsN alloys," *Applied Physics Letters,* vol. 95, Aug 10 2009.

[76] R. L. Field, Y. Jin, H. Cheng, T. Dannecker, R. M. Jock, Y. Q. Wang*, et al.*, "Influence of N incorporation on persistent photoconductivity in GaAsN alloys," *Physical Review B,* vol. 87, Apr 2013.

[77] C. Ling, L. Q. Zhou, D. Banerjee, and H. F. Jia, "Band structures of ZnTe:O alloys with isolated oxygen and with clustered oxygen impurities," *Journal of Alloys and Compounds,* vol. 584, pp. 289-294, Jan 2014.

[78] B. Lee and L.-W. Wang, "Electronic structure of ZnTe:O and its usability for intermediate band solar cell," *Applied Physics Letters,* vol. 96, Feb 15 2010.

[79] T. Tanaka, S. Kusaba, T. Mochinaga, K. Saito, Q. X. Guo, M. Nishio*, et al.*, "Molecular beam epitaxial growth and optical properties of highly mismatched ZnTe1-xOx alloys," *Applied Physics Letters,* vol. 100, Jan 2012.

[80] K. M. Yu, W. Walukiewicz, W. Shan, J. Wu, J. W. Beeman, M. A. Scarpulla*, et al.*, "Synthesis and optical properties of II-O-VI highly mismatched alloys," *Journal of Applied Physics,* vol. 95, pp. 6232-6238, Jun 1 2004.

[81] K. M. Yu, J. Wu, W. Walukiewicz, J. W. Beeman, J. W. Ager, E. E. Haller*, et al.*, "Band anticrossing in highly mismatched group II-VI semiconductor alloys," *Journal of Electronic Materials,* vol. 31, pp. 754-758, Jul 2002.

[82] J. L. Merz, "ISOELECTRONIC OXYGEN TRAP IN ZNTE," *Physical Review,* vol. 176, pp. 961-&, 1968 1968.

[83] M. J. Seong, I. Miotkowski, and A. K. Ramdas, "Oxygen isoelectronic impurities in ZnTe: Photoluminescence and absorption spectroscopy," *Physical Review B,* vol. 58, pp. 7734-7739, Sep 15 1998.

[84] D. G. Thomas, J. J. Hopfield, and C. J. Frosch, "ISOELECTRONIC TRAPS DUE TO NITROGEN IN GALLIUM PHOSPHIDE," *Physical Review Letters,* vol. 15, pp. 857-&, 1965.

[85] S. B. Zhang and S. H. Wei, "Nitrogen solubility and induced defect complexes in epitaxial GaAs : N," *Physical Review Letters,* vol. 86, pp. 1789-1792, Feb 2001.

[86] P. Krispin, V. Gambin, J. S. Harris, and K. H. Ploog, "Nitrogen-related electron traps in Ga(As,N) layers (<= 3% N)," *Journal of Applied Physics,* vol. 93, pp. 6095-6099, May 2003.

[87] M. J. Reason, "Structure and Properties of Dilute Nitride GaAsN Alloy Films," Doctor of Philosophy, Materials Science and Engineering, University of Michigan, Ann Arbor, 2006.

[88] Y. C. Lin, M. J. Tasi, W. C. Chou, W. H. Chang, W. K. Chen, T. Tanaka*, et al.*, "Recombination dynamics and carrier lifetimes in highly mismatched ZnTeO alloys," *Applied Physics Letters,* vol. 103, Dec 2013.

[89] Y. Zhang, B. J. Skromme, and F. S. Turcosandroff, "EFFECTS OF THERMAL STRAIN ON THE OPTICAL-PROPERTIES OF HETEROEPITAXIAL ZNTE," *Physical Review B,* vol. 46, pp. 3872-3885, Aug 15 1992.

[90] J. J. Hopfield, D. G. Thomas, and R. T. Lynch, "ISOELECTRONIC DONORS AND ACCEPTORS," *Physical Review Letters,* vol. 17, pp. 312-&, 1966 1966.

[91] G. Shigaura, M. Ohashi, Y. Ichinohe, M. Kanamori, N. Kimura, T. Sawada*, et al.*, "Deep emissions of MBE-ZnTe on tilted GaAs substrate," *Journal of Crystal Growth,* vol. 301, pp. 297-300, Apr 2007.

[92] Y. M. Yu, S. Nam, K. S. Lee, Y. D. Choi, and B. O, "Photoluminescence characteristics of ZnTe epilayers," *Journal of Applied Physics,* vol. 90, pp. 807-812, Jul 15 2001.

[93] H. Venghaus and P. J. Dean, "SHALLOW-ACCEPTOR, DONOR, FREE-EXCITON, AND BOUND-EXCITON STATES IN HIGH-PURITY ZINC TELLURIDE," *Physical Review B,* vol. 21, pp. 1596-1609, 1980 1980.

[94] K. V. Solov'ev, B. V. Lisovoi, and Y. A. Mironchenko, "On the nature of the luminescence centers in epitaxial films of zinc telluride," *Technical Physics Letters,* vol. 23, pp. 933-934, Dec 1997.

[95] S. Iida, "LUMINESCENCE DUE TO OXYGEN AND SELF-ACTIVATED CENTERS IN ZINC TELLURIDE," *Journal of the Physical Society of Japan,* vol. 32, pp. 142-&, 1972 1972.

[96] M. Felici, A. Polimeni, M. Capizzi, Y. Nabetani, T. Okuno, K. Aoki*, et al.*, "Passivation of an isoelectronic impurity by atomic hydrogen: The case of ZnTe : O," *Applied Physics Letters,* vol. 88, Mar 6 2006.

[97] M. Uchida, Y. Matsuda, T. Asahi, K. Sato, and O. Oda, "Stoichiometry control of ZnTe single crystals by the vapor pressure-controlled wafer-annealing method," *Journal of Crystal Growth,* vol. 216, pp. 134-140, Jul 2000.

[98] M. A. Berding, M. Vanschilfgaarde, A. T. Paxton, and A. Sher, "DEFECTS IN ZNTE, CDTE, AND HGTE - TOTAL ENERGY CALCULATIONS," *Journal of Vacuum Science & Technology a-Vacuum Surfaces and Films,* vol. 8, pp. 1103-1107, Mar-Apr 1990.

[99] J. D. Dow, R. D. Hong, S. Klemm, S. Y. Ren, M. H. Tsai, O. F. Sankey*, et al.*, "PROPOSED EXPLANATION OF THE P-TYPE DOPING PROCLIVITY OF ZNTE," *Physical Review B,* vol. 43, pp. 4396-4407, Feb 1991.

[100] C. B. Norris, "EFFECTS OF ZN-VAPOR HEAT-TREATMENTS ON THE EDGE EMISSION AND DEEP-CENTER LUMINESCENCE OF ZNTE," *Journal of Electronic Materials,* vol. 9, pp. 913-931, 1980.

[101] W. Wang, W. Bowen, S. Spanninga, S. Lin, and J. Phillips, "Optical Characteristics of ZnTeO Thin Films Synthesized by Pulsed Laser Deposition and Molecular Beam Epitaxy," *Journal of Electronic Materials,* vol. 38, pp. 119-125, Jan 2009.

[102] E. Antolin, C. Chen, I. Ramiro, J. Foley, E. Lopez, I. Artacho*, et al.*, "Intermediate Band to Conduction Band Optical Absorption in ZnTeO," *Ieee Journal of Photovoltaics,* vol. 4, pp. 1091-1094, Jul 2014.

[103] Z. T. Kang, C. J. Summers, H. Menkara, B. K. Wagner, R. Durst, Y. Diawara*, et al.*, "ZnTe : O phosphor development for x-ray imaging applications," *Applied Physics Letters,* vol. 88, Mar 2006.

[104] V. V. Nagarkar, V. Gaysinskiy, O. E. Ovechkina, S. Miller, B. Singh, L. Guo*, et al.*, "Bright Semiconductor Scintillator for High Resolution X-Ray Imaging," *Ieee Transactions on Nuclear Science,* vol. 57, pp. 923-930, Jun 2010.

[105] W. Wang, A. S. Lin, J. D. Phillips, and W. K. Metzger, "Generation and recombination rates at ZnTe:O intermediate band states," *Applied Physics Letters,* vol. 95, Dec 28 2009.

[106] E. Antolin, A. Marti, C. R. Stanley, C. D. Fanner, E. Canovas, N. Lopez*, et al.*, "Low temperature characterization of the photocurrent produced by two-photon transitions in a quantum dot intermediate band solar cell," *Thin Solid Films,* vol. 516, pp. 6919-6923, Aug 30 2008.

[107] Y. Okada, T. Morioka, K. Yoshida, R. Oshima, Y. Shoji, T. Inoue*, et al.*, "Increase in photocurrent by optical transitions via intermediate quantum states in direct-doped InAs/GaNAs strain-compensated quantum dot solar cell," *Journal of Applied Physics,* vol. 109, Jan 15 2011.

[108] A. Scaccabarozzi, S. Adorno, S. Bietti, M. Acciarri, and S. Sanguinetti, "Evidence of two-photon absorption in strain-free quantum dot GaAs/AlGaAs solar cells," *Physica Status Solidi-Rapid Research Letters,* vol. 7, pp. 173-176, Mar 2013.

[109] V. A. Stoica, C. Chen, R. Schaller, J. D. Phillips, and R. Clarke, "Two step sub-bandgap radiative carrier injection in ZnTeO," *To be published,* 2015.

[110] U. V. Desnica, "Doping limits in II-VI compounds - Challenges, problems and solutions," *Progress in Crystal Growth and Characterization of Materials,* vol. 36, pp. 291-357, 1998.

[111] D. J. Chadi, "DOPING IN ZNSE, ZNTE, MGSE, AND MGTE WIDE-BAND-GAP SEMICONDUCTORS," *Physical Review Letters,* vol. 72, pp. 534-537, Jan 1994.

[112] R. S. Title, F. F. Morehead, and G. Mandel, "SELF-COMPENSATION-LIMITED CONDUCTIVITY IN BINARY SEMICONDUCTORS .2. N-ZNTE," *Physical Review a-General Physics,* vol. 136, pp. A300-&, 1964.

[113] J. B. Li and S. H. Wei, "Alignment of isovalent impurity levels: Oxygen impurity in II-VI semiconductors," *Physical Review B,* vol. 73, Jan 2006.

[114] W. Walukiewicz, "Intrinsic limitations to the doping of wide-gap semiconductors," *Physica B,* vol. 302, pp. 123-134, Aug 2001.

[115] M. Brasil, R. E. Nahory, F. S. Turcosandroff, H. L. Gilchrist, and R. J. Martin, "EVOLUTION OF THE BAND-GAP AND THE DOMINANT RADIATIVE RECOMBINATION CENTER VERSUS THE COMPOSITION FOR ZNSE1-XTEX ALLOYS GROWN BY MOLECULAR-BEAM EPITAXY," *Applied Physics Letters,* vol. 58, pp. 2509-2511, Jun 1991.

[116] W. Lin, B. X. Yang, S. P. Guo, A. Elmoumni, F. Fernandez, and M. C. Tamargo, "Molecular-beam epitaxy growth and nitrogen doping of ZnSe1-xTex alloys grown on InP substrates," *Applied Physics Letters,* vol. 75, pp. 2608-2610, Oct 1999.

[117] M. Brasil, M. C. Tamargo, R. E. Nahory, H. L. Gilchrist, and R. J. Martin, "ZN1-YCDYSE1-XTEX QUATERNARY WIDE BAND-GAP ALLOYS - MOLECULAR-BEAM EPITAXIAL-GROWTH AND OPTICAL-PROPERTIES," *Applied Physics Letters,* vol. 59, pp. 1206-1208, Sep 1991.

[118] J. M. Hartmann, J. Cibert, F. Kany, H. Mariette, M. Charleux, P. Alleysson*, et al.*, "CdTe/MgTe heterostructures: Growth by atomic layer epitaxy and determination of MgTe parameters," *Journal of Applied Physics,* vol. 80, pp. 6257-6265, Dec 1 1996.

[119] A. Waag, H. Heinke, S. Scholl, C. R. Becker, and G. Landwehr, "GROWTH OF MGTE AND CD1-XMGXTE THIN-FILMS BY MOLECULAR-BEAM EPITAXY," *Journal of Crystal Growth,* vol. 131, pp. 607-611, Aug 1993.

[120] J. P. Faurie, C. Hsu, S. Sivananthan, and X. Chu, "CDTE-GAAS(100) INTERFACE - MBE GROWTH, RHEED AND XPS CHARACTERIZATION," *Surface Science,* vol. 168, pp. 473-482, Mar 1986.

[121] T. Baron, S. Tatarenko, K. Saminadayar, N. Magnea, and J. Fontenille, "PLASMA NITROGEN DOPING OF ZNTE, CD1-XZNXTE, AND CDTE BY MOLECULAR-BEAM EPITAXY," *Applied Physics Letters,* vol. 65, pp. 1284-1286, Sep 1994.